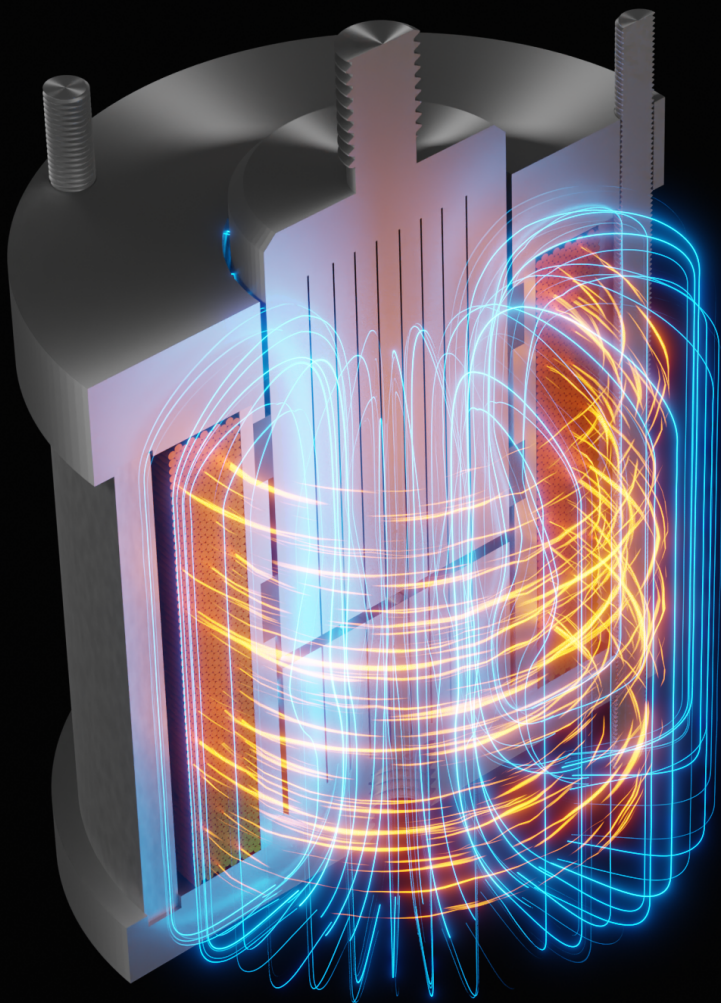


Bandwidth Optimisation of Solenoid Actuator



EMSD4
Daniel Woldbye Steffensen
Frederik Sanderhoff
Jens Erik Damgaard Mejdahl

02-06-2022



AALBORG UNIVERSITET

STUDENTERRAPPORT

**Det Ingeniør-
og Naturvidenskabelige Fakultet**
Electro-Mechanical System Design
Fibigerstræde 16
9220 Aalborg Øst
<http://www.aau.dk>

Title:

Bandwidth Optimisation
of Solenoid Actuator

Project:

EMSD 4. Semester
Master's Thesis

Project period:

1st of February to
2nd of June 2022

Project group members:

Daniel Woldbye Steffensen
Frederik Sanderhoff
Jens Erik Damgaard Mejdahl

Supervisor:

Per Johansen
Michael Møller Bech

Main report pages: 77

Appendix pages: 17

Date for hand in: 2nd of June 2022

Abstract:

The UltrAdapt project at Aalborg University aims to use non-invasive measurement techniques of fluid film thicknesses to estimate states inside journal bearings. In order to aid this work a test bench has previously been developed but it is of interest to improve upon this. The bandwidth of the solenoid actuators, included in this test bench, are of special interest. Thorough transient FE analyses of the actuator shows how eddy currents effectively suppresses the development of the magnetic field within the actuator. An optimisation algorithm is developed based on the FE model in order to place strategic cuts in the actuator material and thereby suppressing eddy currents during transient operation. A total of 17 cuts are made, eight in the plunger, eight in the center piece, and a single slit in the internal aluminium tubes which improves the actuator bandwidth from 5 Hz to 38 Hz. A control algorithm consisting of a feed forward, a proportional controller and an unconventional integral controller is proposed, designed and implemented in order to further increase the actuator bandwidth to 39 Hz as well as ensuring a DC tracking performance of ± 0.01 dB at a full scale input. A Kalman filter is also developed and tested on experimental data with the primary focus of increasing system robustness, though it is not implemented on the real time target controlling the actuator. Final results indicates that only minor further improvements of the bandwidth can be made on the system since limitations in the input voltage is the primary impediment towards a higher bandwidth.

By signing this document, each member of the group confirms participation on equal terms in the process of writing the project. Thus, each member of the group is responsible for all contents in the project.

Preface

This report is written as a master thesis group project on the Master in Electro-Mechanical System Design at Aalborg University under supervision of Associate Professor Per Johansen and Associate Professor Michael Møller Bech. The authors are Daniel Woldbye Steffensen, Frederik Sanderhoff and Jens Erik Damgaard Mejdahl, who have developed the report in the project period from 1st of February to 2nd of June 2022. The authors would like to thank Associate Professor Per Johansen and Michael Møller Bech for their insight, supervision and help. Additionally the authors would like to thank PhD fellow Elias Vagn Hansen for his inputs and support.

The target recipients of the report are the supervisors at Aalborg University, external examiner and interested researchers or engineers in general.

Reading manual

The source citations is based on the Harvard referencing method. With the source citations written in parenthesis right after the quote, e.g. (Surname year) or as a part of the text, e.g. Surname (year). The sources are presented in the bibliography after the main report. All units used in the report are denoted in SI-units or derived thereof. Throughout the report, names like "solenoid", "actuator" and "solenoid actuator" all refers to the specific solenoid actuator of interest in this project. The expression "DC" is in this report synonymous to steady state.

References to appendix, equations, figures and quotes follows the approach in the following example: 'shown in Figure 2.1', referring to the first figure in chapter 2. When the figure is positioned on another page or section, the reference is instead written as 'shown in Figure 2.1 on page xx'. Appendix E and F is of such significant size that the files are attached in the external zip-folder.

Daniel Woldbye Steffensen

Frederik Sanderhoff

Jens Erik Damgaard Mejdahl

Summary

In this report a thorough evaluation of an existing solenoid actuator is carried out. This actuator is part of a bigger system, which serves as a test bench for hydrodynamic bearings. Multiple of these solenoid actuators are used in parallel to exert different loading scenarios onto a single bearing specimen. This bearing test system was designed, developed and manufactured in a former project done by the same authors (Steffensen, Sanderhoff, and Mejdahl 2021). The solenoid actuators are designed to exert a high force, while a requirement was also specified for the bandwidth of the actuators. This bandwidth requirement is not achieved in the previous work, which forms the motivation for this project. In this report improvements to the system are suggested, implemented and tested such that the force exertion system is able to comply with the specified requirement.

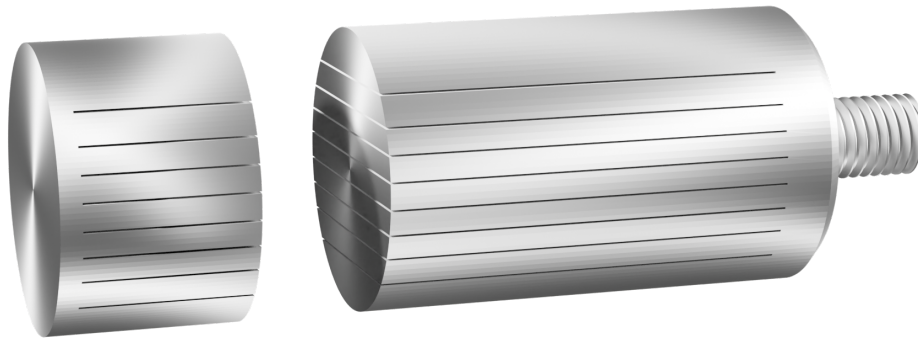


Figure 1. Example of components with multiple thin cuts.

A fundamental focus point of this report is related to the induction of eddy currents, which occurs during the build up of the magnetic field in the solenoid actuators. These eddy currents are shown to decrease the speed of the actuators and are effectively suppressing the dynamic performance of the system. While these eddy currents are unavoidable in systems consisting of components with a high electrical conductivity, it is shown in this project how to decrease the intensity of the eddy currents. Specifically this project is concerned with breaking the pathways of the induced eddy currents by making deliberate cuts in key components of the solenoid. An example of two components which have been cut is seen in Figure 1. With the use of finite element analysis as well as optimisation techniques it is shown how to effectively place these cuts. These simple actions are shown theoretically and experimentally to give quite profound improvements to the speed of the system.

Another key aspect of the improvement of the solenoid actuators are techniques used to effectively control these. In this report a complete control strategy for the solenoid actuators are proposed. As the actuators are to be inserted into a complete system, the control of these are essential. To achieve a high performing system, different measures are taken. An alternative PI controller is proposed, which is implemented alongside an extended Kalman filter which acts like a multipurpose tool for different parts of the control system. This Kalman filter is based on a sophisticated and extensive model of the solenoid actuator, that includes a material model which have been experimentally derived and validated. Together, the idea of making cuts in various components of the systems, as well as implementing the control strategy is shown both theoretically and experimentally to significantly improve the performance of the system.

Nomenclature

Symbol/Abbreviation	Meaning
AAU	Aalborg University
CPM	Classical Preisach model
EDM	Electrical discharge machining
FE	Finite element
FF	Feed forward
FEM	Finite element method
GPM	Generalised Preisach model
I	Integral controller
IW	Integral controller with anti-Windup
MEIW	Model Error Integral controller with anti-Windup
MMF	Magnetomotive force
NaN	Not a number
P	Proportional controller
PI	Proportional-integral
POM	Polyoxymethylene
RBS	Random binary signal
RMSE	Root Mean Square Error
SPA	Spectral analysis

Table of Contents

Chapter 1 Introduction & problem analysis	1
1.1 Existing system and potential changes	6
Chapter 2 Problem formulation	8
2.1 Requirements and delimitation	8
Chapter 3 Preliminary work	10
3.1 Calculation of system bandwidth	10
3.2 Feed forward for open loop bandwidth determination	12
3.3 Actuator test stand	13
3.4 ESCON 50/5 current controller	13
3.5 System identification	14
Chapter 4 Modelling of solenoid	16
4.1 Nonlinear solenoid model	16
4.2 Model parameters	19
4.3 Model validation	24
4.4 Subsidiary conclusion	26
Chapter 5 Transient analysis of solenoid geometry	27
5.1 Electromagnetic finite element analysis	27
5.2 Analysis of solenoid system	28
5.3 Redesigning the aluminium center tubes	32
5.4 Test of improved solenoid prototype	36
5.5 Subsidiary conclusion	37
Chapter 6 Optimisation of cut pattern design	38
6.1 General optimisation approach	38
6.2 Modelling the solenoid	40
6.3 Design variables and design space	47
6.4 Cost function for optimisation problem	48
6.5 Constraints	50
6.6 Optimisation algorithm and solver	51
6.7 Results	52
6.8 Manufacturing and test of cut design	55
6.9 Subsidiary conclusion	57
Chapter 7 Control	58
7.1 Dynamic feed forward from non-linear solenoid model	59
7.2 Feedback controllers	61
7.3 Kalman filter	65
7.4 Control results	71
7.5 Subsidiary conclusion	73
Chapter 8 Conclusion	74
Chapter 9 Discussion & further Work	75

Bibliography	77
I Appendix	78
Appendix A Structural analysis of test stand	79
Appendix B Magnetic material properties of S235	83
Appendix C Mathematical basis of Preisach model	89
Appendix D Electrical conductivity of S235	91
Appendix E Previous report by the same authors	94
Appendix F Technical drawings of test stand	95

Introduction & problem analysis

1

The UltrAdapt project at Aalborg University aims to use non-invasive measurement techniques, such as ultrasonic measurements of fluid film thicknesses, to estimate different states inside journal bearings. This can be done by the use of tribological state observers, so in order to develop and verify these a test bench is previously made. It is however desirable to improve upon the solenoid actuators within this test bench which is the primary focus of the present report. The following chapter serves as a summary of the main findings and work of the former project (Steffensen, Sanderhoff, and Mejdahl 2021) that developed the test bench. This is done to establish a common foundation for proceeding the work, meaning that details of the existing products and knowledge is presented. This project will specifically focus on improving a solenoid actuator which were designed, developed and manufactured during the former project. The solenoid actuator and the main parts of the former project is summarised below.

The objective of the former project was to design and manufacture a test bench for journal bearings. More specifically the work serves as an aid to the UltrAdapt research group situated at AAU. This group is concerned with adaptive lubrication measurement technology based on ultrasonic transducers (Per Johansen 2020). Here journal bearings are of interest as these are widely used in industrial applications. Due to the complex nature of such a tribological system and the related dynamics, the aim of the UltrAdapt project is among other things to develop measurement techniques and technologies to analyse such systems. To understand some of the design choices made for the solenoid actuators, which is a part of this test bench, the journal bearing and its characteristics are briefly introduced.

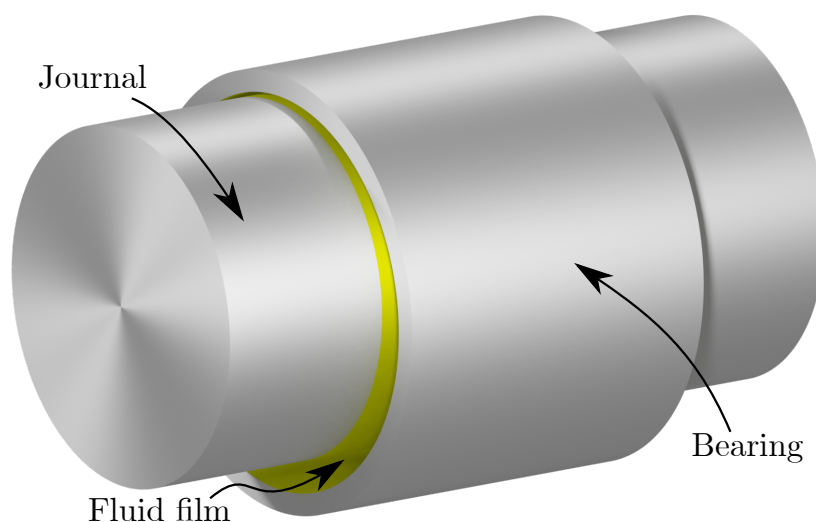


Figure 1.1. Component naming in journal bearings (Steffensen, Sanderhoff, and Mejdahl 2021).

The journal bearing consists of three main components; a rotating shaft called the journal, a lubricating layer of oil, and an outer bushing, containing the shaft and oil, called the bearing. An illustration of a simple journal bearing is shown in Figure 1.1. Note that the fluid film height is greatly exaggerated in the figure. The bearings purpose is to support a rotating load in the fluid film in order to reduce friction and wear. The journal bearings typically operate within the hydrodynamic regime of lubrication, which

describes the situation where the surfaces of the journal and bearing are fully separated by a thin fluid film (Steffensen, Sanderhoff, and Mejdahl 2021). This characteristic of a thin fluid film is important for the operation of the solenoid actuators. During operation of the journal bearing, the journal will move inside the bearing. An illustration of this is shown in Figure 1.2.

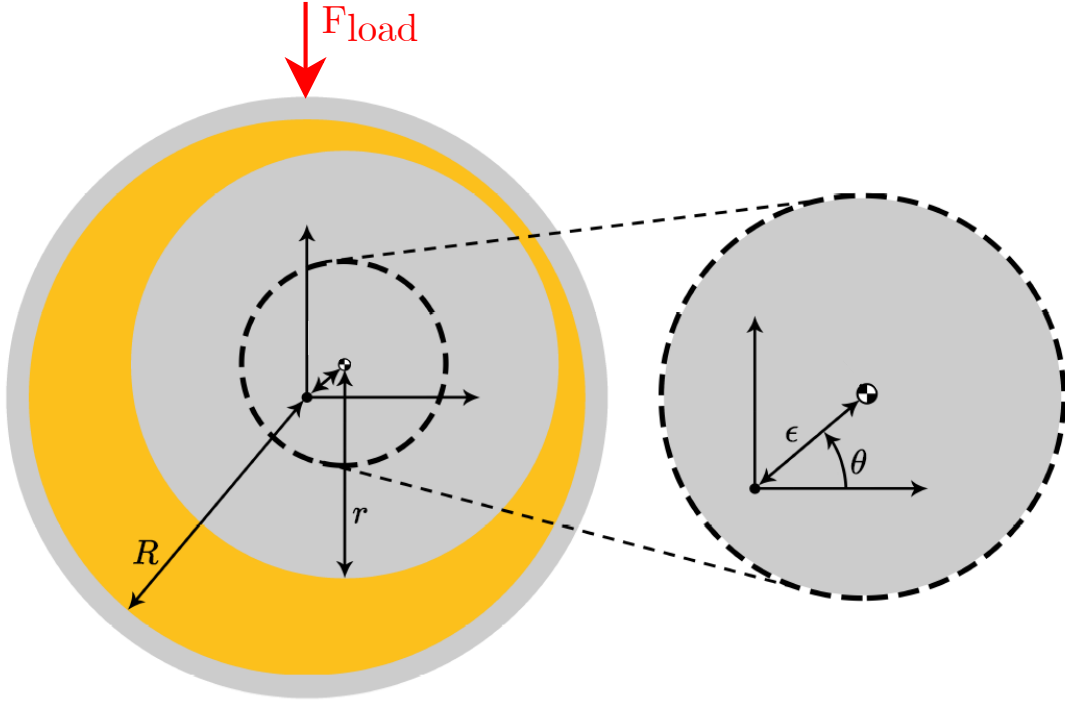


Figure 1.2. Journal bearing model (Steffensen, Sanderhoff, and Mejdahl 2021) (edited).

The height of the fluid film (the yellow part of the figure) is greatly exaggerated relative to the size of the journal and bearing, and will in reality be in the order of micrometers. In Figure 1.2, R denotes the inner radius of the bearing and r is the radius of the journal. From these a radial clearance is defined, $C_r = R - r$. The fluid film height is different around the circumferential direction, and is dependent on the position of the journal relative to the bearing. However, the maximum fluid film height, h_{max} , can be no more than: $h_{max} = 2C_r$. As a reference, the radial clearance in the initial journal bearing used in the developed test bench is around $50 \mu\text{m}$, which means that $h_{max} = 100 \mu\text{m}$.

In Figure 1.2 three additional variables are defined. These are the eccentricity, ϵ , which is defining the distance between the center of the journal and the center of the bearing, and θ which is the eccentricity angle. The load, F_{load} , is the resulting force applied by the solenoid actuators. These three quantities constitutes the origin of the work done in the former project. A model is developed, which described the dynamics from the load of the actuators to the journal eccentricity and eccentricity angle. These dynamics are dependent on the mechanical part of the system governed by the physics of motion, as well as the dynamics of the oil governed by the the physics of fluids. Generally, the dynamics are dependent on many parameters. An in depth explanation of these parameters can be found in the previous work (ibid.).

These journal bearing dynamics are coupled to the tribological properties and characteristics of the system, which is why they are of interest for the UltrAdapt project. Since it is the dynamics of the system that are of interest, an external system which can excite these dynamics is therefore needed to fully analyse the system. The external system must be able to exert a force with a varying size and direction to the journal bearing. In the former work such a solution is developed and is shown in Figure 1.3.

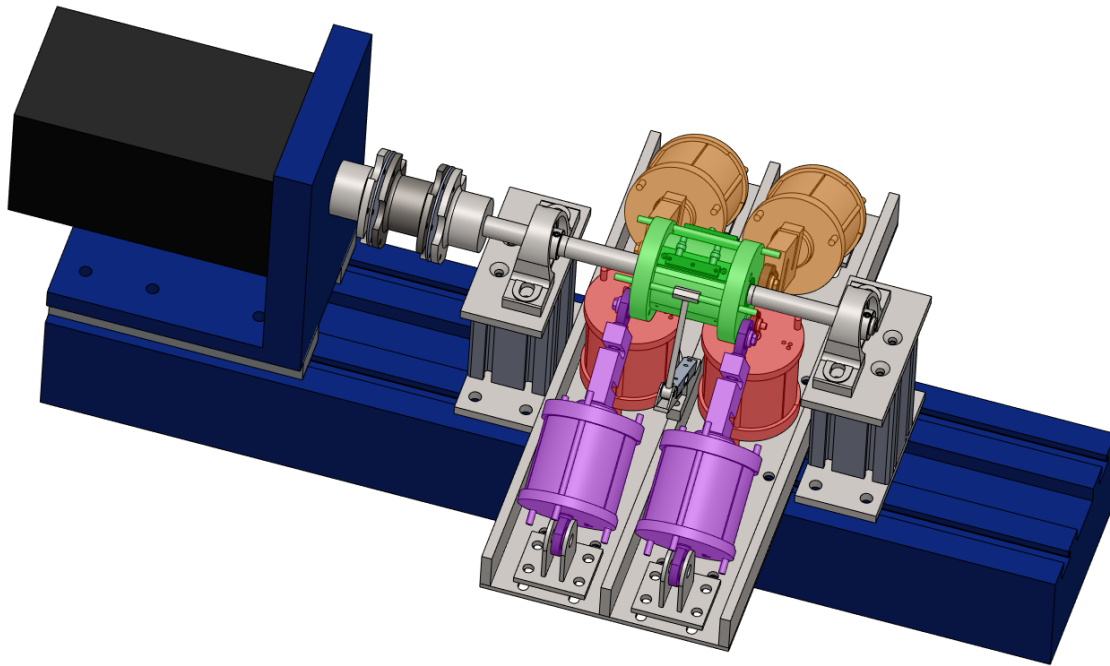


Figure 1.3. 3D model of test bench design (Steffensen, Sanderhoff, and Mejdahl 2021) (edited).

The green highlighted part of the solution is the component in which the bearing is mounted. The components marked with purple, red and orange are six solenoid actuators installed in the system. The purpose of these actuators are to exert a force on the component in which the bearing is mounted. The component transfers the force into the bearing which then transfers the force to the axle through the oil. This gives the possibility to simulate a loading scenario for a general journal bearing system. The purple and orange pair of solenoid actuators are designed such that they exert a pulling force, and the red pair is designed to exert a pushing force. These forces are illustrated in Figure 1.4. In Figure 1.5 a simple sketch of the solution is provided for overview.

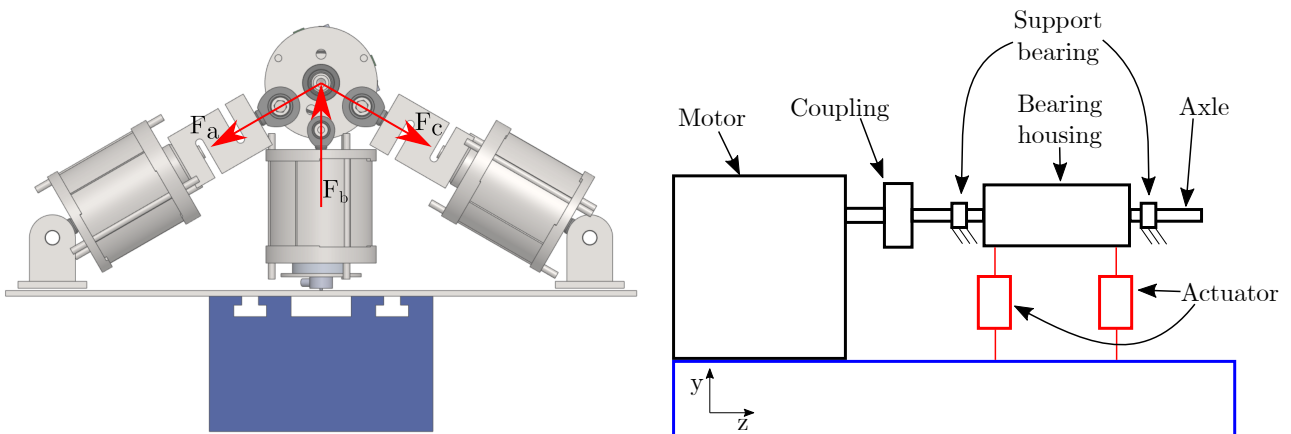


Figure 1.4. Solenoid forces on bearing component (Steffensen, Sanderhoff, and Mejdahl 2021).

Figure 1.5. Simple sketch of the solution (Steffensen, Sanderhoff, and Mejdahl 2021).

The two types of solenoid actuators included in the test bench were designed to have similar characteristics in terms of force and dynamics. In Figure 1.6 and 1.7 the pull and push solenoid designs are shown, respectively. Despite the air gap being variable, both solenoid types is designed to achieve a force of at least 600 N at an air gap length of 2 mm and a coil current of 5 A.

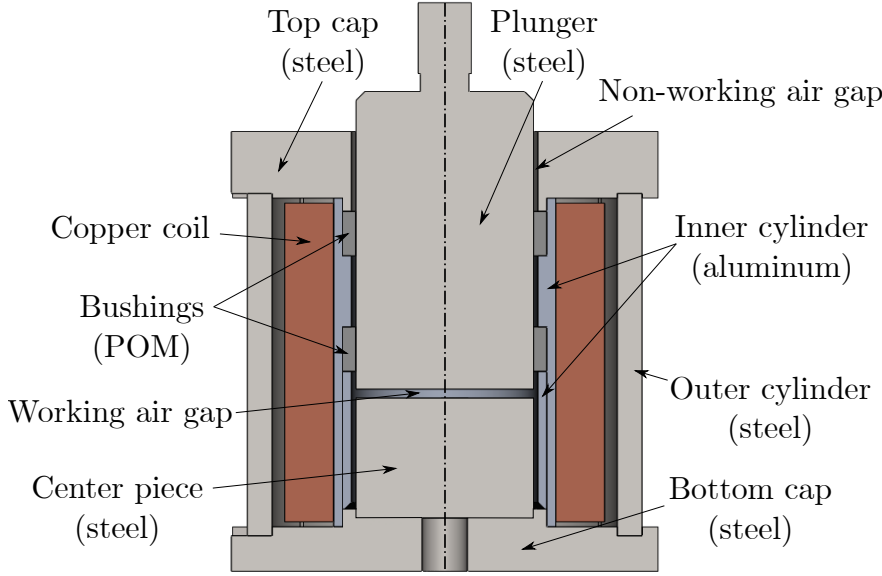


Figure 1.6. Solenoid actuator with pull configuration (Steffensen, Sanderhoff, and Mejdahl 2021) (edited).

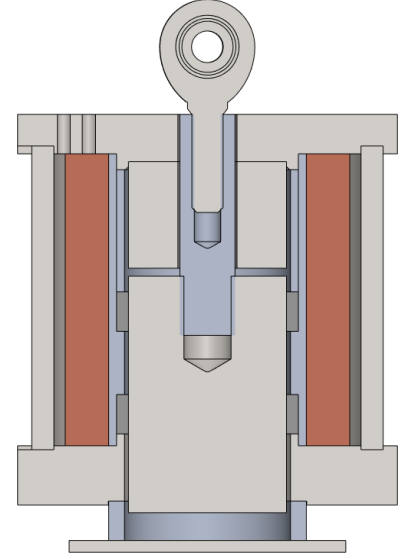


Figure 1.7. Push configuration (Steffensen, Sanderhoff, and Mejdahl 2021).

A special feature of the application of these solenoids is the fact that they are incorporated in a system in which little to no movement of the plunger is expected. In practice the only movement will be due to elastic deformation of the solid materials, as well as the relative movement between journal and bearing. For the setup including the initial journal bearing, a total displacement of $100\ \mu\text{m}$ is possible if elastic deformation is disregarded. A displacement of the plunger leads to a change in the exerted force by the actuator, since the force is dependent on the air gap length. In Steffensen, Sanderhoff, and Mejdahl (2021) an equation for the force, F , is found:

$$F = \frac{\partial W_{mag}}{\partial g} = -\frac{1}{2} \frac{N^2 i^2}{\mathcal{R}_{eq}(g)^2} \frac{d}{dg} (\mathcal{R}_{eq}(g)) = -\frac{1}{2} \frac{N^2}{\mu_0 \mu_{air} \pi r_{pl}^2} \frac{i^2}{\mathcal{R}_{eq}(g)^2} = -K_c \frac{i^2}{\mathcal{R}_{eq}(g)^2} = \frac{B_{ag}^2 A_{pl}}{2\mu_0 \mu_{air}} \quad (1.1)$$

Where W_{mag} is the magnetic energy in the solenoid, g is the air gap length, N is the number of windings in the coil, i is the current in the coil, \mathcal{R}_{eq} is the reluctance of the solenoid, which is dependent on the working air gap length (see Figure 1.6). The variable μ_0 is the vacuum permeability, μ_{air} is the relative permeability of air, r_{pl} is the radius of the plunger and K_c is a constant containing non-varying terms. The variable B_{ag} is the flux density in the air gap and A_{pl} is the area of the plunger.

In order to examine the force sensitivity in relation to the length of the working air gap, g , the partial derivative of the force with respect to the working air gap length is found. According to Steffensen, Sanderhoff, and Mejdahl (ibid.), the reluctance in the two air gaps accounts for more than 95% of the system reluctance, when the steel is not saturated. Therefore the equivalent reluctance in Equation 1.1, is simplified to only consist of the reluctance of the two air gaps:

$$\mathcal{R}_{eq} \approx \frac{g}{\mu_0 \mu_{air} r_{pl}^2 \pi} + \frac{l_{nwg}}{2\mu_0 \mu_{air} \left(r_{pl} + \frac{l_{nwg}}{2} \right) h_{nwg} \pi} \quad (1.2)$$

Here μ_0 is the vacuum permeability, μ_{air} is the relative permeability of air, l_{nwg} is the horizontal distance between the plunger and the top cap and h_{nwg} is the vertical height of the non-working air gap.

When Equation 1.2 is inserted into Equation 1.1 and it is partially differentiated with respect to the air gap length, the following is found:

$$\frac{\partial F}{\partial g} = - \frac{N^2 i^2}{\left(\frac{g}{\mu_0 \mu_{air} r_{pl}^2 \pi} + \frac{l_{nwag}}{2 \mu_0 \mu_{air} \left(r_{pl} + \frac{l_{nwag}}{2} \right) h_{nwag} \pi} \right)^3 \left(\mu_0 \mu_{air} r_{pl}^2 \pi \right)} \quad (1.3)$$

All parameter values are found in Steffensen, Sanderhoff, and Mejdahl (2021). When Equation 1.3 is evaluated at $i = 5$ A, the sensitivity can be plotted as a function of the length of the working air gap, as seen in Figure 1.8.

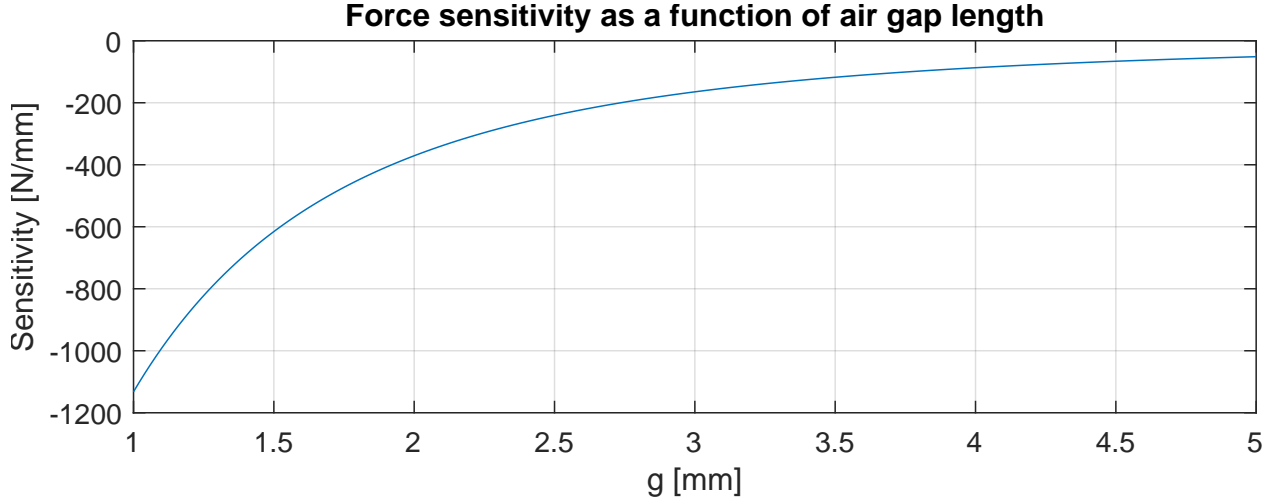


Figure 1.8. The force sensitivity evaluated as a function of the length of the working air gap.

It is seen from both Equation 1.3 and Figure 1.8, that the force sensitivity significantly increases when the air gap length decreases. The plot shows that the force sensitivity at an air gap length of 2 mm is approximately 370 N mm^{-1} .

For both solenoids a requirement is specified for the bandwidth of the systems. Here a minimum of 25 Hz is required, while it is desired to achieve a bandwidth of 50 Hz. This requirement was not met as the bandwidth was experimentally found to be around 5 – 6 Hz. This is the main motivation of this project, as it is focused upon increasing the bandwidth of the previously designed solenoid actuators. The reason why the requirements for the bandwidth in the former project was set to 25 – 50 Hz is due to the dynamics of the journal bearing system. In the former work a linear system is derived from the equation of motion and the fluid mechanics. While the model is quite comprehensive due to the complex nature of the fluid mechanics, the results are briefly reviewed here. This is to give a reasoning behind the desire to further increase the system bandwidth.

A linear model was setup for the system describing the dynamics from the load system to the journal eccentricity as shown in Equation 1.4. The full extent of the model derivation is found in Steffensen, Sanderhoff, and Mejdahl (ibid.).

$$\epsilon = G_{lin.model}(s) \cdot F_{load} \quad (1.4)$$

With a linear model, a parameter sensitivity analysis could easily be conducted. The parameters included are among others, geometric factors as length and diameter of the bearing and journal velocity. To be able to set the requirements in the former project, the bandwidth of a high amount of designs with randomised parameter values is calculated. The randomised parameter values are all within specified ranges, which is based on the requirements in the former project. As defined in Steffensen, Sanderhoff, and Mejdahl (ibid.), the force system is capable of sufficiently exciting a journal bearing, if the force

system bandwidth is equal to or higher than the journal bearing bandwidth. The result of this analysis is shown in Figure 1.9.

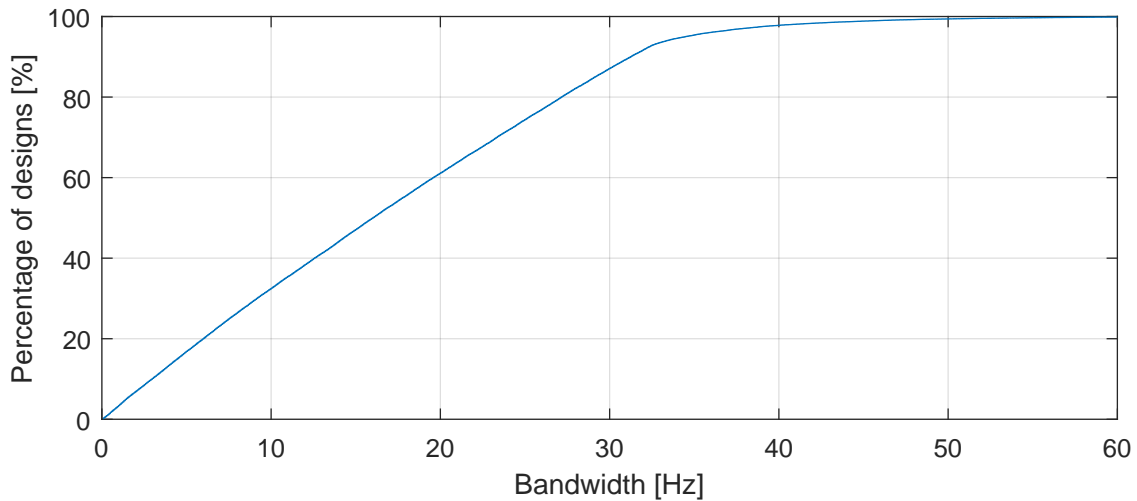


Figure 1.9. Percentage of designs reachable as a function of actuator bandwidth. (Steffensen, Sanderhoff, and Mejdahl 2021). A bearing design refers to a journal bearing with a set of specified parameters.

Figure 1.9 depicts the percentage of the random designs (the vertical axis) which can be sufficiently excited with a given bandwidth of the force system (the horizontal axis). These results were the foundation for the bandwidth requirements of the force system. With a bandwidth of 25 Hz, 75 % of the designs can be excited, and with 50 Hz, 99 % can be excited. As mentioned the designed solenoids achieved a bandwidth of approximately 5 – 6 Hz, which corresponds to a possible excitation of around 10 % of the designs. As this is unsatisfactory, this project is focused upon increasing the bandwidth of the solenoids, such that the bandwidth of a higher percentage of the journal bearing designs can be reached.

1.1 Existing system and potential changes

The solenoids are driven by a set of Maxon ESCON 50/5 motor controllers. The motor controllers consists of an H-bridge and a predefined PI control structure for the current, which can be tuned. Using the ESCON modules means that the electrical system is simple, adjustable and reliable. It is of this reason also desired to make continued use of these motor controllers, due to their ease of use. The motor controllers are rated to 50 V input voltage, a continuous current of 5 A and a peak current of 15 A.

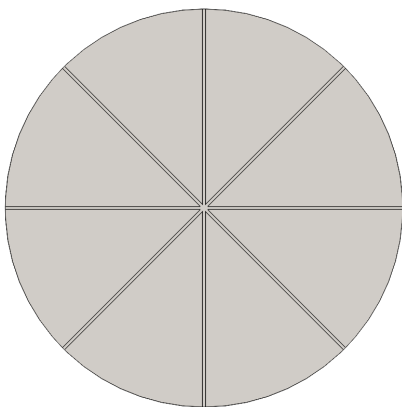


Figure 1.10. Cut pattern.

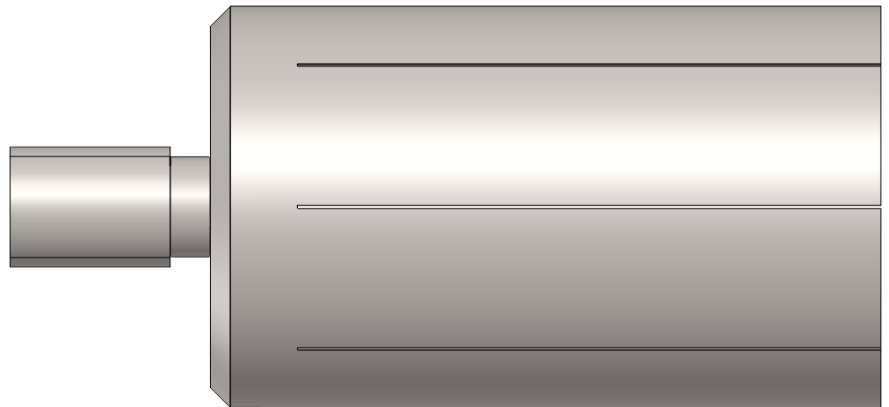


Figure 1.11. Side view of the sliced plunger.

In regards to the magnetic system dynamics, these are found to be heavily dependent on the eddy currents in the system. During transient operation, where the magnetic field is changing, eddy currents are induced. These eddy currents are opposing the changes in the magnetic field, which effectively slows the system. In Equation 1.1, it is seen that the force is dependent on the magnetic field in the working air gap, which means that the dynamics of the force is slowed by the eddy currents. In Steffensen, Sanderhoff, and Mejdahl (2021) a change in the plunger geometry is proposed to break the pathway of the eddy currents in order to reduce the intensity hereof. For the solenoid, the reduction of the eddy currents leads to an increase in the bandwidth of the system.

The proposed plunger geometry is shown in Figure 1.10 and 1.11. A plunger with these cuts is manufactured and inserted into the solenoid. In Figure 1.12 a response of the system is shown, where the current was stepped from 0 to 5 A.

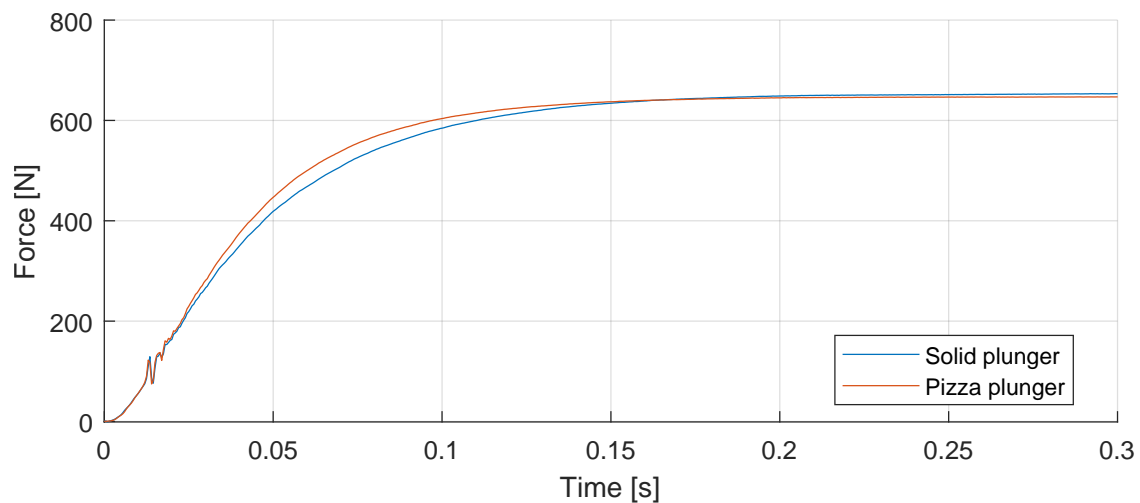


Figure 1.12. Step response of original and improved system.

In the response it is seen that by introducing the "pizza" cut pattern to the plunger, it is possible to slightly increase the speed of the system. The improved design showed that it is possible to alter the system bandwidth by changing the geometry of the plunger. This forms the foundation for the following project, which builds upon this solenoid actuator and the prior obtained knowledge.

Problem formulation 2

In this project the work of Steffensen, Sanderhoff, and Mejdahl (2021) will be continued. The project will focus upon improving the designed solenoid, such that it comply with the requirements specified in Steffensen, Sanderhoff, and Mejdahl (ibid.). The solenoids are to be a part of a force system which is required to exert a varying force on a variety of journal bearing test specimens. In order to sufficiently excite the dynamics of a wider range of these journal bearings, the bandwidth of the solenoids must be increased. To achieve this the project will carry on the investigation into making cuts in various parts as well as examine the use of control strategies.

In this project the following problem statement will be treated:

"How can the bandwidth of the existing solenoid actuator be increased by optimising the design and how can control algorithms support this while ensuring sufficient tracking performance of the force?"

To study the problem statement a number of selected research questions will be treated. These encompasses the subject and establishes the foundation for the report.

- What is governing the transient characteristics of the solenoid? How can these be analysed and modelled?
- How can the dynamics of the solenoid be improved without drastic design changes?
- How can a control system be developed, deployed and tested for the solenoid actuator?

2.1 Requirements and delimitation

In order to successfully treat the problem statement and work with the above described research questions, a number of objectives, requirements and limitation for the project is presented.

Goals and requirements

In order to set the focus of the project, the objectives and requirements of this project are defined. The goals of the project is:

- The main goal is to improve the bandwidth of the solenoid as much as possible.
- No major changes in any of the components are desired. This ensures that the existing manufactured parts can be reused as much as possible.

The set of requirements which the solenoid and these improvements are to comply with is presented below.

1. The outer dimensions of the solenoid such as length, diameter etc. is not be changed. This is such that the improved solenoid can directly replace the original design in the test bench, without the need to make changes to the remaining test bench components.

2. In the previous work a lower limit of the force of 600 N was specified. This limit and requirement is maintained in this work. This means that the solenoid must be able to exert a force of at least 600 N at a coil current of 5 A and air gap length of 2 mm.
3. In order for the force system to have an acceptable performance, it must have a bandwidth of at least 25 Hz and preferably 50 Hz. As the bandwidth of the system is of central concern, a clear definition of how it is calculated in this project, is presented in section 3.1.
4. In order to achieve sufficient tracking of a force reference, the system must be able to track a DC input with less than ± 0.1 dB steady state error.
5. Any proposed changes must be realisable, such that prototypes can be manufactured. This includes for example changes in material, as well as any proposed changes to the geometry of the solenoid. This is so, as there is a desire to deliver a working and proven solution to the UltrAdapt research group.

Delimitation of the project

In order to stay within the scope of the project, delimitations are necessary. Even though the solenoid is part of a bigger system, being the test bench, this system will not be of focus in this project. Generally the delimitation of the project is the following.

- Any changes to the electrical hardware is out of the scope of this project. While the electrical hardware definitely affects the dynamic performance of this system, this is simply not of focus. The performance of the existing electrical hardware is however treated in the project.
- Any changes in the design, geometry or material will be limited to only the pull solenoid. Here it is assumed that any knowledge gained on the pull solenoid systems will be directly applicable to the push systems.
- While plunger movement will be present in the real system, the dynamics hereof are not of immediate interest. The motion of the plunger is related to the fluid dynamics in the oil, which are not trivial to describe. Including an analysis of the motion dynamics is deemed to be complex compared to gain in overall model precision.

Generally the limitations of the project serve to keep the focus on the solenoid, which might cause some improvements to be disregarded. Any of such will be treated in the discussion and further work section of this report.

Preliminary work 3

The following chapter describes the preliminary work performed before the work on solving the problem statement is treated. This chapter will therefore be a mixture of underlying topics, which are to be addressed before the actual work on improving the solenoid is started.

3.1 Calculation of system bandwidth

The system bandwidth is the main point of interest for this project. As this will be treated repeatedly throughout this report, a review of how the bandwidth is calculated in this project is needed. A simple way of calculating the bandwidth is through linear models, but this is not preferable, due to the non-linearity of the system. The bandwidth, calculated based on linear models, is only valid in the linearisation point. The force system is meant to be a general purpose system, which can be operated within a specified range and not only in a linearisation point. For the non-linear system the bandwidth is calculated from experimental data, where the system is given a sine wave with increasing frequency as input, and the output is measured. As the bandwidth is to be a measure for the full capabilities of the system, the input oscillates between 50 N and 600 N. An illustration of the input and output is shown in Figure 3.1 and 3.2.

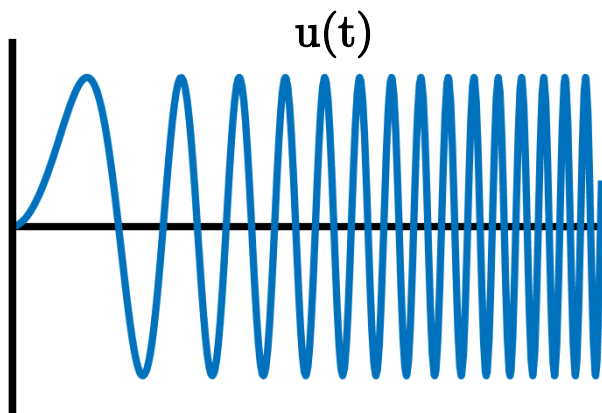


Figure 3.1. Sine input of increasing frequency.

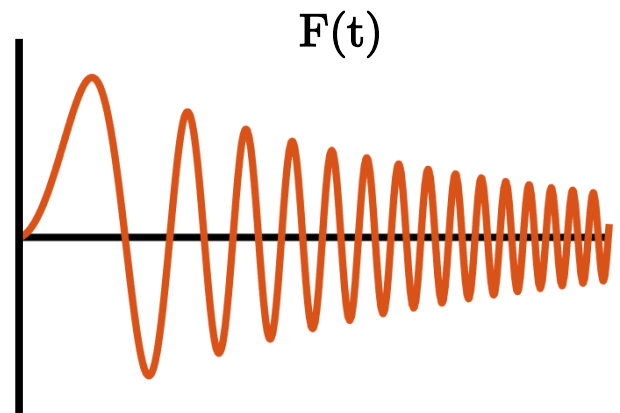


Figure 3.2. Force response of input.

The frequency response of the system is then calculated by comparing the input amplitude to the amplitude of the measured output of the system at each frequency. From this response the bandwidth is calculated as the frequency where the relationship between the input signal and the output drop below -3 dB compared to the DC value. This is illustrated in Figure 3.3.

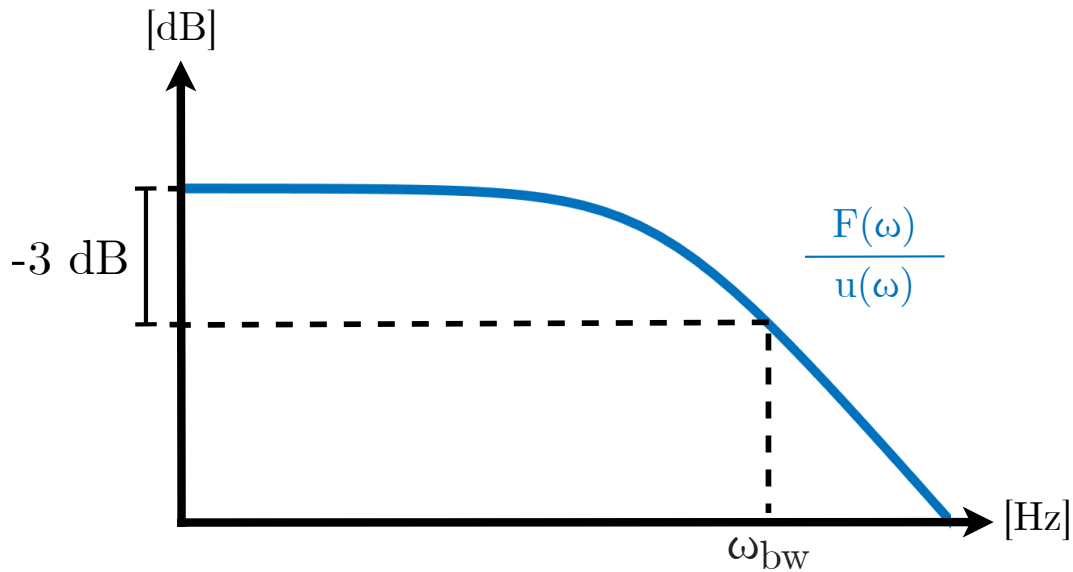


Figure 3.3. Example of frequency response and bandwidth definition.

With this bandwidth calculation any changes or additions to the solenoid system can be compared. Additionally the effects of non-linearity and limits in the controller effort can be included, as the bandwidth will be determined based on experiments of the system.

3.1.1 Bandwidth of open and closed loop systems

The purpose of the force system is to follow a reference signal. For a close loop system with feedback of the force, the input would simply be a force reference which this system is to track. In open loop, the control system is not tracking a reference, as there is no feedback. However, to be able to compare open and closed loop performance, any open loop system test will be pre-compensated with a feed forward, described in the following section (3.2), such that the signal in theory would follow the force reference. The system structure used when determining the bandwidth of the open loop systems can be seen in Figure 3.4.

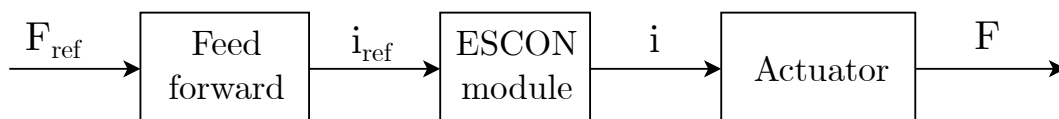


Figure 3.4. System structure when testing open loop systems.

The feed forward used for bandwidth determination is based on a lookup table. The details of this feed forward are described below.

3.2 Feed forward for open loop bandwidth determination

Feed forward can be used to predict the majority of the required input to the system. The idea behind feed forward is to use steady state knowledge of the system to predict the system input required in order to reach a given steady state output. The feed forward used for open loop bandwidth determination is based on a lookup table. This lookup table is meant to reflect the steady state current to force relationship of the actuator. The advantage of a lookup table is that it can represent complicated systems without computationally heavy calculations or the need for sophisticated models.

The lookup table used in this project is based on tests performed on the system. A test to determine the current to force relationship is therefore carried out every time a change has occurred in the actuator setup, in order to ensure that the lookup table reflects the actual system setup. In this test, the input current consists of a low frequency triangular wave varying from -1 A to 6 A . The input exceeds the normal operation range, to ensure that the lookup table covers the entire force range. Figure 3.5 shows the in- and outputs of the system as a function of time. This data is converted to plot the force for a given current, seen in Figure 3.6 as the blue lines. As the force is found to be dependent on the direction of the current, the data is averaged to get a single value for the force at a given current, and is shown as the orange line in Figure 3.6. This calculated mean force is used for the lookup table. The data is down-sampled to 100 points, to reduce memory usage. When implemented on the real time target, the data is linearly interpolated to regain resolution.

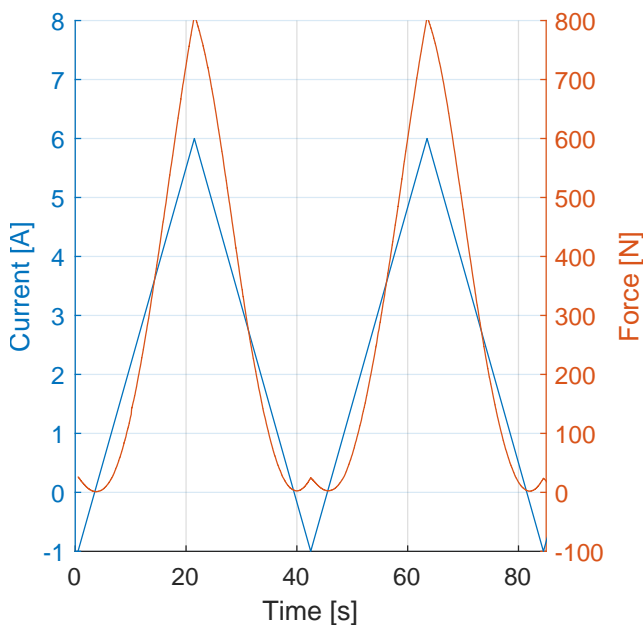


Figure 3.5. Test data from current sweep for lookup table feed forward.

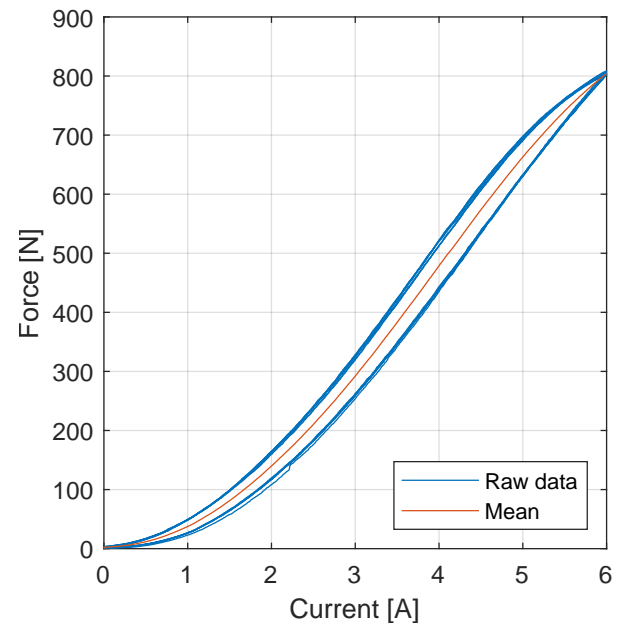


Figure 3.6. Force as a function of current, limited to positive current range

From Figure 3.6 it can also be seen that the current to force function is roughly linear from 200 N and up.

3.3 Actuator test stand

In order to conduct experiments on the actuator, an actuator test stand is developed. With a separate test stand the dynamic performance of the actuator is isolated from the rest of the system, meaning the influence of the oil dynamics and other parts of the test bench will not influence the solenoid actuator. This test stand is designed to be rigid, and allow for easy change of the actuator. The base of the test stand is designed to allow for tilting of the test stand, in order to mimic different mounting scenarios. The test stand can be seen in Figure 3.7.

The test stand is made of two triangular end plates with a thickness of 15 mm and three pillars with a length of 315 mm and a diameter of 20 mm. The pillars are used to keep a fixed distance between the end plates. The top end plate has a threaded M12 hole in the center in order to mount a threaded rod with a mounting bracket. This allows for vertical adjustment of the actuator plunger, and thereby the air gap length. The bottom end plate has two threaded M8 holes that allow for bolting a mounting bracket, which holds the bottom of the actuator. Technical drawings of the components for the actuator test stand can be seen in Appendix F.

Since the behavior of the actuator is highly dependent on the reluctance of the air gap within the actuator, it is important that the deformation of the test stand during load is insignificant compared to the 2 mm air gap within the actuator. Therefore a static structural FEM study is conducted on the test stand, in order to ensure negligible displacements. The FEM study, presented in Appendix A, concludes that the deformation of the actuator test stand is 0.0297 mm which is around 1.5% of the actuator air gap. The test stand is therefore assessed to be sufficiently rigid.

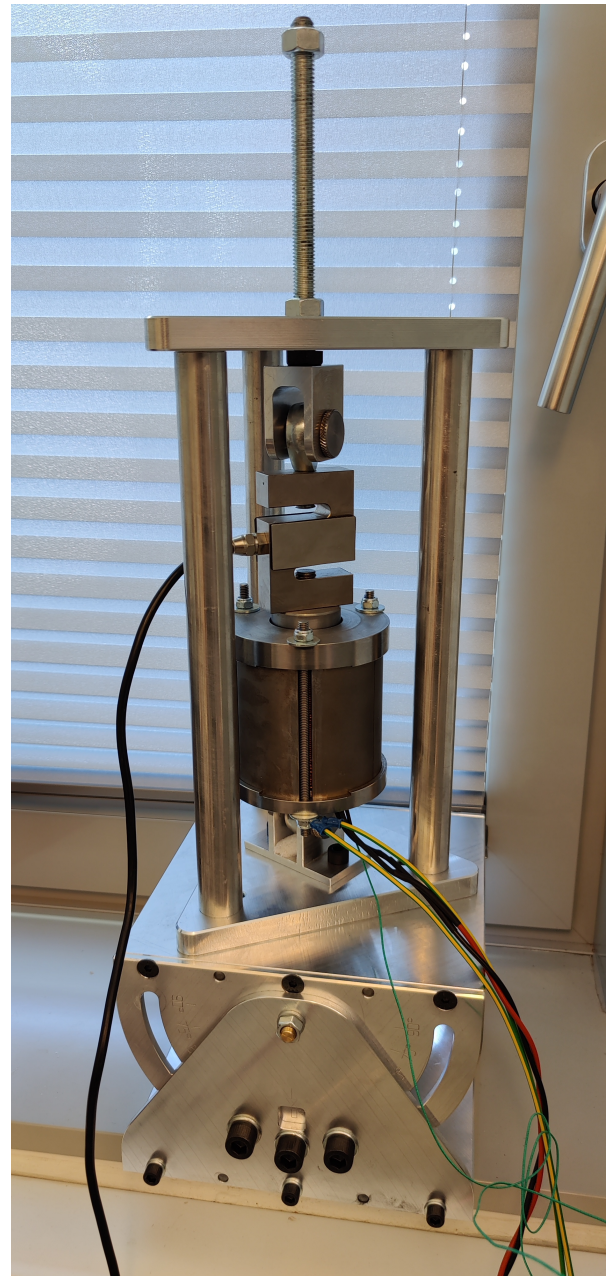


Figure 3.7. Actuator test stand with actuator mounted.

3.4 ESCON 50/5 current controller

In order to drive the current in the solenoid actuator a Maxon ESCON 50/5 module is used, as described in section 1.1. The module operates in current control mode. To maximise the performance of the electrical system, the ESCON current controller is tuned to be aggressive. The current controller inside the ESCON module is a PI-controller. There is only two settings regarding the current controller in the ESCON configuration software. The two settings are "gain" and "time constant". Neither the manual nor the configuration software elaborates on the exact meaning of these settings. The "gain" setting in the ESCON module is tuned by hand to the highest possible value which does not produce excessive noise on the output current. The final values of these settings are: gain = 10000, time constant = 30 μ s.

3.5 System identification

In order to get a general understanding of the system behavior, a series of tests have been conducted. These tests are conducted using RBS (random binary signal) inputs at different mean currents, in order to investigate the system characteristics at different operating points. For each test a unique RBS sequence is generated. The linearisation points of the tests, i.e. the mean currents, are chosen in an attempt to evenly distribute them throughout the force range. To ensure high signal to noise ratio, three tests, with different frequency content, are performed at each linearisation point. A result of a Fourier transformation of all the unique tests is shown in Figure 3.8. Note that an average of the tests with the same frequency content is presented. To prevent parameter variations due to temperature fluctuations, the tests are conducted such that the thermal load on the actuator is more or less constant throughout the test period.

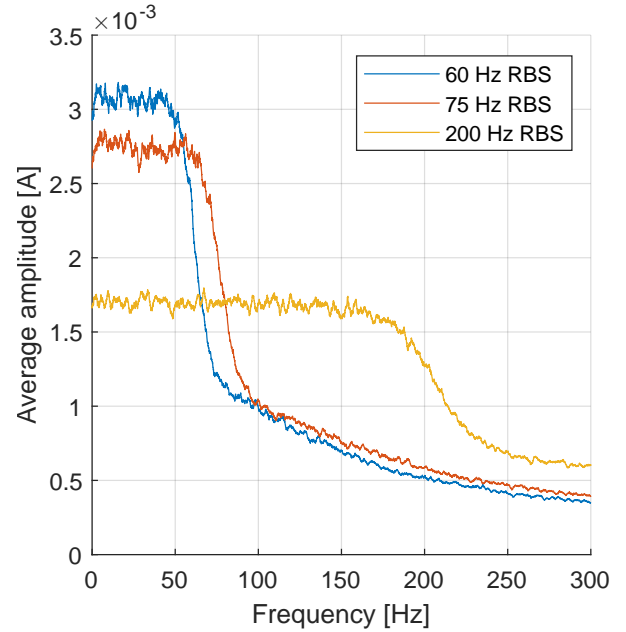


Figure 3.8. Average frequency content in the tests with 60 Hz, 75 Hz and 200 Hz RBS signals respectively. The plot is smoothed with a moving average with a window size of 1 Hz.

To ensure that the system behaves linearly around the linearisation point, the amplitude of the RBS signals are calculated to be the lowest possible. As the system is non-linear, the input to output gain, and therefore signal to noise ratio, is not constant throughout the current range. In order to ensure a good signal to noise ratio, it is necessary to have a current amplitude of at least 0.2 A and a force amplitude of at least 20 N:

- $I_{amp} > 0.2$ A peak-to-peak.
- $F_{amp} > 20$ N peak-to-peak.

The mean currents and the amplitudes are calculated using the force equation presented in chapter 1, while complying with the limits above.

3.5.1 Spectral analysis of tests

To analyse the data a spectral analysis (SPA) of the system response is performed. To prepare the data for the spectral analysis, initial transients are removed and the mean of the data sets have been subtracted to ensure zero-mean. The SPA is carried out using a Hann window with a size of 1000 samples in order to smooth the output. The frequency response of the SPA can be seen in Figure 3.9. The kinks around 1000 rad/s (≈ 160 Hz) are assumed to be caused by a mechanical eigenfrequency, presumably in the load cell. The noisy data on the right hand side of the 200 Hz mark is caused by a lack of system excitation at those frequencies.

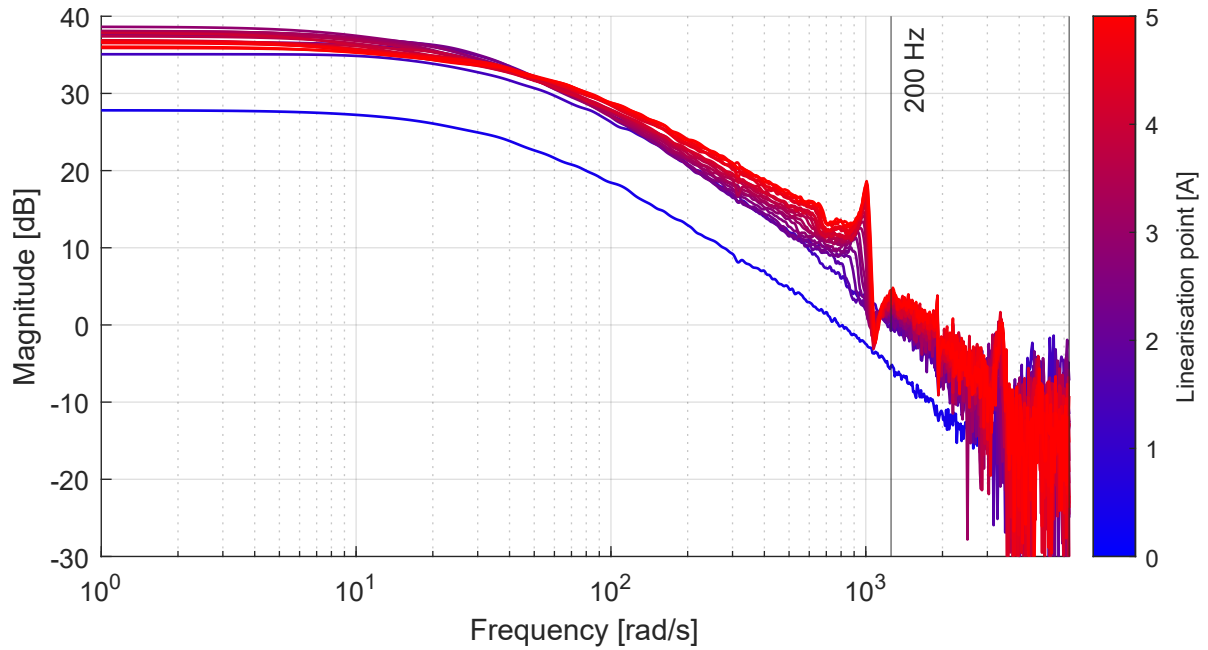


Figure 3.9. Frequency response of the SPA results.

It is also seen in Figure 3.9 that the DC gain of the system is more or less constant, with the exception of the lowest currents. This complies with the steady state current to force data shown in Figure 3.6 on page 12, where the force is approximately linear at 200 N and above. This is not expected from the force equation, Equation 1.1 on page 4, as the force should be proportion to the current squared. It is however assumed to be due to saturation in the steel increasing the reluctance of the solenoid, \mathcal{R}_{eq} .

The knowledge obtained through this spectral analysis forms the foundation for understanding the system. This knowledge is used and built upon in the following chapter to derive an analytical model describing the dynamics of the solenoid actuator.

Modelling of solenoid 4

A way a gaining knowledge about complex physical systems is to derive mathematical models based on basic physical correlations describing the dynamics of the system. Such a model helps when trying to understand how changing different parameters affects the way a system responds to different inputs. Dynamic modelling is also used in various ways to support the development of control algorithms for such systems. In general terms, the more accurate a model describes the physical system, the better control algorithms can be developed. The succeeding chapter seeks to develop a dynamic model of the solenoid actuator, described in chapter 1, based on basic physical correlations.

4.1 Nonlinear solenoid model

An electromagnetic model of the solenoid consists of two coupled systems, an electrical system that links coil voltage and current, and a magnetic system that links currents and the applied magnetic field. The governing equation of the coil can be described as a resistor-inductor circuit as shown in Figure 4.1.

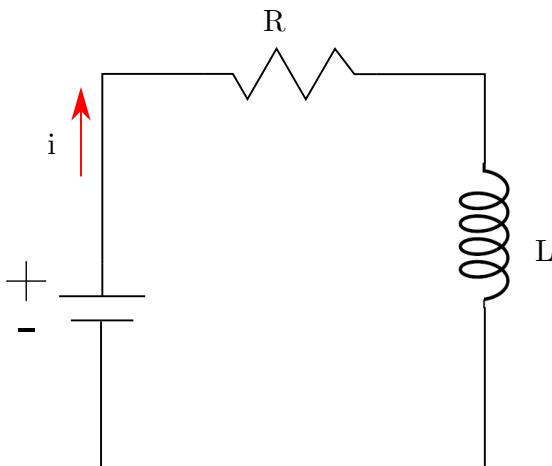


Figure 4.1. Model of electrical resistor-inductance circuit.

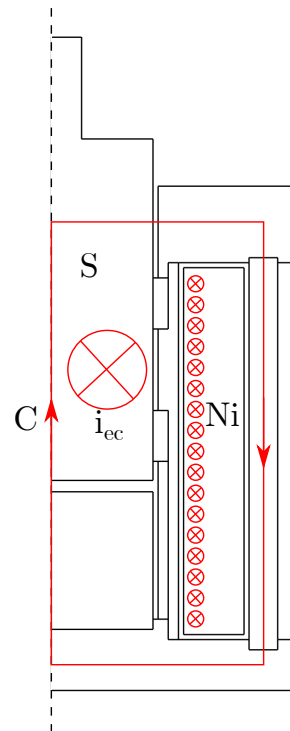


Figure 4.2. Axisymmetric actuator diagram showing windings with current and directions for currents and flux.

The equation of the resistor-inductor circuit is as follows:

$$v = R \cdot i + \frac{d}{dt} (L \cdot i) \quad (4.1)$$

Where i is the current in the coil, v is the applied voltage, R is the coil resistance and L is coil inductance. The electrical system is coupled to the magnetic system, which can be derived through the flux linkage definition:

$$\lambda = L \cdot i = N \cdot \phi \quad (4.2)$$

Where λ is the self flux linkage of the coil. From this definition, the coil self inductance, $L = \frac{N \cdot \Phi}{i}$, is defined, which can be transferred into Equation 4.1:

$$v = R \cdot i + \frac{d}{dt} \left(\frac{N \cdot \Phi}{i} \cdot i \right) \quad (4.3)$$

$$v = R \cdot i + N \cdot \frac{d\Phi}{dt} \quad (4.4)$$

Where Φ denotes the magnetic flux and N is the number of turns in the coil. The magnetic system can be modeled by the use of Ampère's circuital law (Ramirez-Laboreo, Roes, and Sagues 2019), as shown in Figure 4.2. This equation describes a coupling between the magnetic and electrical system. Ampère's model applied to the surface S and along the closed path C , shown in Figure 4.2, states that:

$$\oint_C H \, dl = \iint_S J \, dS \quad (4.5)$$

Here H is the magnetic field intensity and J is the current density. The surface integral of the current density can be simplified to an expression consisting of only two terms; current in the coil times the number of windings, Ni , and the eddy currents, i_{ec} . Since the closed path, C , consists of two fundamentally different parts, it can be reduced to two line integrals. One that covers the line integral of H in the steel, and one that covers the line integral of H in the air, which are both the working and non working air gap shown in Figure 1.6 on page 4. Using these simplifications Equation 4.5 becomes:

$$\int_{steel} H \, dl + \int_{Air} H \, dl = Ni + i_{ec} \quad (4.6)$$

According to Ramirez-Laboreo, Roes, and Sagues (ibid.), the line integral along the steel part can be approximated by an average value H_{steel} , and thereby the line integral becomes:

$$\int_{steel} H \, dl = H_{steel} \cdot l_{steel} \quad (4.7)$$

Here H_{steel} is an average H-field intensity and l_{steel} is the length of the steel path shown on Figure 4.2. The line integral within the air can be expressed as flux and reluctance in the air gaps, where \mathcal{R} denotes the reluctance:

$$\int_{Air} H \, dl = \Phi \mathcal{R}_{air} \quad (4.8)$$

Now an expression for the eddy currents is to be found. According to Ramirez-Laboreo, Roes, and Sagues (ibid.), the eddy currents can be modeled as being proportional to the rate of change in the flux, assuming that the eddy currents are uniformly distributed within the steel:

$$i_{ec} = -k_{ec} \frac{d\Phi}{dt} \quad (4.9)$$

Replacing the different terms in Equation 4.6 with the terms found in Equation 4.4 and Equation 4.7 to 4.9, a dynamic model can be derived:

$$H_{steel} \cdot l_{steel} + \Phi \mathcal{R}_{air} = N \frac{v - N \frac{d\Phi}{dt}}{R} - k_{ec} \frac{d\Phi}{dt} \Leftrightarrow \quad (4.10)$$

$$\frac{d\Phi}{dt} = \frac{\frac{N}{R} v - \Phi \mathcal{R}_{air} - H_{steel} \cdot l_{steel}}{\frac{N^2}{R} + k_{ec}} \quad (4.11)$$

Since the material models are to be based on a known H-field it is necessary to describe the dynamic model in terms of the H-field. The flux can be defined with the flux density and area, which can be inserted into Equation 4.11:

$$\Phi = B_{steel}(H_{steel}) \cdot A_{steel} \quad (4.12)$$

$$\frac{dB_{steel}(H_{steel})}{dt} A_{steel} = \frac{\frac{N}{R}v - B_{steel}(H_{steel}) \cdot A_{steel} \cdot \mathcal{R}_{air} - H_{steel} \cdot l_{steel}}{\frac{N^2}{R} + k_{ec}} \quad (4.13)$$

Here B_{steel} is an average flux density in the plunger, and A_{steel} is the cross-sectional area of the steel core. The B-field is a function of the H-field, and by the chain rule, the following can be defined:

$$\frac{dB_{steel}(H_{steel})}{dt} = \frac{dB_{steel}(H_{steel})}{dH_{steel}} \cdot \frac{dH_{steel}}{dt} \quad (4.14)$$

$$\frac{dB_{steel}(H_{steel})}{dt} = \mu'(H_{steel}) \frac{dH_{steel}}{dt} \quad (4.15)$$

Here the term $dB_{steel}(H_{steel})/dH_{steel}$ is the gradient of the BH-curve, which is defined as the incremental permeability, $\mu'(H_{steel})$ which is a function of the H-field. Applying this to Equation 4.11, gives the following:

$$\frac{dH_{steel}}{dt} \mu'(H_{steel}) \cdot A_{steel} = \frac{\frac{N}{R}v - B_{steel}(H_{steel}) \cdot A_{steel} \cdot \mathcal{R}_{air} - H_{steel} \cdot l_{steel}}{\frac{N^2}{R} + k_{ec}} \Leftrightarrow \quad (4.16)$$

$$\frac{dH_{steel}}{dt} = \frac{\frac{N}{R}v - B_{steel}(H_{steel}) \cdot A_{steel} \cdot \mathcal{R}_{air} - H_{steel} \cdot l_{steel}}{\left(\frac{N^2}{R} + k_{ec}\right) \mu'(H_{steel}) \cdot A_{steel}} \quad (4.17)$$

If it is possible to control the current in the coil, the dynamics of the electrical system can be neglected in the equation and thereby Equation 4.4 can be ignored. The dynamics of the electrical system will instead be implicitly included in the applied current. Going through the same procedure as described above gives the following model, with a current input instead of a voltage input:

$$\frac{dH_{steel}}{dt} = \frac{N \cdot i - B_{steel}(H_{steel}) \cdot A_{steel} \cdot \mathcal{R}_{air} - H_{steel} \cdot l_{steel}}{k_{ec} \cdot \mu'(H_{steel}) \cdot A_{steel}} \quad (4.18)$$

This model describes the dynamics of the H-field within the plunger. In order to find the resulting force of the solenoid actuator, the H-field in the plunger must be converted into a B-field in the air gap. The plunger B-field can be extracted from the model, and based on FEM simulations it is found that there is an almost constant relationship between the B-field in the plunger, B_{steel} , and the B-field in the air gap, when the air gap length is kept constant. The relationship, called the knock-down factor, is from the simulation found to be:

$$kd = \frac{B_{ag}}{B_{steel}(H_{steel})} = 0.83 \quad (4.19)$$

As described in Equation 1.1 the solenoid actuator force can be expressed in the terms of the flux density in the air gap. The equation is repeated below for convenience:

$$F = \frac{B_{ag}^2 A_{pl}}{2\mu_0\mu_{air}} \quad (1.1)$$

The force can be expressed with the flux density in the plunger and the knock-down factor:

$$F = \frac{(B_{steel}(H_{steel}) \cdot kd)^2 A_{steel}}{2\mu_0\mu_{air}} \quad (4.20)$$

4.2 Model parameters

In the model described by Equation 4.18 the change in H-field can be calculated based on the applied current, i , but a number of parameters are to be determined before it can be utilised.

The parameters N and R are coil parameters, that can be counted and measured. The plunger area, A_{steel} , and the length of the flux path within the steel, l_{steel} , are calculated from the solenoid geometry. The air gap reluctance, \mathcal{R}_{air} , is found from a FE model which also takes phenomena as fringing and flux leakage into account. The parameters are as seen in Table 4.1:

Parameter	Value
N	560
R	1.77 Ω
A_{steel}	$1.26 \times 10^{-3} \text{ m}^2$
l_{steel}	0.23 m
\mathcal{R}_{air}	$1.28 \times 10^6 \text{ H}^{-1}$

Table 4.1. Values found for the different parameters.

In Equation 4.18 the two terms $B_{steel}(H_{steel})$ and $\mu'(H_{steel})$ remains to be determined. Both parameters are dependent on the specific material and the H-field. Therefore a material model is needed in order to calculate $B_{steel}(H_{steel})$ and $\mu'(H_{steel})$ for a given H-field. The variable k_{ec} is accounting for the eddy currents within the solenoid. When the other parameters are found, k_{ec} can be determined based on experimental data from the solenoid.

4.2.1 Material models

The dynamic model presented in Equation 4.17 expresses the changes in the H-field in the plunger as a function of the different material parameters and the coil current. These material parameters can be divided into parameters describing the relationship between the H-field and the B-field, and then the parameter k_{ec} , that describes the eddy currents. The B-field within the steel is dependent on the specific material and can be divided into two different contributions. One is the BH-curve of the material which defines the magnetic saturation within the steel, denoted B_{rev} . The second is the material hysteresis which describes the history dependency of the (de)magnetisation of the steel, denoted B_{irr} . The succeeding section is going to derive an expression for B_{rev} , before a classic Preisach model (CPM), capable of modelling hysteresis, is developed. Hereafter these two models are merged in order to obtain a generalised Preisach model (GPM). The variable B_{rev} describes the BH-curve and the generic shape of such a curve for ferromagnetic material is shown in Figure 4.3. The following expression shows how the B-field is calculated with the GPM:

$$B = f_{GPM} = B_{rev} + B_{irr} \quad (4.21)$$

$$\mu' = \mu'_{GPM} = \mu_{rev} + \mu_{irr} \quad (4.22)$$

For both expressions it can be seen that there is a contribution from the reversible term, which describes the saturation, and the irreversible term, describing the hysteresis.

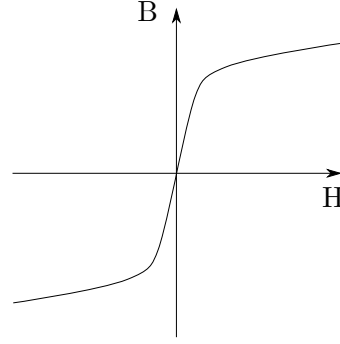


Figure 4.3. A generic model of a ferromagnetic material.

The accuracy of the dynamic solenoid actuator model relies on the accuracy of the material model. Magnetic material data for the structural steel used in the solenoid is not available. Therefore a series of tests are conducted in order to determine the magnetic material properties of the S235 steel used to manufacture the solenoid actuator. A test report is found in Appendix B.

According to Ramirez-Laboreo, Roes, and Sagues (2019) the generic shape shown in Figure 4.3 can be described by the following model:

$$B_{rev}(H) = \mu_0 H + \text{sign}(H)\mu_1 H_1 \left(1 - e^{-\frac{|H|}{H_1}}\right) + \text{sign}(H)\mu_2 H_2 \left(1 - e^{-\frac{|H|}{H_2}}\right) \quad (4.23)$$

Equation 4.23 has the advantage that the derivative, which is the incremental permeability, is analytically defined and therefore $\mu_{rev}(H)$ is easily found:

$$\frac{dB_{rev}}{dH} = \mu_{rev}(H) = \mu_0 + \mu_1 e^{-\frac{|H|}{H_1}} + \mu_2 e^{-\frac{|H|}{H_2}} \quad (4.24)$$

From Equation 4.23 and 4.24 it can be seen that this model ensures, that the material permeability tends towards the vacuum permeability, μ_0 , as the H-field tends towards infinity. The four model parameters, μ_1 , μ_2 , H_1 and H_2 is determined by fitting the model structure to a series of material tests. The material tests are conducted as described in Appendix B. To determine the parameters, an optimisation algorithm is developed in order to minimise the least square difference between the modeled B-field and the measured B-field. Since the objective function proved to have a lot of local minima, a global minimisation algorithms, called particle swarm, is utilised. The best fit is found to be with the following parameters: $\mu_1 \approx 2.217 \times 10^{-5} \text{ H m}^{-1}$, $\mu_2 \approx 1.432 \times 10^{-3} \text{ H m}^{-1}$, $H_1 \approx 2.092 \times 10^5 \text{ A m}^{-1}$ and $H_2 \approx 1.080 \times 10^3 \text{ A m}^{-1}$. The proposed material model for the BH-curve is shown with the green line in Figure 4.4.

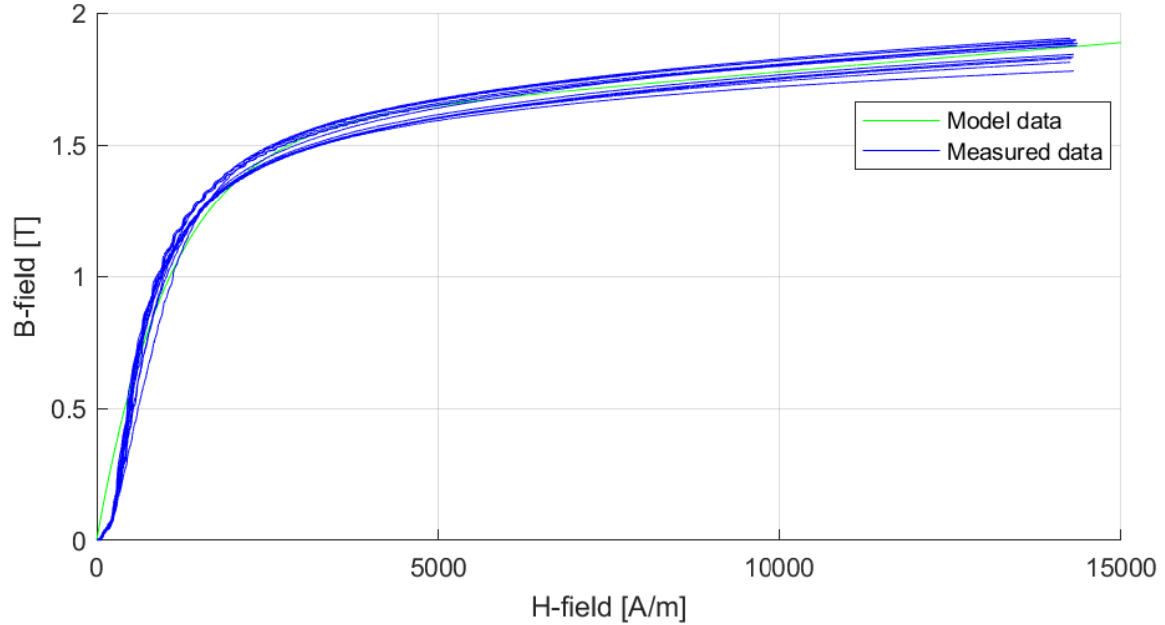


Figure 4.4. The blue lines indicates measured values from experiments and the green line is the modeled BH-curve.

Figure 4.4 shows that the fitted material model describes the majority of the measured data well. It is also noticed that there are some deviations, especially in the region where the H-field is small. The measured material data seems to be consistent regarding the shape, across all the different tests. This indicates that it is an actual material property, but it cannot be modelled by Equation 4.23. It is assessed that the present model captures enough of the material properties to be used as the BH-curve, especially compared to the added complexity it would take to model the kink in the region with low H-field values. It is worth mentioning that this model does not contain any information about hysteresis in the metal, wherefore this is further examined in the following section.

Material model including hysteresis

Ramirez-Laboreo, Roes, and Sagues (2019) proposes a CPM, which is a mathematical tool used that is capable of modeling hysteresis in ferromagnetic materials. The fundamental challenges when modelling hysteresis is to incorporate the history of the applied H-field on the material and knowing how to utilise this history in order to calculate the present value of the B-field. The CPM is capable of doing that, and is therefore utilised here. In order to gain an intuitive understanding of how the CPM works a discretised example is examined before the final continuous model is derived. In the following, the output of the CPM will be f_{CPM} and the output of the GPM will be f_{GPM} . For both models the output will be the B-field in the material at a given time.

The hysteresis can be envisioned as a series of very small magnetic domains that either has the value γ or $-\gamma$ depending on the present and prior magnetic field. These domains are represented as non-ideal relays, called hysterons, with different thresholds denoted (β_n, α_n) , as shown in Figure 4.5.

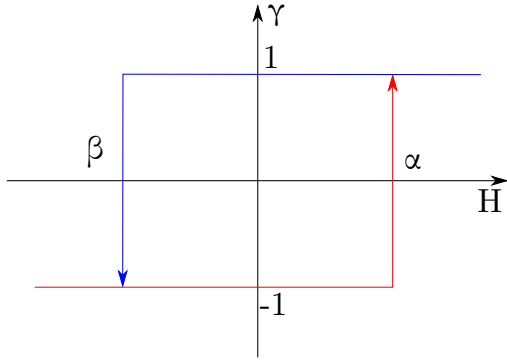


Figure 4.5. A non-ideal relay (hysteron) with thresholds, α and β .

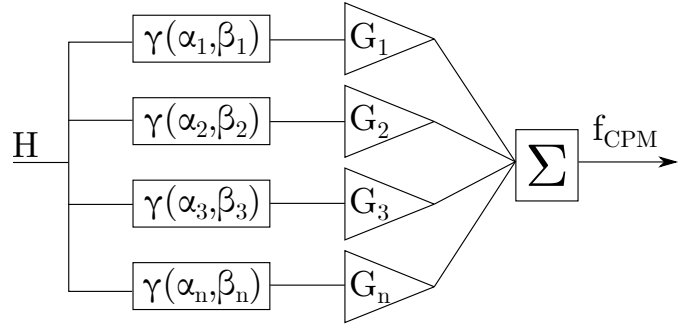


Figure 4.6. A weighted sum of hysterons that gives the output of the CPM.

The (β_k, α_k) values are magnetic field thresholds, which are the bounds at which the output of the hysterons switches between γ and $-\gamma$. Here the hysteresis is modeled as multiple parallel coupled hysterons, where a weighted sum of the hysterons give the current B-field as shown in Figure 4.6. The weights for hysterons are represented with $G_1, G_2 \dots G_n$ in the figure. The shape of the hysteresis curve is determined by the weighting of each hysteron.

In order to visualise the hysterons and the history of the H-field, a Preisach plane is used, as seen in Figure 4.8. The Preisach plane serves to illustrate which hysterons are active ($+\gamma$ value) and which are inactive ($-\gamma$ value). The hysterons are represented as the red crosses. If the hysterons are inside the blue area they are active and if they are inside the red area they are inactive. The threshold values of the hysterons, (β_k, α_k) , defines their coordinate in the Preisach plane. In the plane, the point $(H(t), H(t))$ represents the present magnetic field intensity and moves along the green line. So for an H-field input, as the one shown in Figure 4.7, the Preisach plane will look like the one shown in Figure 4.8. The B-field can be found at a given time, t , by adding the weighted values of the active hysterons (crosses in the blue area) and subtracting the weighted values of the inactive hysterons (crosses in the red area).

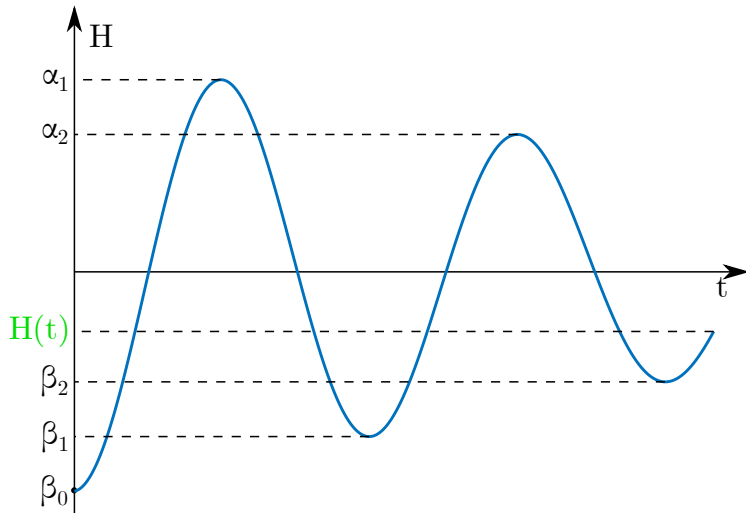


Figure 4.7. An arbitrary input of a H-field over time to the CPM, where α and β are the local maxima and minima.

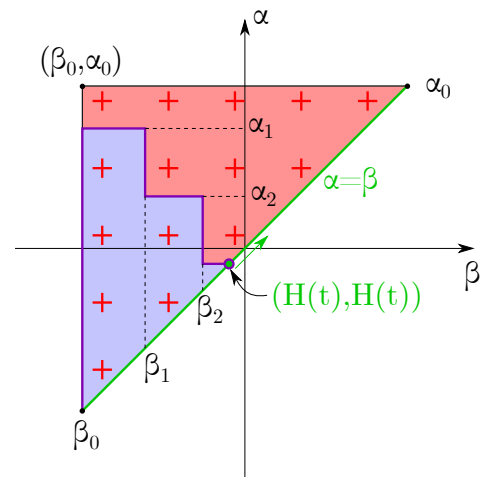


Figure 4.8. The Preisach plane, showing hysterons as red crosses and history of the magnetic field as α and β levels.

Preisach model with distribution functions

If the hysterons are weighted equally, the shape of the hysteresis loop can also be determined by the placement of the hysterons in the Preisach plane. The placement is defined with a Preisach function, $P(\alpha, \beta)$. Typically the Preisach function is expressed as the product of two probability density functions, and thereby these distribution functions defines the shape of the hysteresis loop. According to Ramirez-Laboreo, Roes, and Sagues (2019) and Pruksanubal, Binner, and Gonschorek (2006) the use of two Cauchy distribution functions is the best fit for most ferromagnetic materials, and therefore these are used in the present project.

The mathematical equations used to implement the Preisach model based on distribution functions are presented in Appendix C. From the equations shown in Appendix C it is seen that the GPM contains five additional material parameters aside the four parameters that are already found in the reversible material model. These parameters are m_{h_m} , s_{h_m} , m_{h_c} , s_{h_c} and \hat{B}_{irr} . According to Ramirez-Laboreo, Roes, and Sagues (2019), m_{h_m} must be equal to zero, in order to obtain a major hysteresis loop that is symmetrical, and therefore the four remaining parameters are to be determined.

Similarly to the parameters for B_{rev} , this is done by fitting the model to experimental data by the means of an optimisation algorithm. The experimentally obtained hysteresis curve is found as described in Appendix B, whereafter several different approaches is used to fit the model parameters. MATLAB's global optimisation algorithm "particle swarm" is used since the objective function, which is defined as a sum of least squares, has many local minima. Initial attempts to reuse the reversible material parameters found in subsection 4.2.1 showed poor results wherefore an optimisation algorithm with all eight material parameters is used. Figure 4.9 shows the hysteresis data obtained in Appendix B and the hysteresis model on top of it. The values used for the material parameters in this model can be seen in Table 4.2.

Parameter	Value
μ_1	10 H m^{-1}
μ_2	-10 H m^{-1}
H_1	$9.640 \times 10^8 \text{ A m}^{-1}$
H_2	$7.372 \times 10^8 \text{ A m}^{-1}$
\hat{B}_{irr}	1.617 T
s_{h_m}	249.6
m_{h_c}	331.8
s_{h_c}	149.0

Table 4.2. Values found for the material parameters.

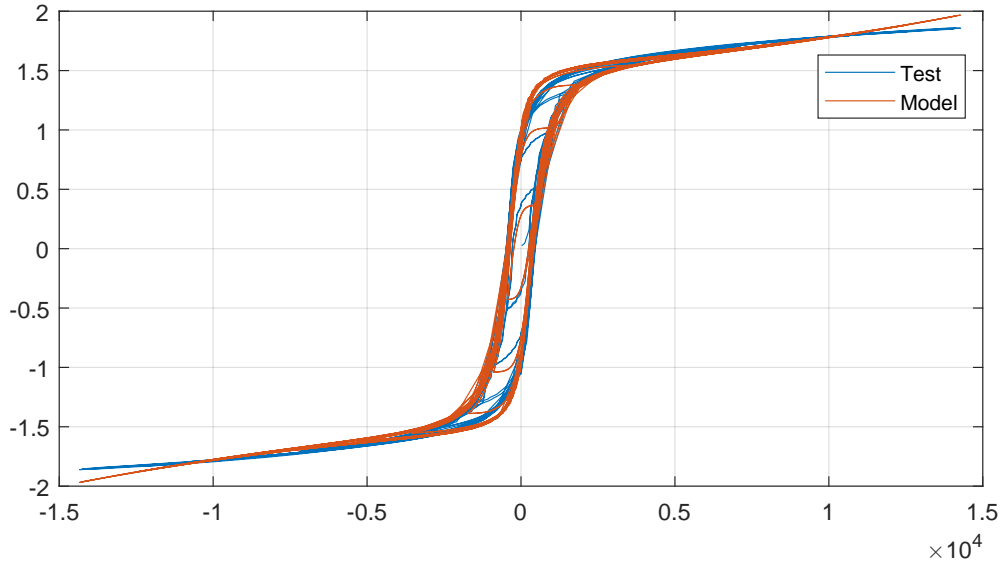


Figure 4.9. Hysteresis loop. Data from the material test is shown as the blue line while the modelled material behavior is marked as the orange line.

Figure 4.9 shows measured and modelled magnetic material properties of the the S235 steel. It is seen that the model does not fit perfectly to the measured data, but it captures significantly more of the magnetic material properties than B_{rev} alone. The full solenoid actuator model is validated in the following section.

4.3 Model validation

The eddy current constant k_{ec} is found by minimising the difference between the modeled actuator force and the experimentally measured force. Here Equation 4.18 and 1.1 are used to model force with the current as an input. In order to ensure that the eddy current dynamics are excited, a series of random steps between 0-5 A on the current input is applied to the actuator while the resulting force is measured. The eddy current constant, k_{ec} , is found as the value that allows for the least square error between the measured and modeled force value.

When using the fitted k_{ec} value, the results of comparing the measured and modeled force, shows the correct dynamics but an incorrect gain. The gain of the model is not governed by the k_{ec} value. Among the remaining parameters it is assessed that the error is due to incorrect values for the air gap reluctance, \mathcal{R}_{air} , and the knock-down factor, kd , as these has been approximated from an FE model, while the other parameters are either measured or calculated from the geometry. Therefore another optimisation algorithm is designed where all three parameters, k_{ec} , kd and \mathcal{R}_{air} , are variables. This algorithm is gradient based and uses the least square error of the force as objective function. The values of the parameters are shown in Table 4.3:

Parameter	Value
k_{ex}	54 479 A V ⁻¹
kd	0.80
\mathcal{R}_{air}	1 308 969 H ⁻¹

Table 4.3. Values found for the different parameters.

It is noticed that both kd and \mathcal{R}_{air} are relatively close to the values found from the FE model, but both are changed such that the resulting output force has a lower DC gain.

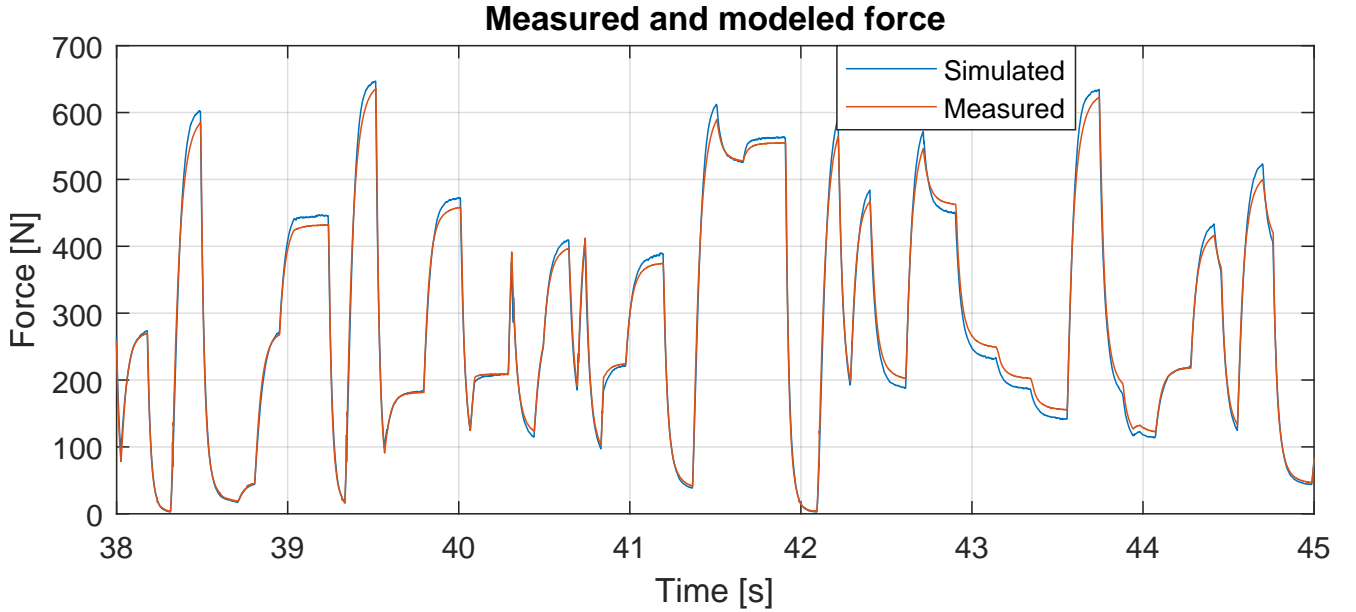


Figure 4.10. Simulated and measured force response for a sequence of random input currents, where the simulation is based on the GPM.

Figure 4.10 shows that the model captures a significant amount of both the dynamics and magnitudes of the solenoid actuator. The model generally fits very well with a few deviations, especially where the forces are high. The root mean square error (RMSE) between the measured and the simulated force is found to be:

$$RMSE = \sqrt{\frac{\sum_{i=1}^k (F_{measured_i} - F_{model_i})^2}{k}} = 12.1 \text{ N} \quad (4.25)$$

The RMSE can be seen as an average error between the solenoid model the measured data. This means that, compared to the full scale value of 600 N, there is an average error of 2%.

Reducing the computational time of the model

It is worth noting that the solenoid model containing the hysteresis material model is very computationally expensive. It is therefore questionable whether it is possible to implement this model on a real time target for use in control, which is presented in chapter 7. Especially the sums shown in Equation C.8 and C.9 takes a lot of processing power, and the simulation of a 60s test takes 3769s on a laptop in MATLAB Simulink. Therefore it is of interest to investigate the performance of a solenoid model where the nested material model does not take hysteresis into account, but only uses the B-H curve and permeability described in Equation 4.23 and 4.24.

The parameters, k_{ex} , kd and \mathcal{R}_{air} should not change due to the model change. However using the same values in the model without hysteresis, these parameters might try to compensate for inaccuracies in the model including hysteresis. It is therefore necessary to fit the parameters again on experimental data, such that they will not try to compensate for inaccuracies in the previous model, but rather the new model. The same procedure as described above is used here, and the parameters are as shown in Table 4.4.

Parameter	Value
k_{ex}	57 893 A V ⁻¹
kd	0.73
\mathcal{R}_{air}	1 044 395 H ⁻¹

Table 4.4. Updated model parameters.

Figure 4.11 shows a segment of the modeled system response compared to measured validation data. It is noticed that the model underestimates the highest forces. A possible explanation to this is that a small play in the mounting of the actuator or elastic deformation would result in a change in the air gap. This would change both the reluctance and knock-down factor and could thereby explain why the model predicts a lower force at higher currents. At the medium to low range the model generally overshoots the forces. This could be explained by the fact that the steel has an amount of hysteresis that is not insignificant, which is not included in the present model. Regarding these two potential sources of inaccuracy, the play and elastic deformation is the most difficult to incorporate in the model, especially when the actuator is incorporated in the larger test bench.

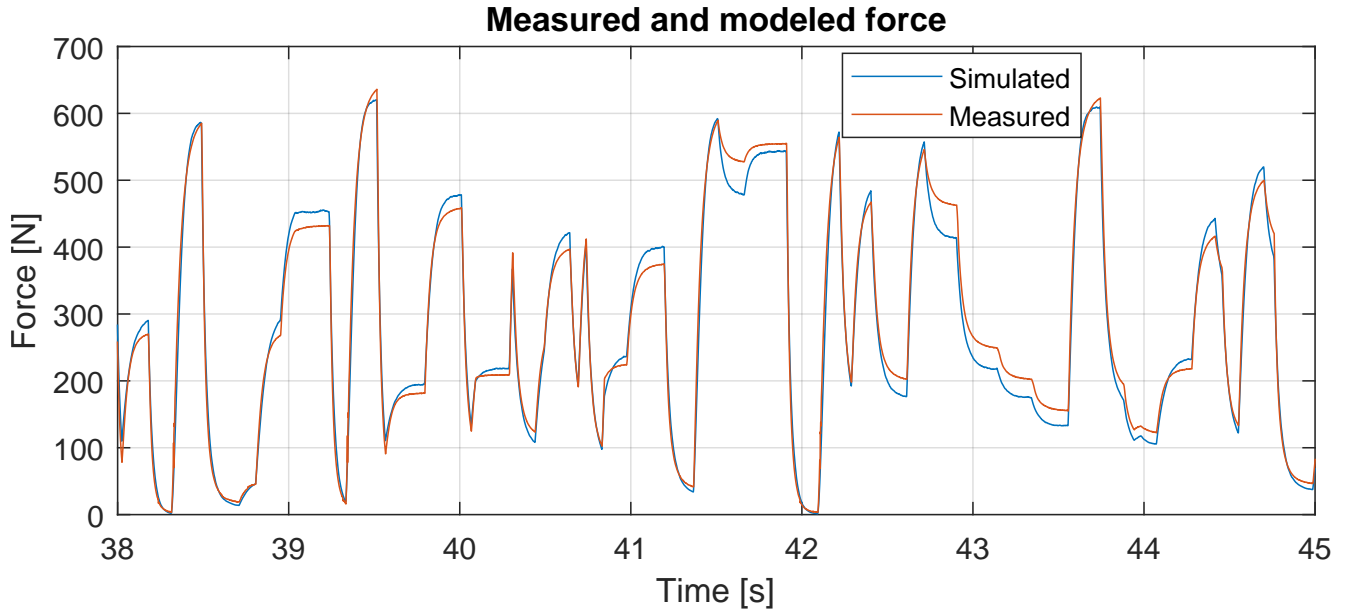


Figure 4.11. Simulated and measured force response for a sequence of random input currents, where the simulation is based on the CPM.

The RMSE between the simulated and measured force is found to be:

$$RMSE = 18.0 \text{ N} \quad (4.26)$$

This model without the hysteresis is not nearly as computationally heavy as the one accounting for hysteresis, and as a reference, simulating 60s with this material model takes 2.96s while the same simulation of the solenoid model including the hysteresis model takes 3769s. The model that does not account for hysteresis has an average error of 3% of the full scale force of 600 N. Since the model not accounting for hysteresis still is a good representation of the solenoid actuator, and demands significantly less processing power in order to run as a real time application compared to the one accounting for hysteresis, it is used in the succeeding work.

4.4 Subsidiary conclusion

A non-linear solenoid model has been derived capable of modelling the output force based on either a current or a voltage input to the solenoid, where the current to force model is the one being used in the succeeding work. The solenoid model proposed initially includes a material model based on a generalised Preisach material model. This model is found to be the best fitting material model. However, due to a disproportionate computational requirement, it is complicated to implement the model on a real time target. Instead a simpler model, which does not include hysteresis but only the BH-curve, is used. This solenoid model without hysteresis demonstrated to have a root mean square error of 18 N compared to actual tests, when subjected to a random input current between 0 A and 5 A, which is deemed reasonable.

Transient analysis of solenoid geometry 5

In chapter 4 a dynamic model of the solenoid is presented. The model is based on a set of lumped parameters, which describe the main characteristics of the system. Here the model is verified with experimental data, where it is shown to accurately model the system response. The approach to determine the values for the parameters in the governing equation was through the use of data fitting. While this approach leads to satisfactory results, it lacks the possibility of predicting the impact of changes in for example the geometry of the solenoid. This applies for the three values; k_{ec} , kd and \mathcal{R}_{air} , as these are not explicitly defined in terms of geometry, but instead experimentally fitted. It would require a prototype to be manufactured in order to determine the impact of changes in the solenoid using the model.

In order to analyse the solenoid geometry a finite element model and analysis through COMSOL is utilised. In COMSOL a model of the solenoid is built and simulated. As this is an electromagnetic problem, the approach is to solve the Maxwell equations for a given domain subjected to a set of boundary and initial conditions. The finite element software is utilised as a tool for improving the solenoid dynamics, and will serve as an addition to the analytical model and the experimental work.

5.1 Electromagnetic finite element analysis

The following analysis are using the transient electromagnetic solver in COMSOL's AC/DC module. While the fundamentals of the solver and the governing equations are not reviewed, the boundary conditions and the constitutive relations are presented. In this project both 2D, 2D axisymmetric and 3D models are used, however material models and boundary conditions remain the same for each. As the movement of the plunger is neglected in the project, as described in section 2.1, the plunger is not allowed to move in the COMSOL model. Therefore, there is no need for mechanical properties, only the electromagnetic properties and boundary conditions are necessary.

For both the axisymmetric and 3D model the boundary conditions are chosen to be the program default option of magnetic insulation. This condition enforces the boundary of the model to be perfectly insulated, meaning the magnetic vector potential (the field variable of a magnetic problem) is zero normal to the boundary (COMSOL 2016). The magnetic field cannot enter or exit the boundary, as this can be interpreted as a boundary to a domain of infinite electrical conductivity (*ibid.*). Another option is a boundary condition of perfect magnetic conduction, which in principle is the opposite condition, meaning that no current can flow in the boundary. These boundary conditions are applied to an air domain around the solenoid. According to COMSOL (*ibid.*) the choice of the two conditions does not matter if the surrounding air domain is big enough. Then similar results will be obtained. In order to reduce the amount of elements needed to mesh a large air domain, COMSOL has a feature to artificially create an air domain of infinite size, by the use of coordinate stretching. This requires much fewer elements, and by using this feature, one can choose either of the boundary conditions.

5.1.1 Material models

In terms of constitutive models the ones of importance are the relation between the current density, J , and the electrical field, E , as well as the relation between the flux density, B and the magnetic field H . The material model for the steel, used in the solenoid actuator, is based on a experimentally determined BH-curve, described in Appendix B. For the remaining materials in the model, the magnetic permeability is orders of magnitude lower than steel and close to the vacuum permeability. Therefore program default values are used, as these values are insignificant for the result of the model. For the relation between the current density and the electrical field, the following applies (COMSOL 2018):

$$J = \sigma E \quad (5.1)$$

Where σ is the electrical conductivity of the specific material. The electrical conductivity is here written as a scalar, however COMSOL supports the possibility of anisotropic materials. For the purpose of this model, the solenoid consists of electrically isotropic materials, except for the copper wire which is enameled.

For the steel, copper and aluminium material the conductivity are to be determined. Disregarding the frequency and temperature dependence, the conductivity is found as:

$$\sigma = \frac{1}{\rho} = \frac{L}{A \cdot R} \quad (5.2)$$

Where ρ is the resistivity of the material, A is the cross sectional area, L is the length and R is the resistance. In order to achieve satisfactory measurements of the resistance, the test specimen has to have a small cross sectional area and be relatively long. A series of specimens of the steel material suitable for this experiment was available, however no suitable aluminium specimens could be found. From the experiments of the steel specimens, the conductivity of the steel material is found to be 5.32 MS m^{-1} , as described in Appendix D. For the electrical conductivity of the aluminium material, the value is adjusted in COMSOL, such that the results match experimental data from the solenoid actuator. The conductivity is found to be 18 MS m^{-1} , which is within realistic bounds for aluminium conductivity (NDT Supply.com 2002).

5.2 Analysis of solenoid system

With the fundamental definitions for the FE models above, an axisymmetric 2D model and 3D model of the solenoid are created. To verify the model, three consecutive experiments are conducted, with a current step input of 1 A, 2.5 A and 5 A, respectively. It is noted that all simulations with a current step input within COMSOL is neglecting the dynamics of the electrical build up of current. This means that e.g. with a 5 A step input, the current in the coil will be 5 A instantly. This cannot happen in reality as the coil will have some inductance preventing an instantaneous change in current.

The simulation with the 5 A step input is used as a reference for manually adjusting the electrical conductivity of the aluminium. The best value for the conductivity is then used for simulating the system at the other current inputs. The results are shown in Figure 5.1. In the simulations the air gap has been adjusted to achieve the same DC force. This is done as it is difficult to precisely measure the air gap length during the experiments. This applies to measuring both the initial air gap length as well as taking into account the deformation of the test setup during an experiment.

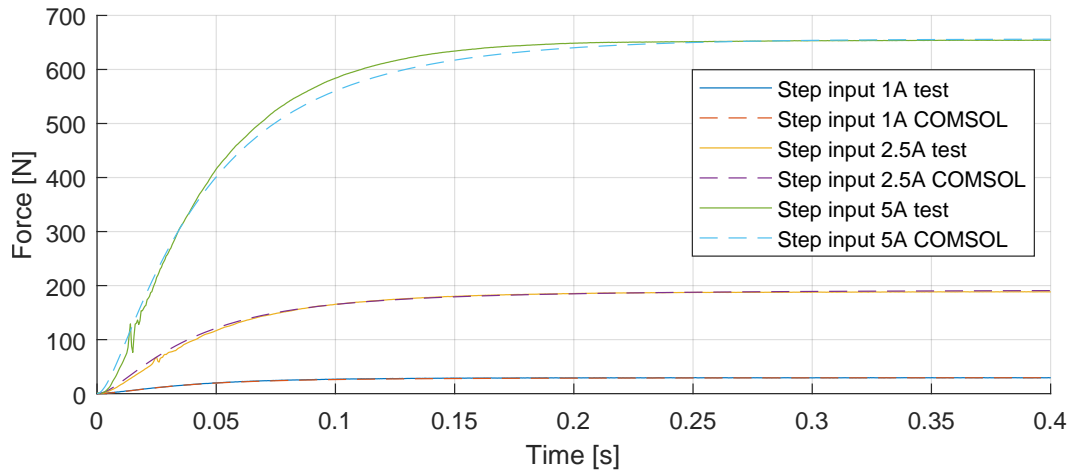


Figure 5.1. Comparison of model response and experiments at different current inputs.

While some difference between the model and the experimental results are observed, the settling time of the reference experiment at 5 A is similar to the simulation. Using the same material data for the two other step responses shows a similar satisfactory behaviour. Generally the model seems to model the system adequately, meaning the COMSOL model can be used to analyse the influence of geometry changes.

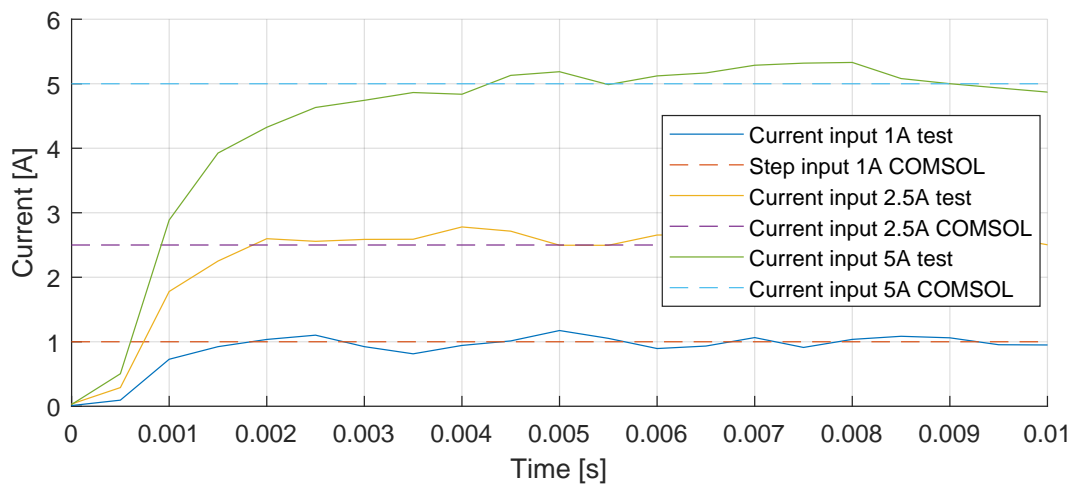


Figure 5.2. Comparison of current in model response and experiments at different current inputs.

In Figure 5.2 the belonging current responses to the experiments and the COMSOL simulations are shown. While the current in COMSOL is instantly at the reference current, some dynamics are seen in the current responses of the experiments. Here settling times in the order of 2 ms to 4 ms are observed. These settling times are significantly faster than the settling times for the forces, which all are approximately 130 ms. The assumption of an instantaneous rise in the current in COMSOL is therefore deemed to be acceptable, as it is only a few milliseconds in the beginning where the model is inaccurate.

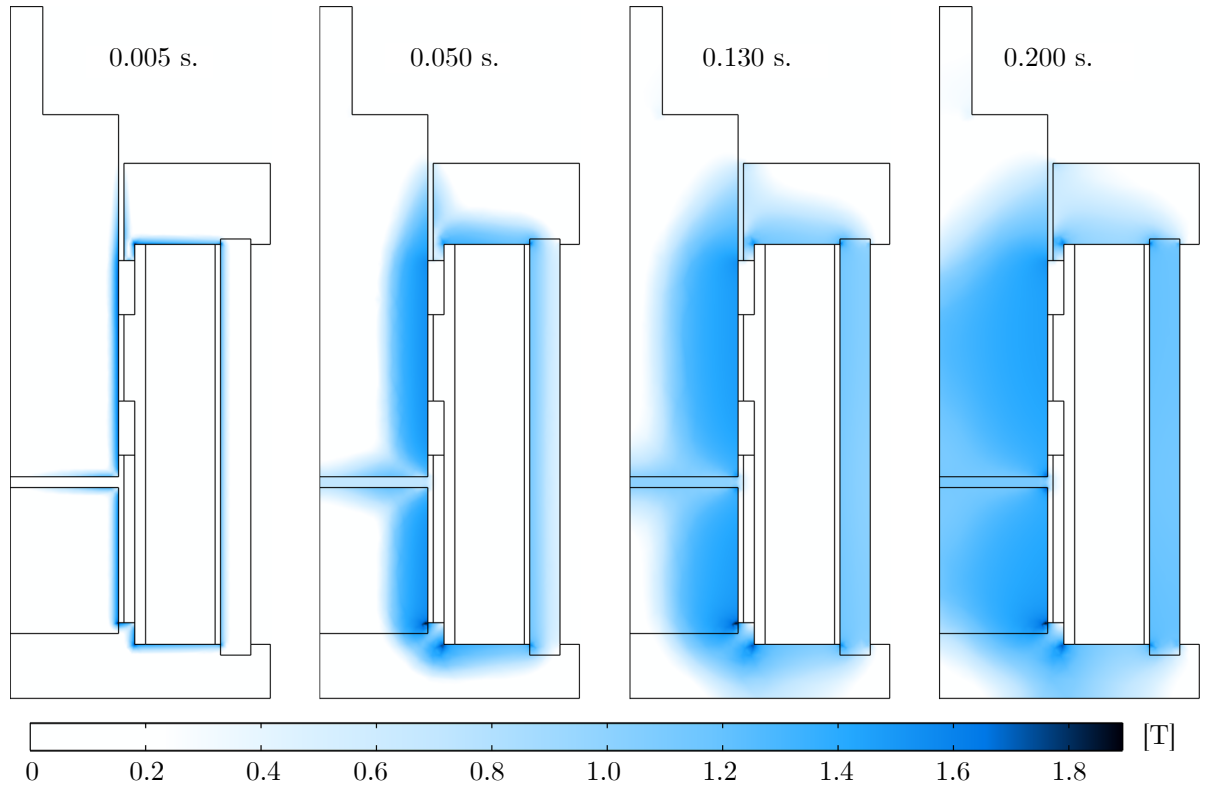


Figure 5.3. Transient development of flux density in the solenoid.

In Figure 5.3 the transient magnetic field in the solenoid actuator is displayed. Here it is seen that the field diffuses into the solenoid starting from the copper coil. It is also noticed that there is a time delay before a significant amount of flux is present in the air gap. The speed of the magnetic field diffusion is delayed by the induced eddy currents. This is the skin effect, which is also observed in wires conducting currents at a high frequency, where the currents are only running on the surface of the wire. Similarly the magnetic field is initially only present close to the coil. This effectively means that the reluctance of the system is very high in the beginning, as the magnetic field is severely suppressed. This has an important influence on the electrical system, due to the relationship between the inductance and reluctance, which can be deduced from Equation 4.2 on page 17 which is repeated below:

$$L = \frac{N \cdot \phi}{i} \quad (4.2)$$

The flux, ϕ , can be expressed in terms of the MMF and the reluctance:

$$\phi = \frac{N \cdot i}{\mathcal{R}} \quad (5.3)$$

Where \mathcal{R} is the reluctance of the structure. Combining Equation 4.2 and 5.3:

$$L = \frac{N^2}{\mathcal{R}} \quad (5.4)$$

In Figure 5.4 and 5.5 the reluctance and inductance from the simulation with 5 A step input is shown. Both values changes with a factor of ~ 37 from the initial to the final value. These changes in the values influences both the magnetic and electrical system. The objective is to speed up the magnetic system, which can be achieved by reducing the eddy currents. This reduction must be visible as a decrease in the transient reluctance values. Reducing the transient reluctance will in accordance to Equation 5.4 lead to an increased transient inductance value, which will slow the electrical system.

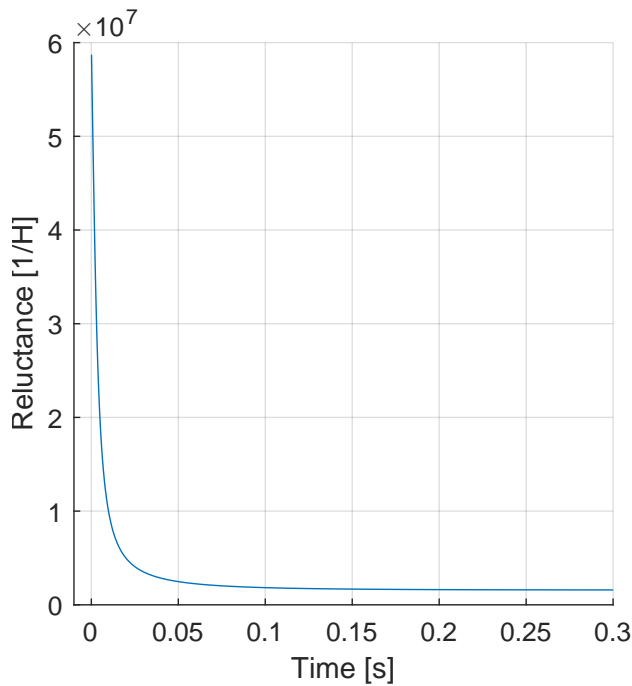


Figure 5.4. Reluctance value during a step.

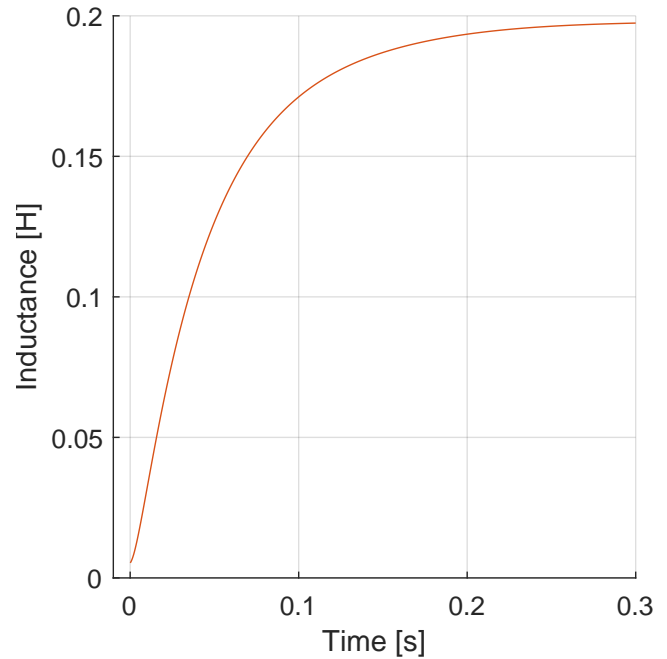


Figure 5.5. Inductance value during a step.

5.2.1 Analysis of eddy currents

In Figure 5.6 a plot of the current density norm in all parts of the solenoid, except the coil, is displayed. Here it is seen that the currents originates close to the copper coil initially, and over time dissipates into the steel parts and eventually vanishes as the magnetic field settles (no change in magnetic field, no induced currents). It is especially notable that the current density is initially high in the aluminium parts of the solenoid compared to the other components. This indicates that an inexpedient design choice was taken during the design of the solenoid in the former project. The aluminium tubes acts like a short-circuited coil, and due to the relatively high electrical conductivity of aluminium, some quite significant eddy currents are induced. The currents in the aluminium tubes then creates a magnetic field in the opposite direction, which opposes the magnetic field from the copper coil, and thereby suppresses the magnetic fields in the plunger.

While the eddy currents in the aluminium tubes initially are of highest intensity, there are also currents present in all other steel parts as seen on Figure 5.6. As this is a plot of the current density, which is the currents per surface area, it has to taken into account that currents in bigger components like the center piece and the plunger also contributes to a high amount of the currents. This is more prominent at the 0.050 s time step.

An idea to reduce the eddy currents in the plunger and center piece is proposed in the former project as explained in chapter 1, and shown on Figure 1.10 and 1.11 on page 6. Here cuts are introduced to the plunger. This idea is treated separately in chapter 6. However an analysis and improvement of the aluminium tube design is presented below.

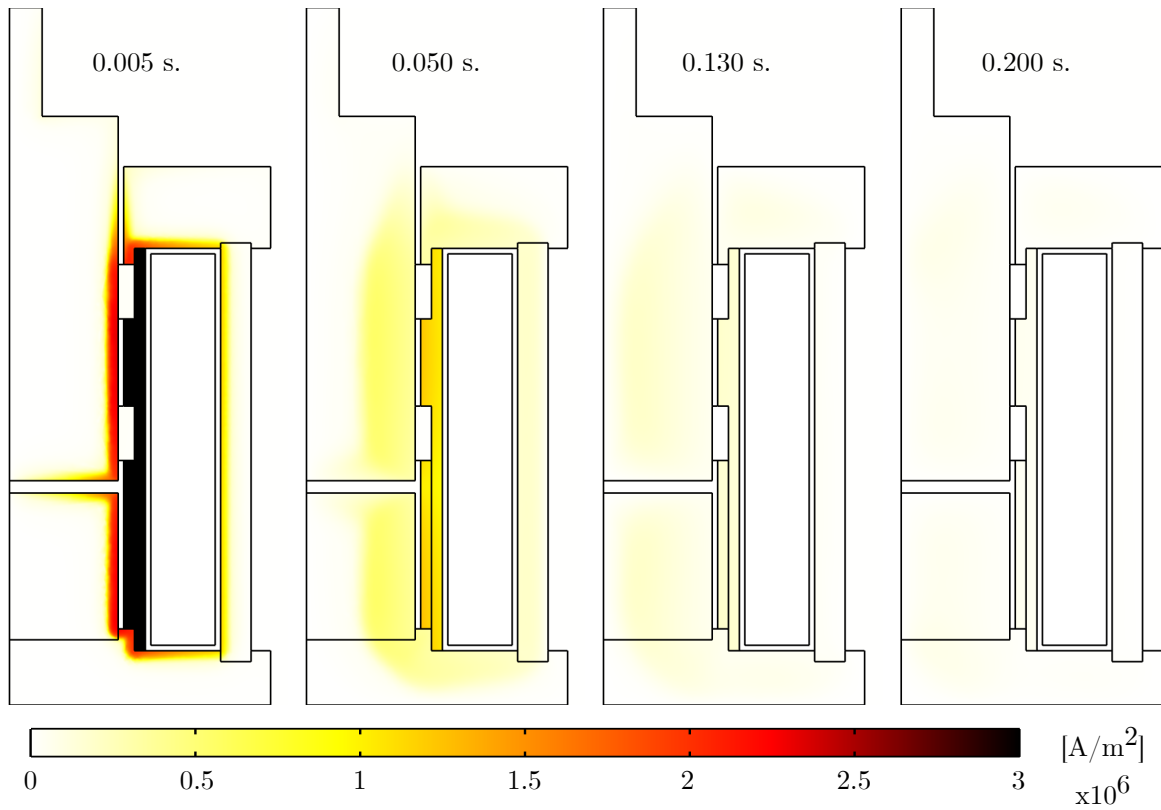


Figure 5.6. Transient development of the induced eddy currents.

5.3 Redesigning the aluminium center tubes

The problem with the aluminium center tubes is related to their relatively high electrical conductivity. This means that substantial currents are induced within these components during transient operation. A simple solution is to exchange the material of the two tubes. As an initial trial the aluminium material is replaced with a material with low electrical conductivity. A force response of a step input of 5 A can be seen in Figure 5.7.

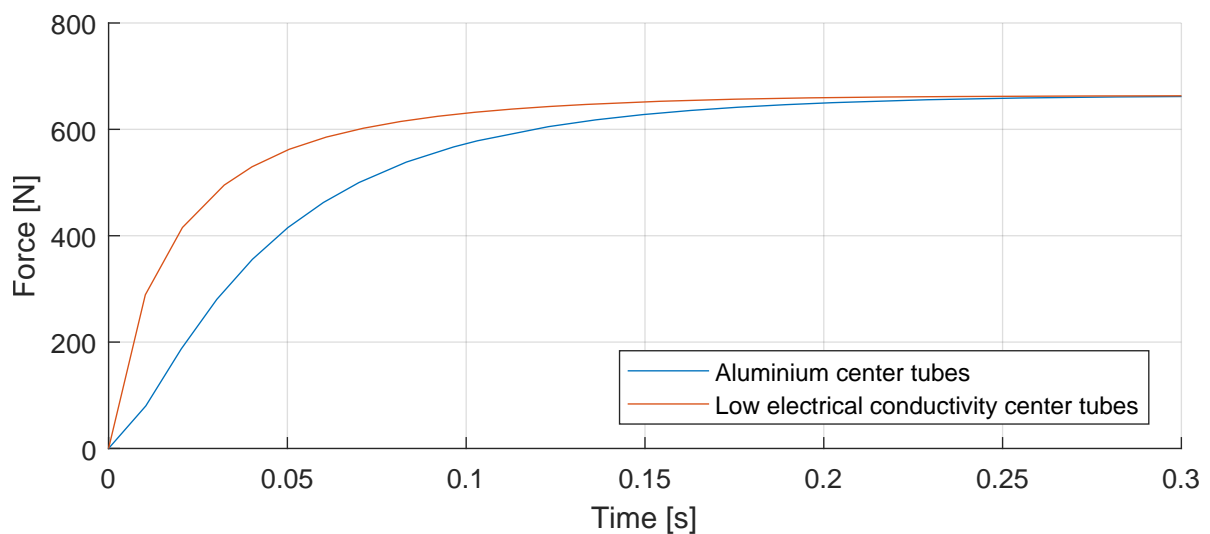


Figure 5.7. Force response with different center tube materials.

In the figure the response of the original design is also plotted for reference. In the response it can be seen that by changing the center tube material to a material with a low electrical conductivity, the speed of the magnetic system is increased. It is argued in section 5.2 that if the speed of the magnetic system increases, transient reluctance decreases. This means that the inductance likewise has been increased in the transient part of the response. It has to be taken into consideration that it might not be possible for the ESCON modules to drive the current to 5 A within an insignificant amount of time. Figure 5.2 shows the actual and simulated current in the actuator during the tests shown in Figure 5.1. Even though this would in reality slow the overall response, it is however seen that the magnetic system has increased in speed.

While it might be a viable solution to change the center tube material to one with a low electrical conductivity, there are two constraints which the new material has to fulfill.

1. It has to be tolerant to elevated temperatures. The solenoid is designed to be capable of operating at temperatures up till 100 °C (Steffensen, Sanderhoff, and Mejdahl 2021).
2. It has to be able to withstand the load exerted on the tube from both the copper windings and the end caps.

At the same time it requires the manufacturing of new parts, if another material is to be used. As the aluminium tubes are already manufactured and complies with the above, a modification to these would be preferable.

5.3.1 Cutting aluminium center component

In order to improve the design of the aluminium tubes, the idea of reducing eddy currents by breaking their path with the use of cuts is again utilised. In Figure 5.8 an illustration of a cross-sectional view of the solenoid is shown. This is a simple illustration of only the copper coil, aluminium tube and the steel plunger.

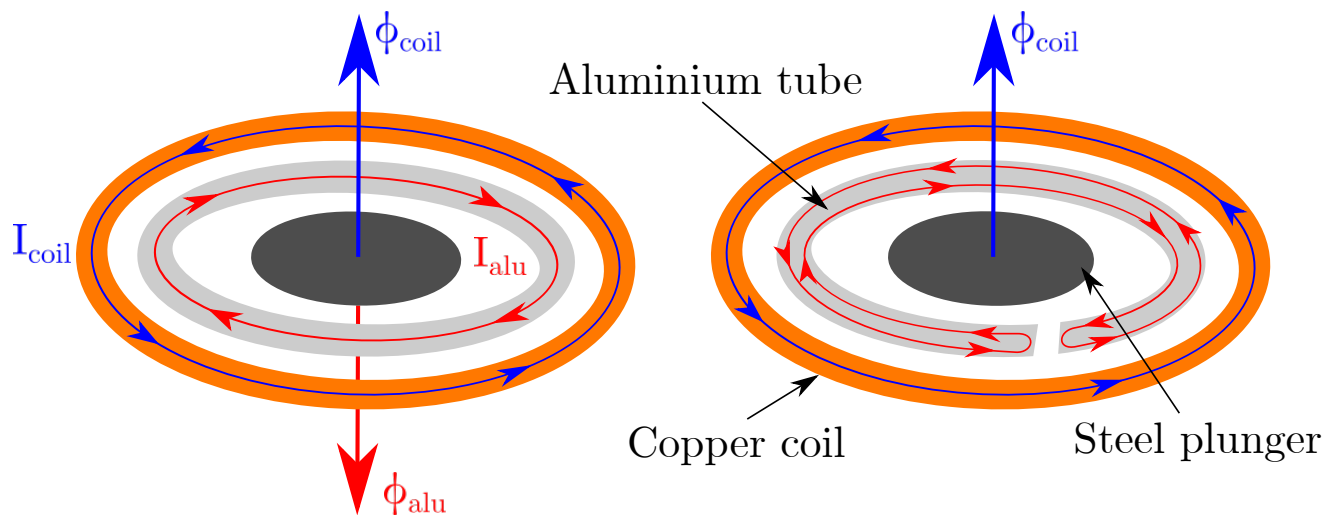


Figure 5.8. Illustration of currents and magnetic fields in cross-section of solenoid.

In the left hand part of Figure 5.8, the coil currents, I_{coil} , and associated magnetic field, ϕ_{coil} , is shown. Likewise the eddy currents induced by the magnetic field from the coil, I_{alu} are also shown, as well as the magnetic field created hereof, ϕ_{alu} . A simple solution to stop the currents in the aluminium tube is to make a cut in this part. As the currents have to run in a loop, the currents in the aluminium, which will still exist, instead runs in a loop as illustrated in the right hand part of the figure. To prevent short-circuiting through the top and bottom cap, these are electrically isolated from the aluminium tubes.

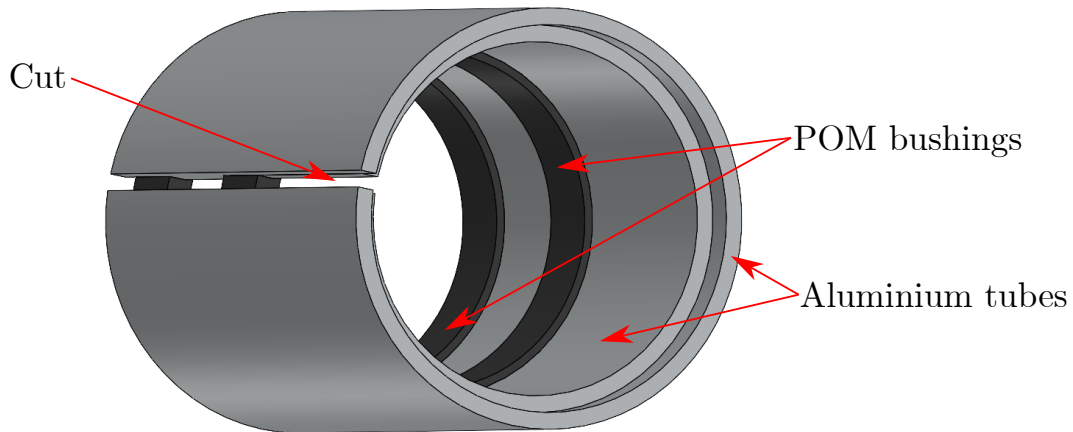


Figure 5.9. 3D model of aluminium tubes with cut.

Figure 5.8 is a simplified illustration of the behaviour, which is based on a 2D simulation of the problem. Simulating the problem in 3D shows, that eddy current loops are not as simple as illustrated here, however the intensity of the currents is still reduced.

Figure 5.9 shows the cut introduced in the aluminium tubes. In the 3D simulation, the desired behaviour is still achieved by cutting the aluminium tubes, as the eddy current loops are broken, and the opposing magnetic field has been removed. This also appears from the force response of the 3D simulation, where the response of the original solenoid design is compared to the improved design. This is shown in Figure 5.10.

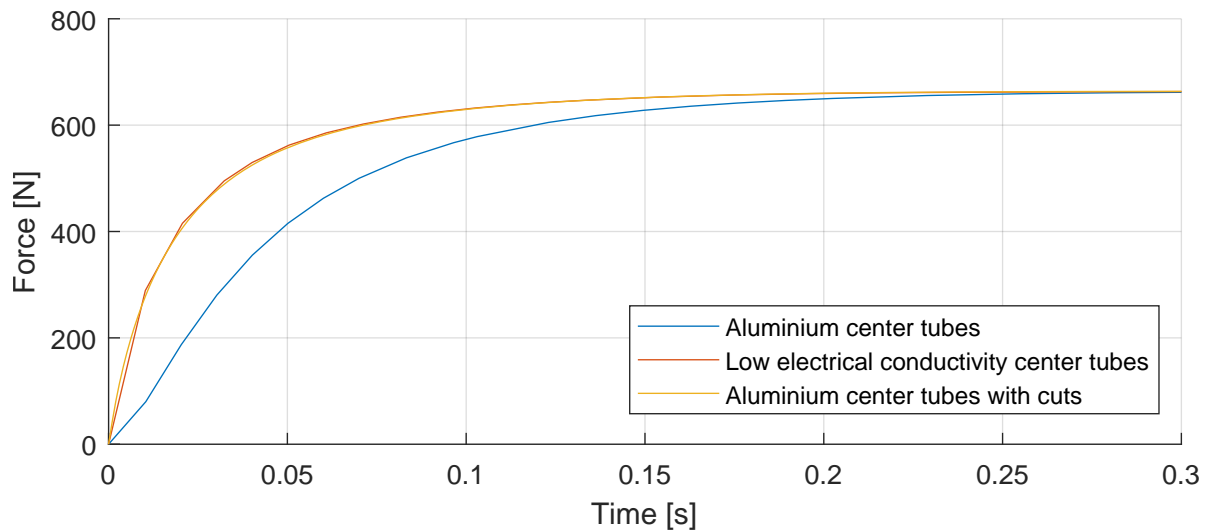


Figure 5.10. Force response from 3D simulation of original and improved solenoid.

From Figure 5.10, it appears to give similar performance whether the tubes are replaced with a low electrical conducting material or a cut is introduced in the aluminium tubes. This must be due to a reduction in eddy currents inside the aluminium tubes. The current density inside the cut tubes and the original tubes is shown in Figure 5.11.

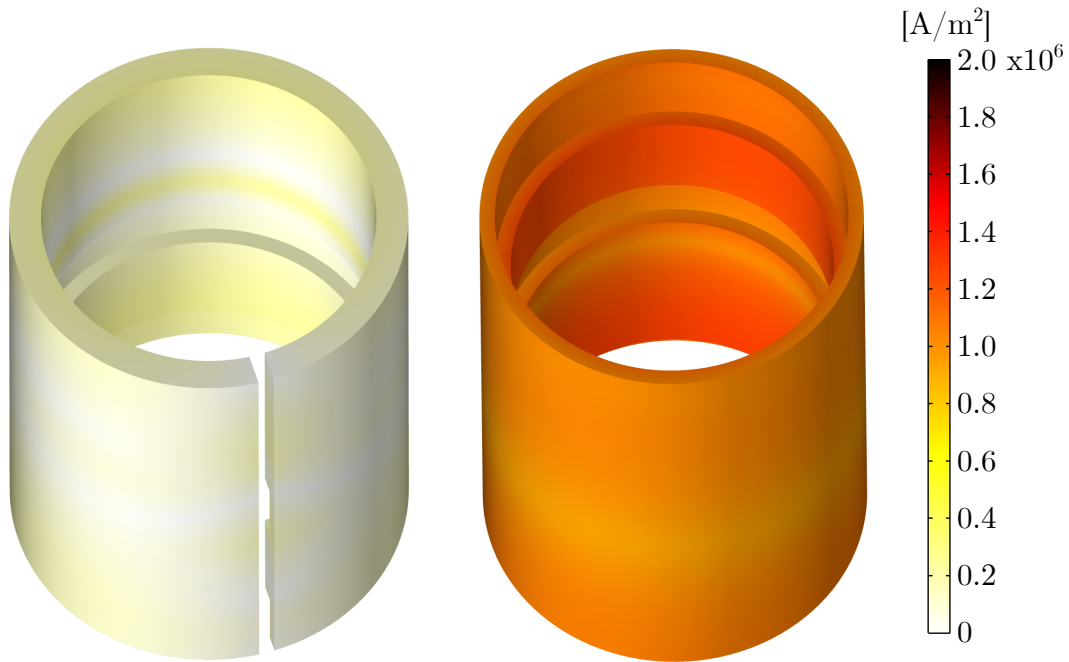


Figure 5.11. Contour plot of current density in improved and original design.

In the contour plots on Figure 5.11 it appears that the currents have been significantly reduced in the design with a cut in the aluminium tubes. While it has been reduced, currents are however still induced inside the aluminium. In Figure 5.12 the same plot of the current density contour is shown, however the color legend limits are adjusted. Here it is seen that the current density is concentrated in the marked areas. Three specific areas are marked on the figure, where it appears that the areas of highest concentration is mainly on the opposite site of the cut. The concentrations of current can be explained with Figure 5.13, which shows a contour line plot of the magnetic flux inside the non-steel parts.

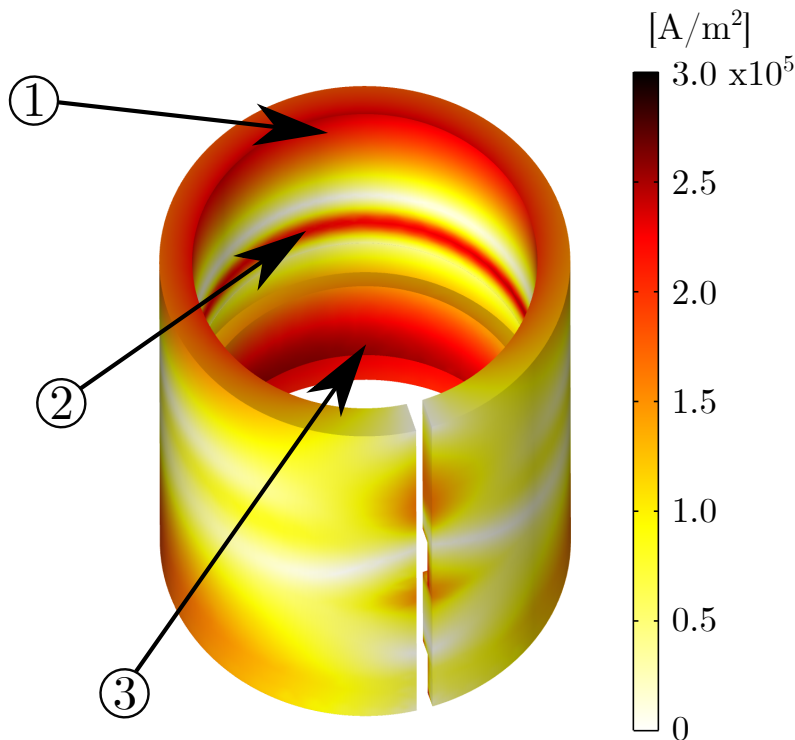


Figure 5.12. Contour plot of current density in cut aluminium tubes.

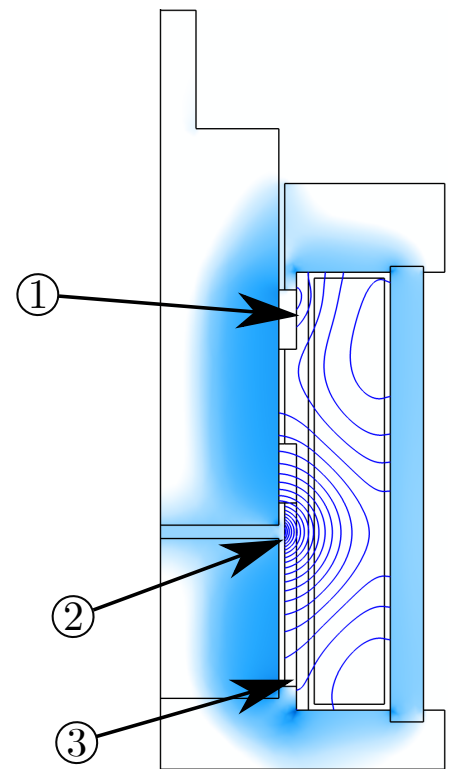


Figure 5.13. Leakage and fringing flux paths in solenoid.

In Figure 5.13 both leakage and fringing effects are observed. Here it appears that the current density in the aluminium tubes are at the highest at areas around the air gap and close to the top and bottom cap. This is also the areas at which the flux leaks through the non-steel parts of the solenoid as well as at the air gap where the fringing occurs. These current does not seem to slow down the build up of the main flux in the plunger, meaning the idea of cutting the aluminium tubes appears to yield satisfactory results. For this reason a prototype solenoid is manufactured with this improved design.

5.4 Test of improved solenoid prototype

With a prototype manufactured and assembled, it is possible to conduct tests to determine the improvement of the system speed. A sine sweep experiment as explained in section 3.1 is conducted to determine the frequency response of the system, and to compare the bandwidth of the improved system to the original. In Figure 5.14 the measured frequency response of the original and improved system is shown.

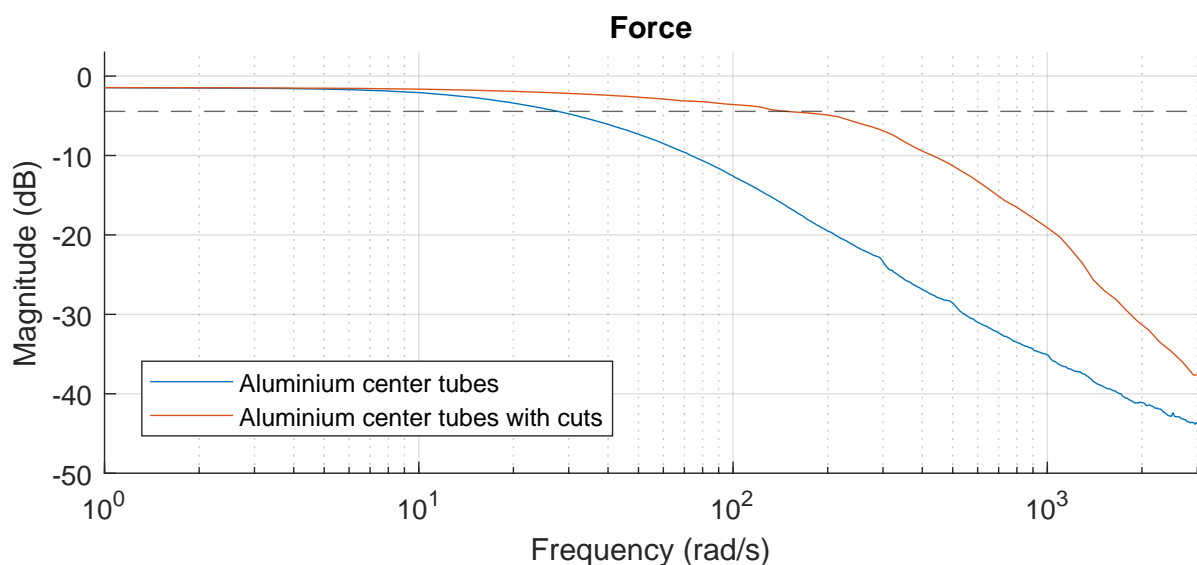


Figure 5.14. Measured frequency response of the force in the original and improved system. The dashed line marks the -3 dB drop off from the DC value of the responses.

The sine sweep experiments are conducted using the feed forward method, such that they are comparable. Both tests are conducted using the open loop approach, as described in section 3.1. In each experiment the peak to peak amplitude of the sine inputs are 550 N meaning the results gives an indication of the full scale capabilities of the system. The original system has a bandwidth of ≈ 5 Hz, while the improved system reaches ≈ 24 Hz, meaning the improved system is more than four times faster than the original.

As these experiments has been conducted on the real solenoid, it includes the dynamics of the full system including the electrical. To examine the influence of the electrical system, a frequency response from the current reference to the measured currents is plotted in Figure 5.15.

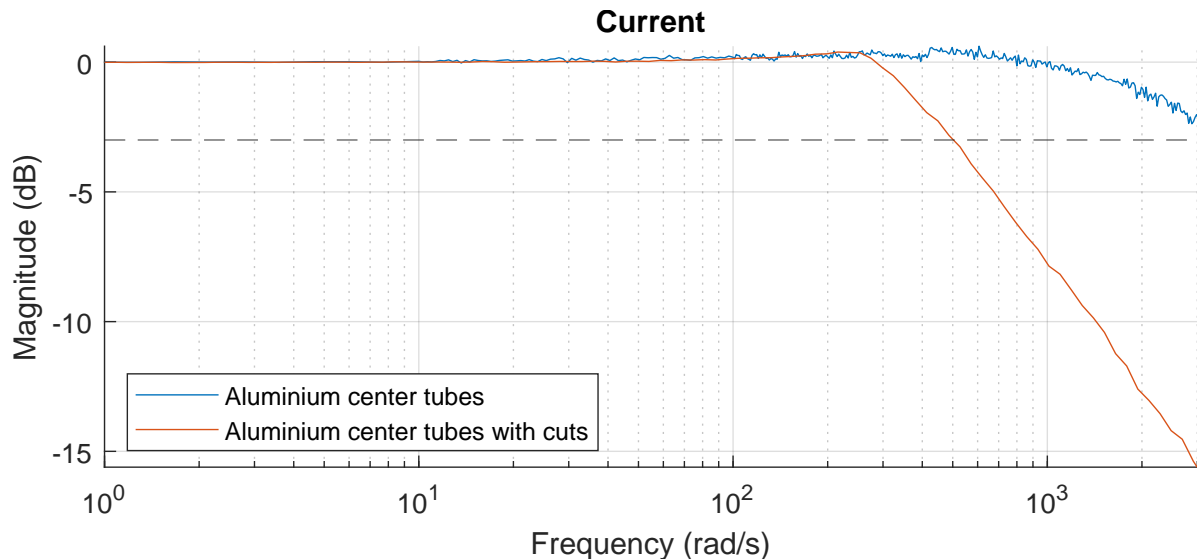


Figure 5.15. Measured frequency response of the currents in the original and improved system. The dashed line marks the -3 dB drop off from the DC value of the responses.

From the frequency response in Figure 5.15 it appears that the electrical system is affected by the change of the design. As described in section 5.2 the system is coupled, where it was argued that a decrease in eddy currents would effectively be a decrease of the transient reluctance value. This would increase the transient inductance value and slow the electrical system. This is exactly what is observed in the frequency response of the current. In the improved design, the bandwidth of the electrical system is ≈ 80 Hz, while the bandwidth of the original system is not even reached with these experiments. Here a 2 dB drop-off appears at 500 Hz. For both designs however, the electrical system is still significantly faster than the magnetic system.

5.5 Subsidiary conclusion

In this chapter an analysis of the solenoid geometry in regards to the transient behaviour is conducted. It is shown that significant eddy currents exist in the solenoid components of high electrical conductivity. While this includes both the steel and aluminium parts, this chapter is focused on the aluminium tubes. Here it is shown that by introducing a longitudinal cut into the two tubes, the pathway of the eddy currents can be altered to reduce the intensity of these currents as well as removing the opposing magnetic field. Despite a relatively easy and small change to the design, it is shown with both simulations and experiments, that the bandwidth of the force system is significantly increased. As it is shown in Figure 5.6 the eddy currents also exist within the steel parts of the solenoid. These are the focus of the following chapter.

Optimisation of cut pattern design 6

In this chapter an optimisation of the steel parts of the solenoid is conducted. The objective of the optimisation is to improve the transient performance of the solenoid, by decreasing the eddy currents. The optimisation is conducted with the aid of MATLAB and COMSOL, as these provide the necessary features and algorithms. To define the optimisation problem, the following must be considered.

- **Model:** The model refers to the virtual approximation of the solenoid structure, which includes considerations of meshing the structure. This virtual model is build in COMSOL.
- **Design variables:** The design variables define the degrees of freedom in the model for the optimisation. These degrees of freedom will be related to the geometry of the solenoid.
- **Cost function:** The cost function quantifies the different designs such that one design can be deemed better or worse than another design. The cost function will be dependent on settle time.
- **Constraints:** The constraints define the bounds of the design space. For the solenoid, the outer dimensions cannot be changed, meaning that geometric constraints exists for the problem.
- **Solver/Algorithm:** The solver/algorithm relates to the approach at which the optimisation problem is solved.

6.1 General optimisation approach

In chapter 5 the transient behaviour and characteristics of the solenoid is described. It is found that the unintended eddy currents is a main contributor for slowing the system. The eddy currents appear in all the steel components, however not with the same intensity. In Figure 6.1 the current density norm in the steel parts of the solenoid is shown. In Figure 6.2 the flux density and the flux pathways are plotted for the same time instance as the current density. The model is simulated with a current step input. In the current density plot it appears that the eddy currents in the remaining structure is primarily found in the plunger and center piece, while some currents are also present in the top and bottom cap. Relatively to the other steel components, the currents in the outer cylinder are small. In the flux density plot in Figure 6.2 it is seen that the eddy currents are blocking the flux from diffusing into the center of steel.

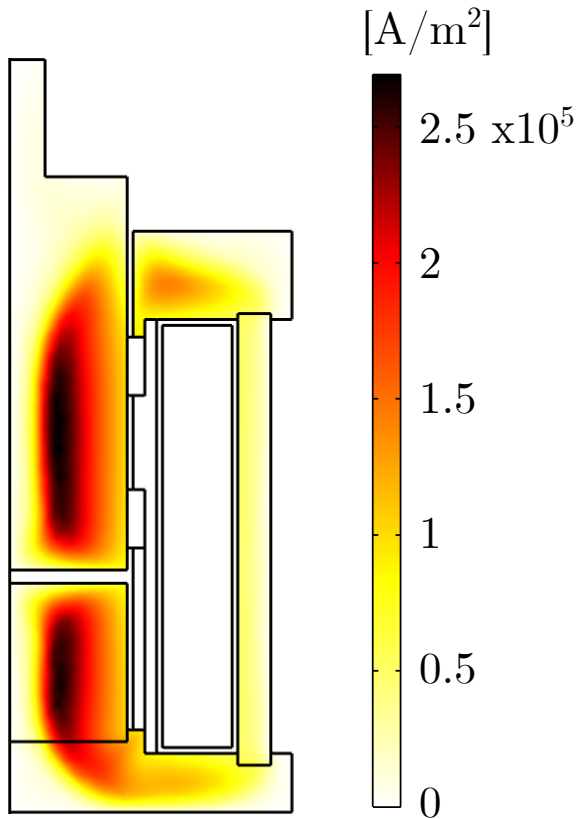


Figure 6.1. Current density of steel parts.

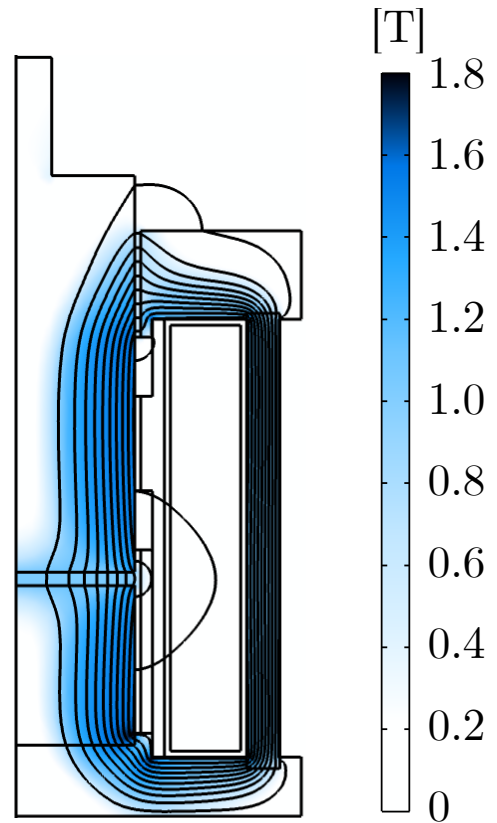


Figure 6.2. Flux density in solenoid.

As Figure 6.1 depicts the norm of the current density, the directions of the currents are not specified. However, the currents are induced in the plane normal to the direction of the magnetic flux. In the plunger, centerpiece and the outer cylinder, the direction of the currents can be deduced. An illustration of the plunger eddy currents is shown in Figure 6.3. As the direction of the magnetic flux is in the axial direction of the plunger, the induced currents run in the normal plane hereof, which is in the circumferential direction of the plunger seen in Figure 6.1. The induced eddy currents in the top and bottom cap cannot as easily be illustrated as the direction of the magnetic flux is different throughout the parts.

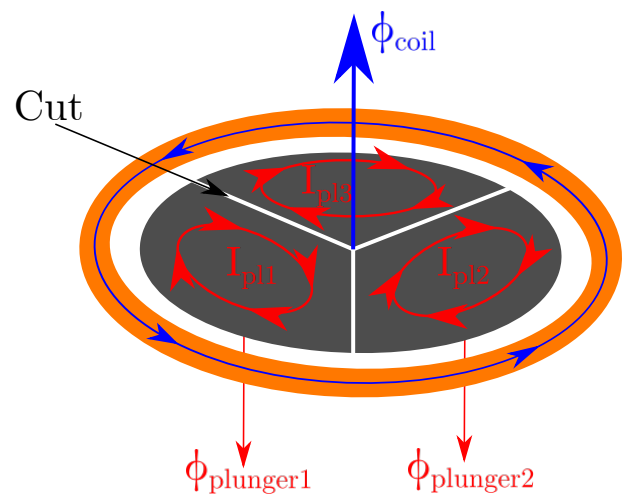
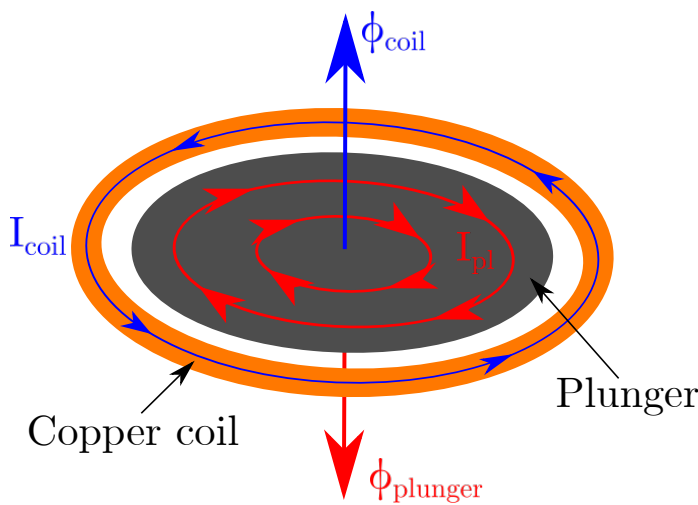


Figure 6.3. Currents and magnetic field in original system.

Figure 6.4. Currents and magnetic fields in system with cuts.

To limit the optimisation process, the problem is focused towards the plunger and center piece, as the eddy currents are found to be most significant in these parts. Prominent eddy currents are also induced in the top and bottom cap, however this is of less intensity than in the plunger and center piece. Due to the geometric similarity of the plunger and center piece, they can be treated equally. In the following, only the plunger is treated, as it is assessed that changes made in order to limit eddy currents in the plunger also applies to reduce eddy currents in the center piece.

In subsection 5.3.1 it is shown that the eddy currents can be successfully altered with a simple cut. The idea of making cuts in the plunger is also explored in Steffensen, Sanderhoff, and Mejdahl (2021), where it is found to improve the speed of the system. The effect of breaking the path of the eddy currents within the plunger is illustrated in Figure 6.4. As proven in Steffensen, Sanderhoff, and Mejdahl (ibid.), the cuts decrease the intensity of the currents, which leads to an overall improvement in speed in the magnetic system. This forms the basis for the following optimisation process, where an optimal cut pattern for the plunger is sought.

Since the cuts are to be in the longitudinal direction to interrupt the eddy currents, as shown in Figure 6.4, the solenoid actuator can no longer be represented by the 2D axisymmetric model. Instead either a 3D model or a non-axisymmetric 2D model is therefore required.

6.2 Modelling the solenoid

In the following section, the finite element model of the solenoid is presented. In the previous section it is argued that a 2D axisymmetric model is not viable. In 3D, the solenoid can be modelled with more details, and with such a model the actual rise time of the magnetic flux and force can be simulated. The model can give trustworthy estimates of the absolute differences between the rise time of the force for the different designs of the plunger, because it is verified against data from the solenoid test setup in chapter 5. The drawback to the 3D model is computational time. One of the challenges is simply to reduce the amount of elements used for meshing the model. In order to discretise the plunger when introducing cuts, a large amount of elements are needed to describe the air within the cuts. Each cut has a width of 0.3 mm, which is determined from the manufacturing capabilities. The COMSOL model of the plunger, as well as an example of the meshed model are shown in Figure 6.5 and 6.6.

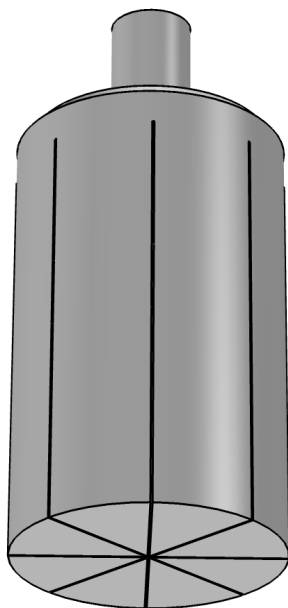


Figure 6.5. Plunger model in COMSOL.

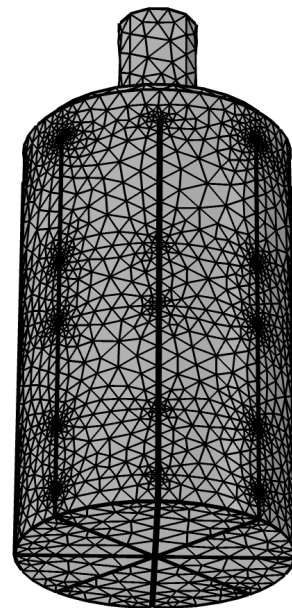


Figure 6.6. Meshed model of the plunger.

In Figure 6.6 the horizontal lines in the mid part of the plunger defines the boundaries for the contact face of the POM bushings.

In order to make the 3D model suitable for the optimisation process, the computational time has to be significantly reduced. While it is deemed possible to reduce the time to solve the model, it is assessed to be unrealistic to reduce it to a degree at which it is useful for the optimisation. This means another approach has to be taken.

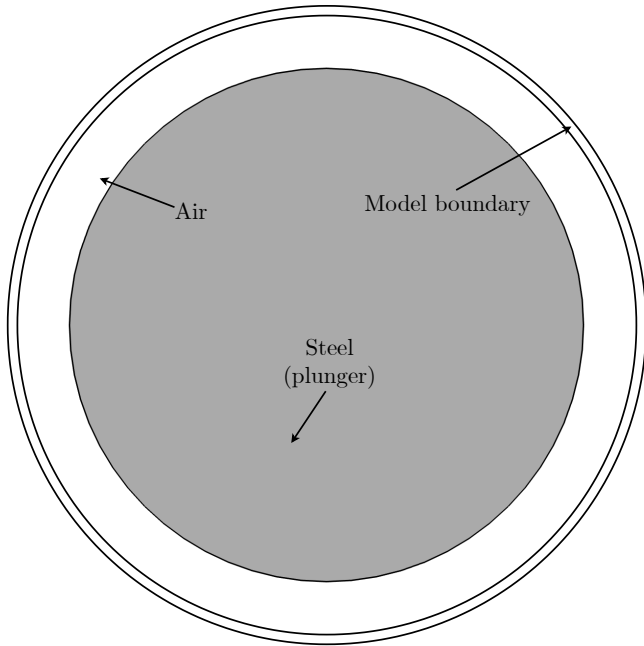


Figure 6.7. 2D model of solid plunger.

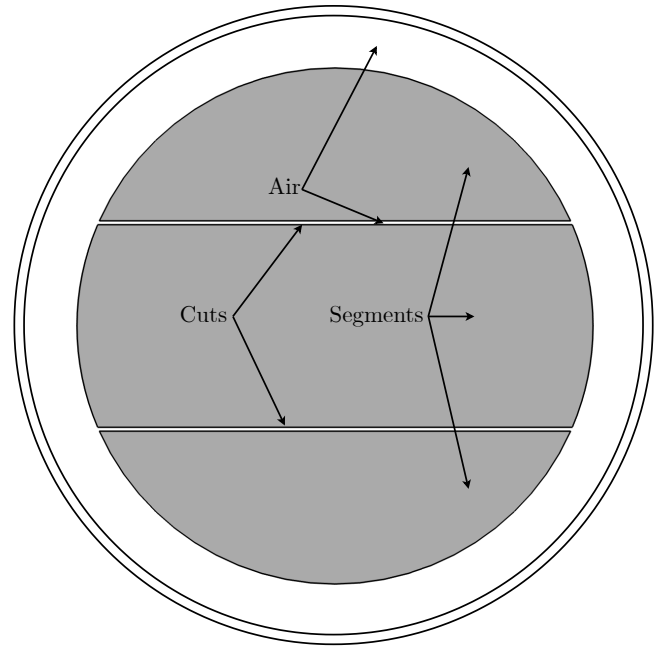


Figure 6.8. 2D model of plunger with cuts.

To reduce the computational time, a 2D model, as shown in Figure 6.7 and 6.8, is proposed. Most of the details in the solenoid actuator cannot be included in such a model, however the main benefit is the possibility to model the cuts with a much lower number of elements. Using such a 2D model, it is not possible to explicitly calculate the resulting force. Instead the build up of magnetic flux density will be examined, as the force is related to it, as shown in Equation 1.1 on page 4. By excluding the majority of the solenoid details, this 2D model will not be able to produce results for the actual settling time of the magnetic flux density in the plunger. If the relative order between cut designs, in terms of the time to build up magnetic flux density, can be accurately determined with this model, it is deemed useable for the optimisation. Since the main goal is to optimise the settling time of the flux in the plunger, only this part needs to be modelled. As the remaining parts are unchanged, they are assumed to not affect the results.

In the 2D model, it is not possible to use the available coil feature in COSMOL to apply circumferential currents in the plane. It is assumed that the complete system is the fastest, when the magnetic system is as fast as possible, even though the speed of the electrical system becomes slower when the eddy currents are reduced, as described in Equation 5.4. The characteristic of the electrical system is therefore not of importance, since the fastest overall system can be determined solely from the speed of the magnetic system. Applying a constant current in the coil at time zero induces a magnetic field originating from the coil. With respect to the 2D model this is equivalent to inducing a magnetic field, H , on the model boundary seen in Figure 6.7 with a specified field intensity in the out-of-plane direction.

6.2.1 Comparison of 2D and 3D model

To compare the results of the 2D and 3D model, five different cut designs are chosen. The pattern and name of each design is shown in Figure 6.9. Each pattern consists of four cuts.

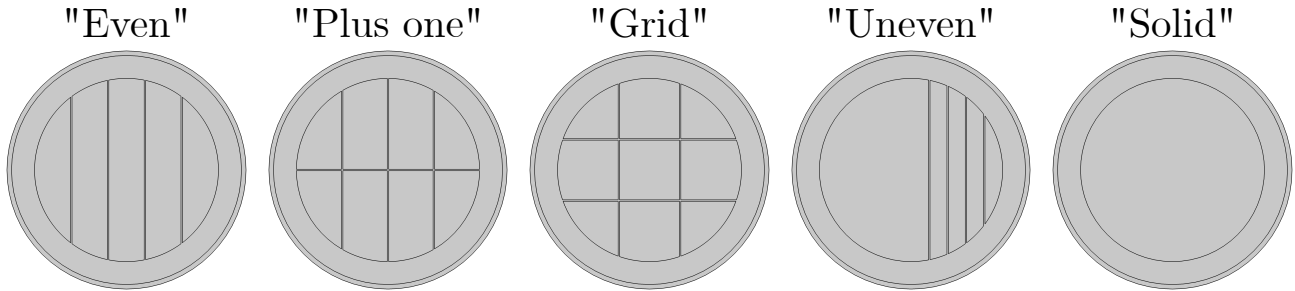


Figure 6.9. Cut pattern designs used for example.

Each of the five patterns are modelled in both 2D and 3D. In the 3D model the cut pattern is made in both the plunger and the center piece. For comparing the results, the build up of flux in the plunger is calculated. In the 3D model the build up of flux is calculated in "Plane 2" shown in Figure 6.13. In the 2D model the DC flux value reached depends on the the applied magnetic field. The value for the magnetic field intensity is approximated from the 3D model here, however a review of the value used for the optimisation is presented further below. As the DC level reached in the 2D and 3D model is not the same, the flux response is normalised with respect to the DC value in each simulation. The results are shown in Figure 6.10 and 6.11.

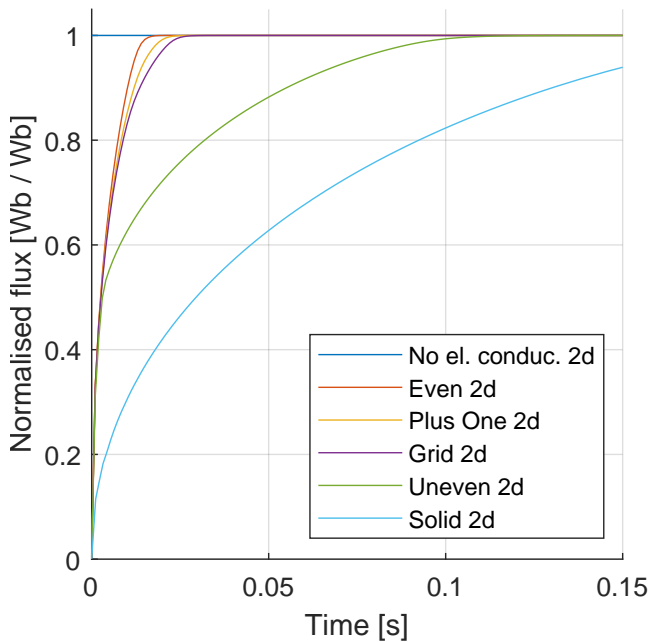


Figure 6.10. Comparison of flux responses in 2D.

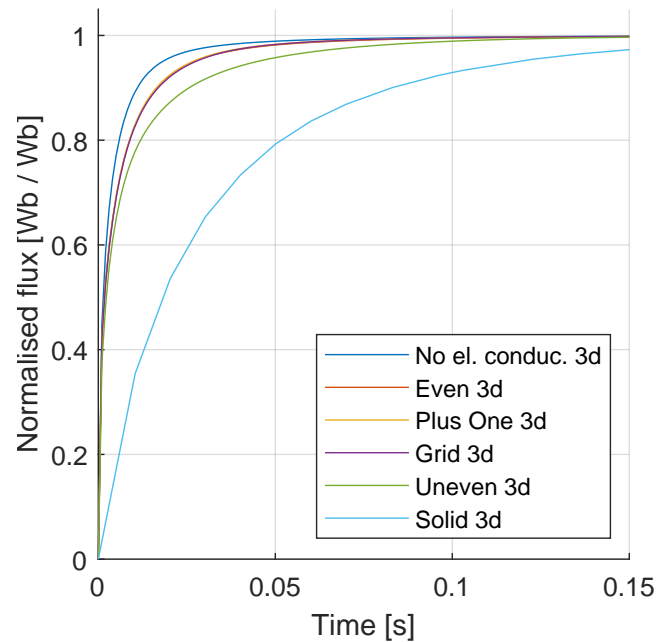


Figure 6.11. Comparison of flux responses in 3D.

In the results it appears that the order of which designs settle the fastest is maintained for most of the designs in the 2D and 3D simulations. The order should be maintained for the 2D model to be valid and usable, which is not directly the case in the above results. However, the results for the 3D simulations in Figure 6.11 are assumed to be affected by something else than the different cut pattern designs. While it is seen in both the 2D and 3D model, that introducing cuts decreases the settling time of the flux in the plunger, it seems that the "Even", "Plus one" and "Grid" designs have the same settling time in the 3D simulations. As a measure for comparing each of the responses, the cost function, which is to be used for the optimisation, is utilised. The cost function is presented in section 6.4. In short terms, the cost

function value is a measure for speed of the designs. Here a lower value indicates a design with a lower settling time. The cost function values of each example design is presented in Table 6.1.

	No el. conduc	Even	Plus One	Grid	Uneven	Solid
Cost function value (2D)	-0.4000	-0.3960	-0.3955	-0.3950	-0.3836	-0.3514
Cost function value (3D)	-0.3951	-0.3933	-0.3934	-0.3933	-0.3903	-0.3666

Table 6.1. Cost function values for the different designs in 2D and 3D.

In the table it is seen that the order is partially maintained, however the "Even", "Plus one" and "Grid" designs achieve a cost function value which is almost the same. In the real solenoid and the 3D simulations, it is not only the plunger and center piece which are slowing the system. In all steel parts, eddy currents are induced, as seen in Figure 6.1, meaning that all these parts are slowing the build up of magnetic field. As the other steel parts are included in the 3D model, their dynamics are also included in the response in Figure 6.11, which is not the case for the 2D model. As an indication for this, two additional simulation results are shown in Figure 6.10 and 6.11, one for each. In these simulations the electrical conductivity of the plunger (and center piece for the 3D model) is set to zero. This is equivalent to a "perfect" cut design, which effectively removes all eddy currents. These are denoted: "No el. conduc." in the figures. In the 2D model, this effectively removes all dynamics, meaning the flux settles instantly. For the 3D model the settle time only slightly decrease, when the eddy currents are effectively removed from the plunger and center piece. Any remaining dynamics, which are still present in the response, must be due to the other steel parts. As the flux must build up in all steel parts simultaneously, the settle time is decreased to a level at which it is no longer dominated by the dynamics of eddy currents in the plunger and center piece.

In relation to how the 2D model behaves compared to the 3D model, the results shown in Figure 6.10 are assumed to still be valid, however they only apply exclusively for the plunger and center piece. While the system appears to be dominated by other dynamics, it is shown in the results in Figure 6.11 that there is still a possibility to slightly decrease the settling time. This is seen with the "No el. conduc. 3d" response, as this is still slightly faster than the other responses. However it will most likely require more than four cuts to achieve a better result.

Review of B-field in the plunger

The above forms the basis of the argumentation that the 2D model is sufficient to use for optimising the settling time of the flux in the plunger and center piece exclusively. However, the analysis is based on a low number of different example designs, while the optimisation is not to be limited from any patterns. It is difficult to generalise the results based on these example designs alone. Therefore a brief review of the B-field distribution in the plunger is presented to substantiate the use of the 2D model. This analysis takes offset in a "pizza" cut pattern. In Figure 6.12 the plunger B-field distribution for the 2D model during transients is shown.

In Figure 6.12 it appears that the flux density builds up from the edges of each segment and into the middle. This behaviour should also appear from the 3D model, if the two models are modelling the same system characteristics. To analyse this the flux density distribution in the 3D model of the solenoid is shown in Figure 6.13.

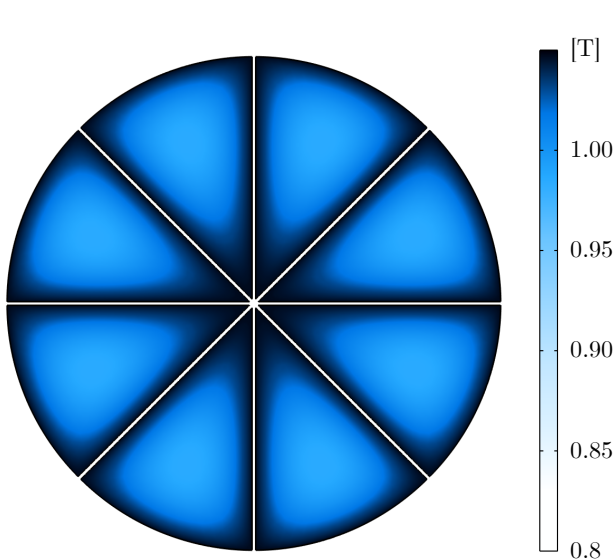


Figure 6.12. B-field plot in the 2D model.

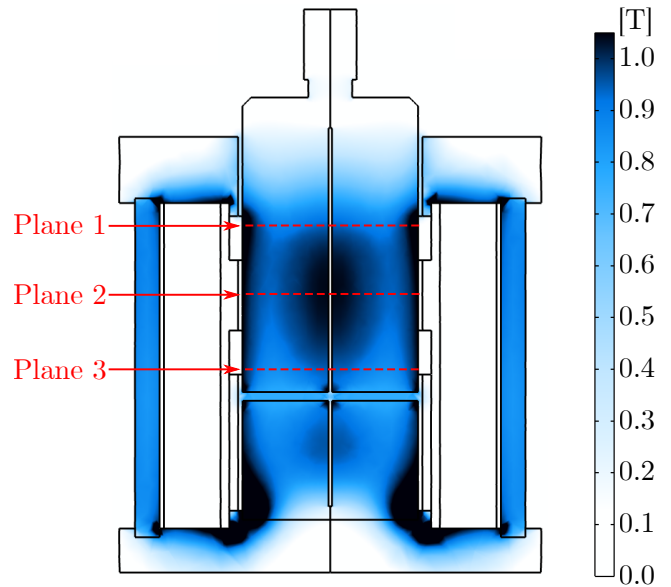


Figure 6.13. Flux density in cut-section of 3D model.

The plot is showing the B-field during the transient part of the response. In the figure, three planes are defined at three distinct locations in the plunger. The three planes are defined at locations where the B-field is slightly different from each other. The flux density distribution in the plunger in each plane is shown in Figure 6.14, 6.15 and 6.16.

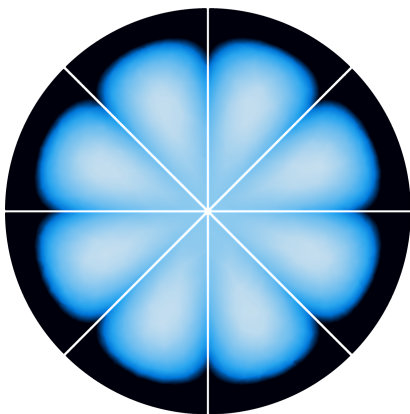


Figure 6.14. B-field plane 1.

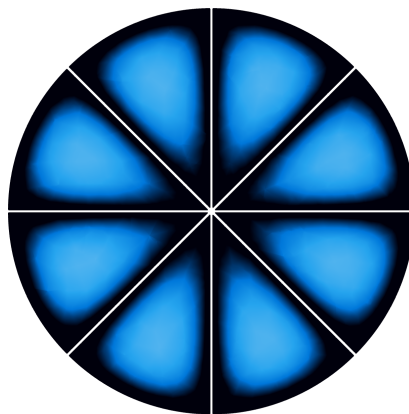


Figure 6.15. B-field plane 2.

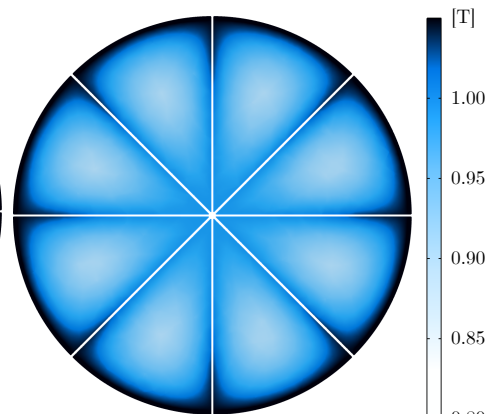


Figure 6.16. B-field plane 3.

The distribution of the B-field in each plane is quite different. The distribution in plane 1 and 3 appears similar due to the concentration on the outer edges of the plunger segments. They are however different in intensity. The distribution in plane 2 appears to be very similar to the distribution seen with the 2D model in Figure 6.12. The distribution of the B-field in the plunger appears to be quite different depending on the location of the plane. From Figure 6.13 it is expected that the distribution seen in plane 2 is also seen in any arbitrary plane in between plane 1 and 3. These two planes mark the location of transitions, where the distribution is slightly different. This however means that a majority of the plunger has a distribution similar to plane 2, and therefore the 2D model. The 2D model is therefore assumed to be sufficiently accurate in modelling the distribution of the B-field in most of the plunger.

Analysis of H-field intensity in 2D model

The 2D model appears to be a satisfactory model of the magnetic field in the plunger. While the above analysis of the 2D model behaviour is done with an estimated intensity of the H-field corresponding to the one observed in the 3D model, this is not exact. As a value has to be set for the 2D model, the impact of using different field intensities is analysed. In Figure 6.17 the response of three plungers with different cut designs and with three different H-fields applied, is shown. The three designs are similar to the "Even", "Plus one" and "Grid" cut patterns used in the above, respectively. The response shows the rise in the magnetic flux in the steel over time. Each response is normalised with respect to its respective DC value.

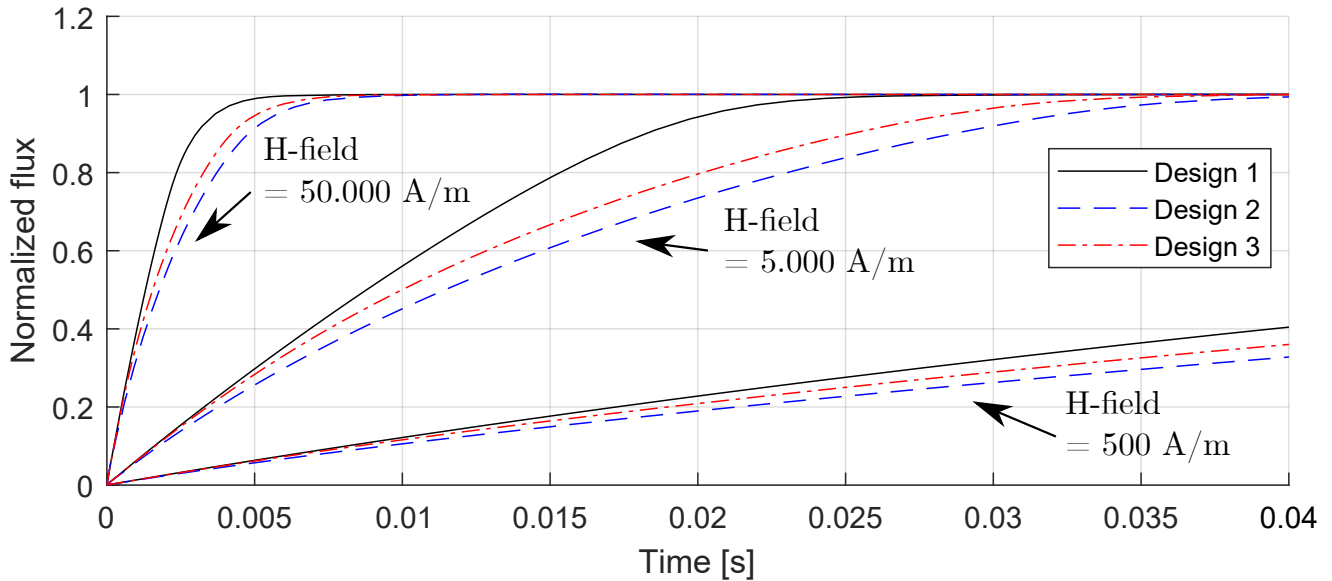


Figure 6.17. Comparison of different values used for the H-field.

Two important observations are done from Figure 6.17. Firstly, the rise time of the magnetic flux is for all three designs faster with higher field intensity. This is to be expected as the designs reaches magnetic saturation earlier. Secondly, design 1 appears to have the fastest rise time, then design 3 and then design 2. This order is the same no matter the intensity of the H-field, which is advantageous as it indicates that in terms of the optimisation, the relative speed between the designs seems to be maintained independently of the H-field. For the optimisation a field intensity of 5000 A/m is chosen. According to Figure 4.4 on page 21, which depicts the BH-curve, the steel is experiencing saturation at 5000 A/m. The solenoid actuator will reach magnetic saturation during operation, so to ensure that this is also a part of the optimisation, the intensity of the field is chosen such that saturation also occurs in the model.

6.2.2 Meshing

Due to the nature of the problem, where the cut pattern in the plunger is fundamentally different between designs, the mesh generation has to be automated. It is difficult to set up any general definitions of the mesh inside the plunger, as no patterns are restricted. To perform the optimisation, COMSOL's automatic mesh generation feature is utilised. This is a physics based meshing feature, which sets appropriate settings for the given physics (COMSOL 2019). The user is able to control the general refinement level of the mesh in nine different levels from coarser to finer. Using the auto-generated mesh, the model might not be as time efficient as possible, however it can easily and quickly be applied to an arbitrary geometry.

6.2.3 Convergence study

To analyse the mesh generation, a convergence study is conducted. As the problem includes a high amount of arbitrary geometries, it is difficult to generalise this study. However, five selected geometries are created to do an initial examination of the performance. These geometries are seen in Figure 6.18. A model without cuts is included for reference.

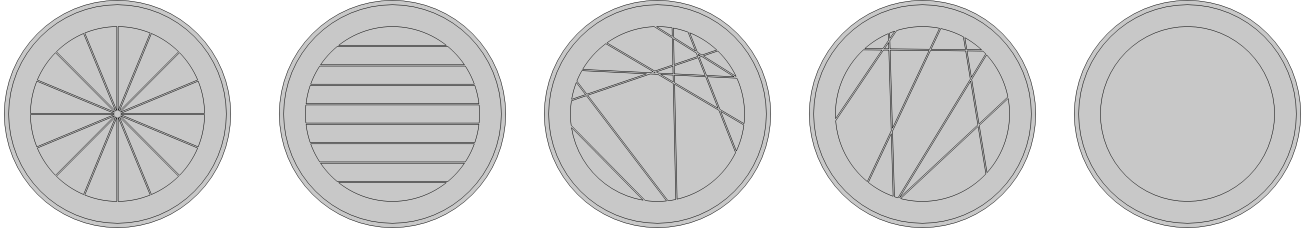


Figure 6.18. The five reference cut designs for the mesh convergence study.

The convergence study is conducted by evaluating the cost function value for each of the five designs using the nine different mesh refinement levels. The cost function is presented in Equation 6.4 on page 48. To be able to compare the the different mesh levels and the different patterns at the same time, the cost function values of the five designs are normalised with the cost function value of the finest mesh setting for each design. This is done as it assumed that the result is converged to a satisfactory degree at this setting. This means that at the finest setting, each design is given a value of 1. To see the deviation from this value, all the results are subtracted by 1, and converted to per mill. The results are shown in Table 6.2.

	Mesh level (coarser → finer)								
	1	2	3	4	5	6	7	8	9
"Pizza" pattern	0.14	0.07	-1.10	-0.48	-0.14	-0.47	0.04	0.09	0
"Parallel" pattern	-0.02	-0.91	-1.16	-0.12	0.09	-1.04	-1.00	0.14	0
Random pattern 1	0.37	0.30	0.26	-0.06	0.24	-0.06	0.36	0.14	0
Random pattern 2	0.19	0.09	-0.01	0.15	-0.02	0.14	-0.36	-0.02	0
No cuts	0.33	0.69	0.21	-0.06	-0.02	0.15	-0.16	0.10	0

Table 6.2. Deviation from finest mesh setting for each pattern in %.

From the results it can be concluded that for the five trial designs, the deviation in the cost function is negligible. Here the maximum deviations are in the order of 1.2 %. The deviation is in fact so small that it is assumed to be due to numerical uncertainty in the FE solver. In practice, the result seems to be independent of the mesh refinement level. To further analyse this, three meshed examples of the fourth cut design are shown in Figure 6.19 to 6.21

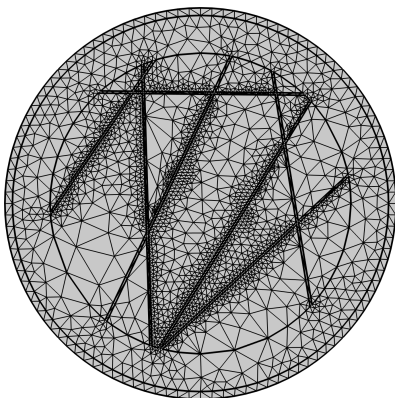


Figure 6.19. Coarsest mesh.

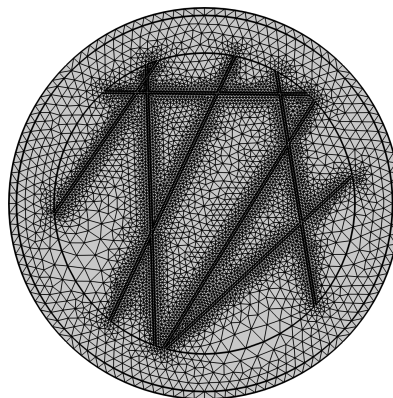


Figure 6.20. Intermediate mesh.

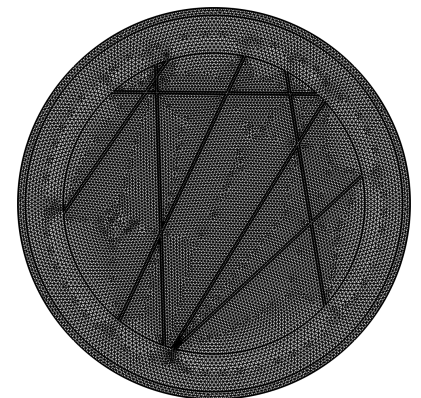


Figure 6.21. Finest mesh.

For the first two meshes, the majority of the elements are placed inside the cuts. Even with the coarsest mesh setting, quite a lot of elements are used inside the cuts. For the finest mesh setting, the element sizes are more or less constant. The meshed model consists of approximately 4800, 10600, and 25000 elements, respectively. The solution time of the the models are 19 s, 54 s and 144 s, respectively. Despite the coarsest mesh setting yielding the approximately same result for the cost function value, mesh level five is used for the optimisation procedure. The lower mesh levels generally is producing elements which are of low quality according to a condition number measure used in COMSOL, which is often caused by highly skewed elements inside the cuts. Despite the good results from this mesh levels, it is difficult to predict whether similar satisfactory results are obtained for an arbitrary design. With a mesh level of five, the mesh appears to be of good quality, at least for the five designs.

In this section it is shown that a simplified 2D model of the plunger is usable for the optimisation. The absolute values are not correct with this 2D model, meaning only the relative improvement by introducing cuts is of interest.

6.3 Design variables and design space

The optimisation problem is regarding the cuts made in the plunger, meaning that the design variables of the problem is related to the position of the cuts. Each cut is defined with an angle, θ_k , and a length, l_k . This means that two degrees of freedom are associated with each cut. This yields the following design vector, \mathbf{x} :

$$\mathbf{x} = [\theta_1 \quad l_1 \quad \theta_2 \quad l_2 \quad \dots \quad \theta_n \quad l_n]^T \quad (6.1)$$

Where n denotes the number of cuts. The definition of the degrees of freedom for a cut are shown in Figure 6.22. The length l_k is defined as the shortest distance between the center of the plunger and the cut, while the angle θ_k is the angle of the cut from the horizontal line.

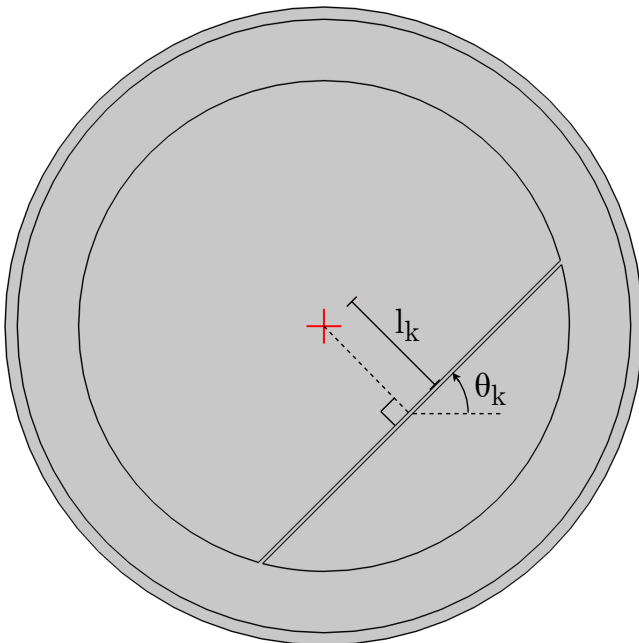


Figure 6.22. Definition of the degrees of freedom.

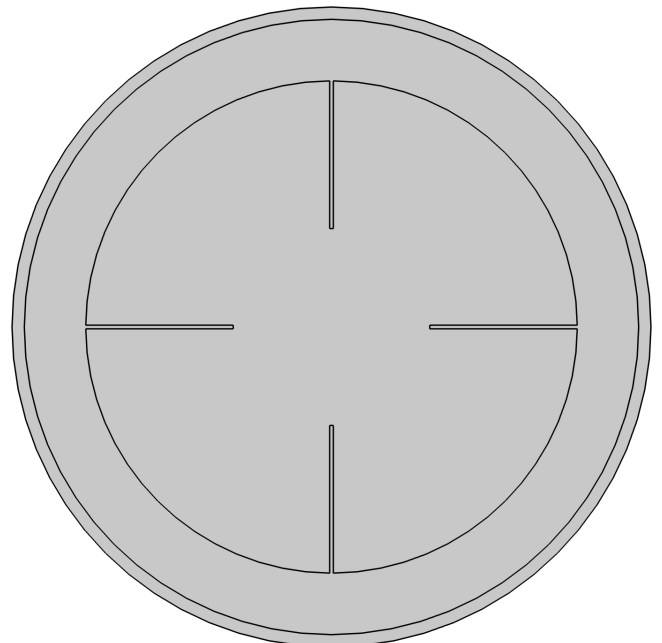


Figure 6.23. Non feasible pattern.

The width of the cuts is predetermined by the chosen manufacturing process. Electrical discharge machining (EDM) is chosen, as this allow for thin cuts of down to 0.3 mm. As it is required to maintain the structural integrity of the plunger, all cuts are made from the bottom of the plunger towards the top, as shown in Figure 6.24. The cuts will stop at the height of the non working air gap. Since the

EDM process is used, partial cuts, like the ones in Figure 6.23, cannot be made. This removes degrees of freedom for each cut, as three degrees of freedom are necessary to fully define an arbitrary cut with a predefined length. If the length is not predefined, four degrees of freedom would be needed.

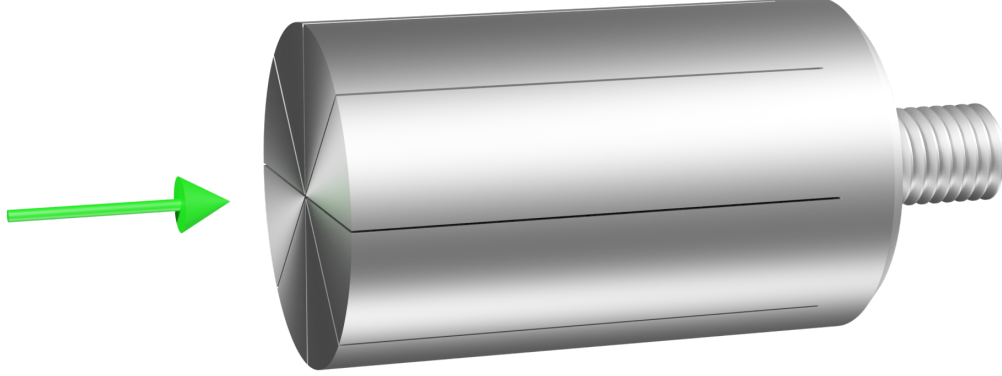


Figure 6.24. EDM cut direction in the plunger.

6.4 Cost function for optimisation problem

In order to quantify and compare the performance of the different pattern designs, a cost function is to be developed. The essential focus for this problem is the settling time of a given design. The faster the magnetic field can built up, the faster the force system will be. The force of the solenoid cannot be explicitly determined with the 2D model, which means that the cost function is instead related to the magnetic flux in plunger. It is found that the most reliable measure related to the settling time is to integrate a function describing the flux build up. Using the settling time directly is found to be more sensitive to mesh quality and the solver settings within COMSOL. The cost function, f , of a given design described by the design vector, \mathbf{x} , is the following:

$$\min_{f(\mathbf{x})} f(\mathbf{x}) = - \int_0^{t_{end}} \frac{\phi(\mathbf{x}, t)}{\phi(\mathbf{x}, t_{end})} dt \quad (6.2)$$

Where t is the time and the constant t_{end} is the end time of the simulation, determined as the settle time of the plunger without cuts. The integration is performed numerically within MATLAB. The function $\phi(\mathbf{x}, t)$ describes the flux in the plunger at a given time. The flux is determined by integrating the flux density over the plunger area:

$$\phi(\mathbf{x}, t) = \sum_{i=1}^n \left(\int B_n(\mathbf{x}, t) dA_n \right) \quad (6.3)$$

Where B_n and A_n is the flux density field and area of a given segment denoted n , respectively. A segment is defined as a part of the plunger as shown in Figure 6.8 on page 41. The integration of the flux density is handled within COMSOL. The denominator of the fraction in Equation 6.2 serves to normalise the flux function with respect to the DC flux level. The normalisation of the flux function has an impact on the results of the optimisation procedure. Including the normalisation removes the effect and impact of the difference between the achieved DC levels in the different designs. To examine this, two cut design examples are used, called $\mathbf{x1}$ and $\mathbf{x2}$. These are showed in Figure 6.25 and Figure 6.26.

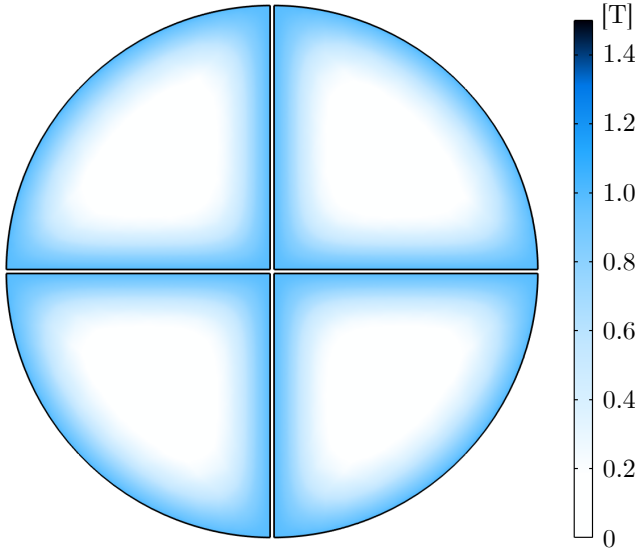


Figure 6.25. Flux density in cut design $\mathbf{x1}$ at 0.05 s.

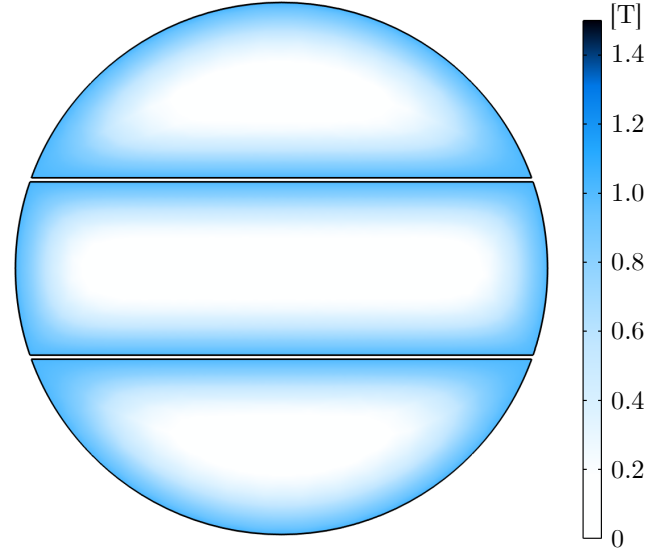


Figure 6.26. Flux density in cut design $\mathbf{x2}$ at 0.05 s.

Plotting the flux function defined in Equation 6.3 for the two designs, as well as the flux function for a plunger with no cuts for reference. In Figure 6.27 it appears that the designs with two cuts have a lower settling time, however the design with the solid plunger reaches a slightly higher DC level. This is due to the fact that material is removed in designs including cuts. Comparing the two designs with cuts, only a slight difference in the DC flux level for the two designs are present:

$$\frac{\phi(\mathbf{x1}, t_{end})}{\phi(\mathbf{x2}, t_{end})} = 99.9\% \quad (6.4)$$

Where $\mathbf{x1}$ is design 1, and $\mathbf{x2}$ is design 2. Comparing the area of the two designs in Equation 6.5, shows the same difference, as the difference seen in Equation 6.4.

$$\frac{A_{\mathbf{x1}}}{A_{\mathbf{x2}}} = 99.9\% \quad (6.5)$$

Regarding the normalisation term in the cost function, the cost function value of the two designs are calculated and compared:

$$\frac{f(\mathbf{x1})}{f(\mathbf{x2})} = 100.03\% \quad (6.6)$$

Design 2, which has a bigger area and DC flux level, has the lowest function value and is therefore the best design. However, by calculating the cost function values again but this time without using the normalisation term in the cost function yields:

$$\frac{f_{mod}(\mathbf{x1})}{f_{mod}(\mathbf{x2})} = 99.93\% \quad (6.7)$$

Where f_{mod} is the cost function with no normalisation term. Using the modified cost function, the first design has the lowest cost function value and is therefore found to be the best. While the difference in the cost function values between the two designs are close to being equal with both cost functions, it is

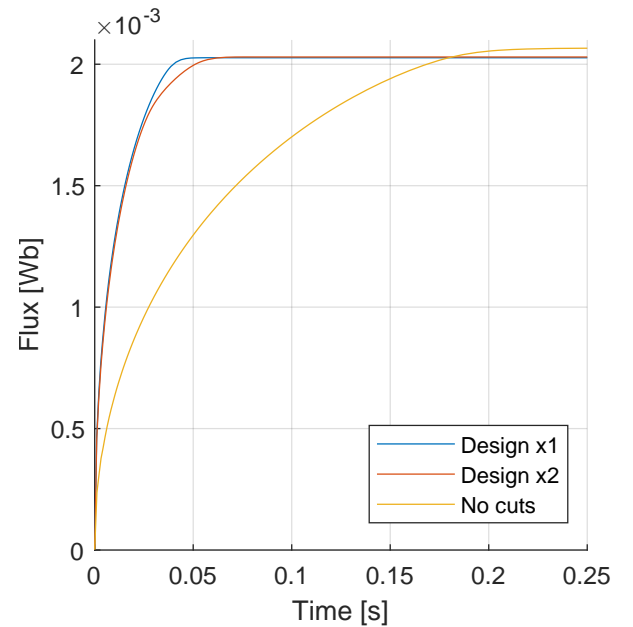


Figure 6.27. Step response of Equation 6.3 for design $\mathbf{x1}$ and $\mathbf{x2}$.

quite significant that the best design is switching, when using the other cost function. By omitting the normalisation term, the loss of area is penalised, which explains why the lowest function value is achieved with design 2 in Equation 6.6, as this has the least loss of area. If the flux is integrated over a long period of time, the design with the highest DC will always achieve the best cost function value. The force of the plunger is dependent on the area according to Equation 1.1.

$$F = \frac{B^2 A}{2\mu_0\mu_{air}} \quad (1.1)$$

One could argue that a penalisation on the loss of area is reasonable, as a loss would result in a reduced force. However, since the solenoid has shown to be able to deliver more than enough force in regards to the specifications, some loss in peak DC force is permissible. Instead the design that reaches its DC level the fastest is preferred, which is achieved by using a normalisation term in the cost function.

6.5 Constraints

In order to limit the design space, constraints and bounds have to be applied for the design variables. Regarding the bounds of the design variables, the bounds for the angle, θ_k , and length, l_k , has to be specified. For the angles, no limits are specified, as the cuts are simply rotating inside the plunger. The full rotational design space can be reached while limiting θ_k to be between 0° and 360° , however some undesirable scenarios might occur. An example would be if a cut is placed at exactly 360° . If a better solution exists at a slightly higher angle of for instance 365° (or 5°), the optimisation algorithm cannot easily move the cut to this position, as this would require a large change in the design variable. In this example, this would require the algorithm to move the variable from the upper bound directly to the lower bound, which is not preferable.

Regarding the bounds for the length l_k , the lower bound is specified to be -20.15 mm while the upper bound is 20.15 mm. The radius of the plunger is 20 mm, so by allowing the cuts to be placed at e.g. 20.15 mm, the cut can be placed outside the plunger which effectively removes the cut. With this ability to remove cuts, the optimisation algorithm could run with an arbitrary number of cuts, and if an optimal solution is to remove some of the cuts, this would be possible. However, due to the choice of cost function, the removal of plunger area is not penalised. This means that with a high number of cuts, a lot of the plunger area could potentially be removed. While it is allowable to remove some area, and therefore reduce the DC force, removing too much area will reduce the possible force below the requirement. This could be avoided with an area constraint, however instead the number of cuts are predetermined to comply with the required area.

From Equation 1.1 the force is proportional to the area, the maximum allowable amount of area, which can be removed, is calculated. With the current design, 700 N can be reached with a coil current of 5 A and an air gap length of 2 mm. With a total of eight cuts, it is possible to remove a maximum of approximately 8% of the plunger area, which therefore removes approximately 8% of the force. This would give a resulting DC force of 644 N. This is above the required 600 N, which means potentially more material could still be removed, however some headroom in the achievable force is desired. Using Equation 1.1 it can be calculated that if the air gap is increased to more than approximately 2.1 mm, the target force of 600 N cannot be reached. As this is an increase of 0.1 mm, it is deemed undesirable to remove any more material, as this would further reduce the headroom. Regarding the increase of the 0.1 mm, it is deemed difficult to guarantee that the air gap length precision is within less than 0.1 mm when assembling the setup. The optimisation procedure is therefore limited to use a maximum of eight cuts.

This means that no explicit constraints are defined for the problem. Only the bounds for the degrees of freedom are specified.

6.6 Optimisation algorithm and solver

To solve the optimisation problem a suitable algorithm is to be used. Here one of the MATLAB optimisation problem solvers is used. As a first step it is to be decided whether a gradient based optimiser is usable. As the problem and the cost function requires COMSOL simulations, the problem is implicit. The gradients are calculated by the means of finite difference, which requires a function call to COMSOL for each degree of freedom. With eight cuts there are 16 degrees of freedom. A function call takes ~ 60 s, meaning that calculating all gradients in a given point takes approximately 16 min. If the problem is convex this computational time for the gradient evaluations are acceptable, as a gradient based optimisation algorithm should converge to the global minimum within a finite amount of steps.

It is not directly indicated from the problem whether it is convex or non-convex. If the problem is convex, a gradient based method is preferable. If the problem is non-convex, more caution has to be taken if a gradient based method is to be used, especially if the problem is also non-smooth. This requires more care to be taken in relation to the initial guesses of the optimisation. In regards to this optimisation problem the initial points are some predefined initial cut design patterns.

6.6.1 Initial study of problem convexity

For an initial study of the problem, MATLAB's general purpose gradient based optimisation algorithm "fminunc" is used, due to its ease of use. From this study it is concluded that the problem is non-convex. More specifically it is found that the algorithm has difficulty in changing the initial pattern of the cuts. In a general sense the patterns can only change if the algorithm changes the intersection between the cuts. This is illustrated with a example below. Here the intersections are marked with red dots.

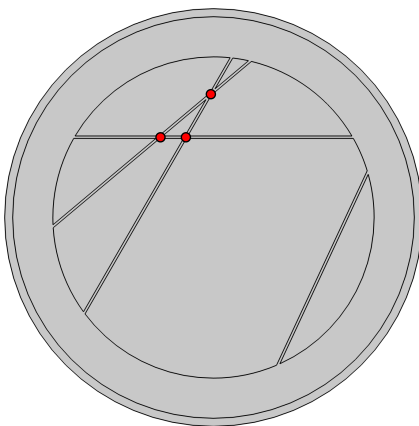


Figure 6.28. Initial point with marked intersection points.

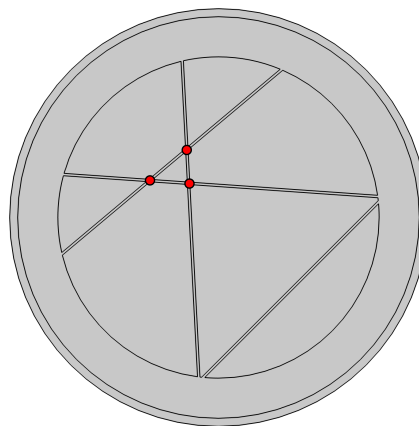


Figure 6.29. Optimised design using gradient based algorithm.

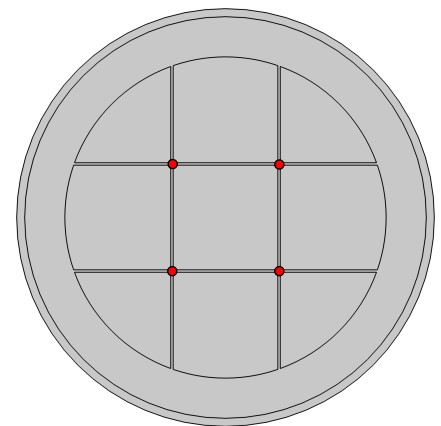


Figure 6.30. Example of better solution.

In Figure 6.28 the initial guess for an optimisation procedure is shown. In Figure 6.29 the result of using the gradient based optimisation is shown. Here it is seen that while the general size of each segment is more even, the intersections between the cuts remain the same. This is a general tendency, where the initial pattern is mostly maintained. While the pattern in Figure 6.29 yields a lower cost function value than Figure 6.28, several other design patterns exists which yields an even lower cost function value. An example of this is shown in Figure 6.30.

It is deemed necessary to make use of global optimisation tools since the cost function is non-convex. The gradient based algorithms are found to be too dependent on the initial patterns. A general conclusion of this initial study is that the optimal local solutions seems to be designs in which the area of each segment is evenly distributed.

6.6.2 Global optimisation

To solve the problem, MATLAB's global optimisation toolbox is utilised. Within the toolbox multiple solvers exist, which each have several advantages and disadvantages. Among the different solvers, the "surrogateopt" algorithm is deemed to be the best choice. According to MATLAB it is a preferable solver for problems with time-consuming function evaluations (MATLAB 2022b). Using the "surrogateopt" solver, the computational time in MATLAB is slightly higher compared to other solvers, as this algorithm builds a surrogate model, which has to be updated at each iteration. This model is an approximate model, which has the advantage of having a very low function evaluation time (MATLAB 2022a). Using this algorithm, it is possible to rapidly minimise this surrogate model, which provides a qualified guess for better solutions to the problem, which are called adaptive points. To build the model, the algorithm approaches the problem in a stochastic manner meaning it chooses random points in which the model is evaluated.

Besides the main advantages of using a global solver, there are two other benefits of this algorithm. Firstly, the algorithm has a checkpoint-file option, which allows the solver to be interrupted and restarted from where it was stopped. This interruption can be either from the user or due to a crash of any sort i.e. the computer, MATLAB or COMSOL. Secondly, the solver can be passed a NaN value from the function evaluation, which it then simply disregards in the surrogate model. This is especially useful due to the way COMSOL is called from MATLAB. Inside COMSOL the geometry is quite significantly altered when the cut pattern is changed. This is automated, however in rare cases a problem occurs where COMSOL simply returns an error to MATLAB. This is also the case when meshing the geometry, which also is handled automatically. In these cases the MATLAB function, which handles calculation of the cost function, returns NaN. These two benefits significantly increases the robustness of the optimisation procedure as any COMSOL error is handled automatically without the need to intervene. At the same time any crash simply requires the problem to be restarted form the checkpoint-file.

In the interest of reducing computational time, the design variables are converted from being continuous to integer, i.e. divided into a finite amount of possible lengths and angles. This reduces the design space, which should reduce computational time, but might also remove possible patterns. The potential removal of patterns is dependent on the specific division of the angles and lengths. For the length, the total amount of possible values is set to 136. With the length ranging from -20.4 mm to 20.4 mm, the cuts can be placed with a minimum distance of $20.4 \cdot 2 / 136 = 0.3$ mm between each other. This distance is equal to the width of the cuts, meaning that two cuts with the same angle is either exactly on top of each other, just touching each other or not intersecting at all. In regards of the angle, the subdivision is chosen to be 7.5° . This will limit the amount of possible patterns, however there is still a vast amount of obtainable designs.

6.7 Results

The results of using the "surrogateopt" global optimisation algorithm is shown in Figure 6.31. In the plot several points are marked which are defined by the "surrogateopt" algorithm (ibid.). The surrogate reset marks the end of the "search for minimum" phase, in which the surrogate model is used to search for a minimum. At this point the next adaptive point in the model is within a specified tolerance to the previous adaptive points, meaning the model is to be expanded with new random function evaluations. The lines marked "Checkpoint Resume" is where the algorithm has been restarted from a check point file. The points marked "best" is the best value found yet, while the points marked "incumbent" is the best value found yet since the last surrogate reset. The "random samples" is the random points at which the problem is evaluated to build the surrogate model. The "adaptive samples" are the evaluations of the cost function in the candidate points found from the surrogate model.

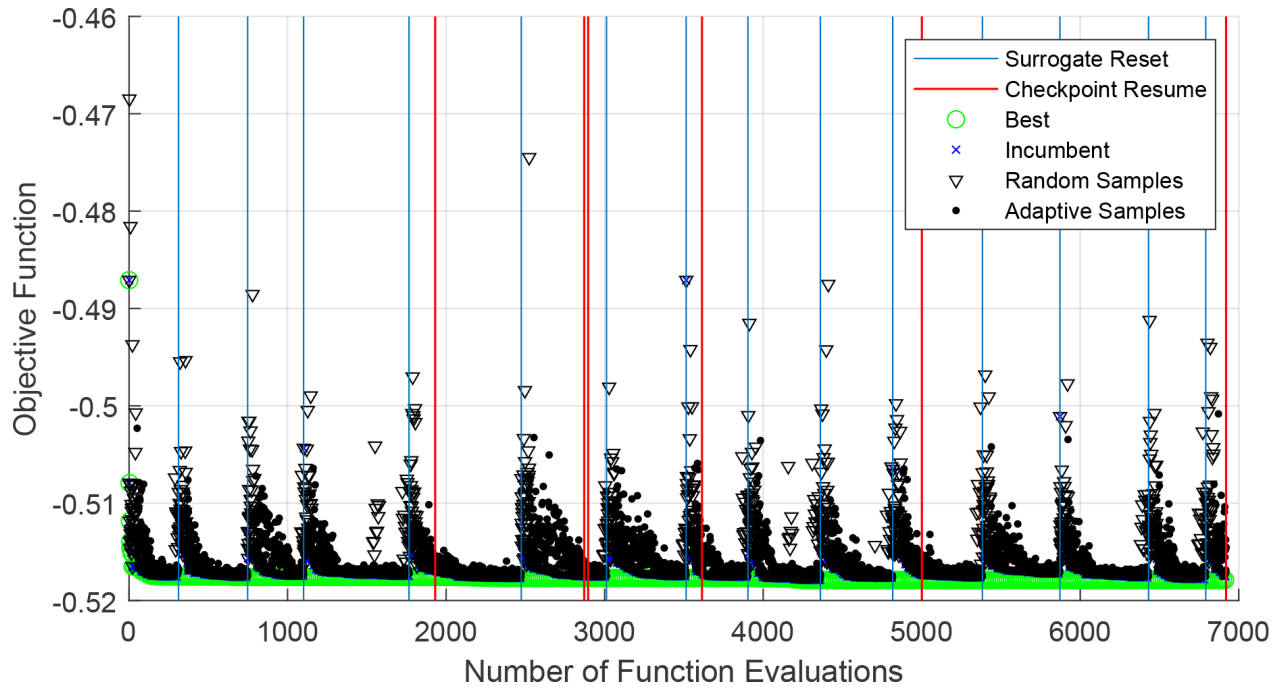


Figure 6.31. Result of global optimisation algorithm.

The algorithm is terminated after evaluating 3000 consecutive designs without finding a better solution. The design with the lowest function value found with the "surrogateopt" algorithm is shown in Figure 6.32. Besides from two cuts, the design appears to be a parallel cut pattern. The cost function value of the best design is -0.51790 . The second best design found in the optimisation, with a pattern different from the best solution, is shown in Figure 6.33. This design has a cost function value of -0.51704 . As a reference a plunger without cuts have a cost function value of -0.43963 , so the two designs are respectively 17.8% and 17.6% better. Despite a quite significant difference in the patterns, they seem to have a similar performance.

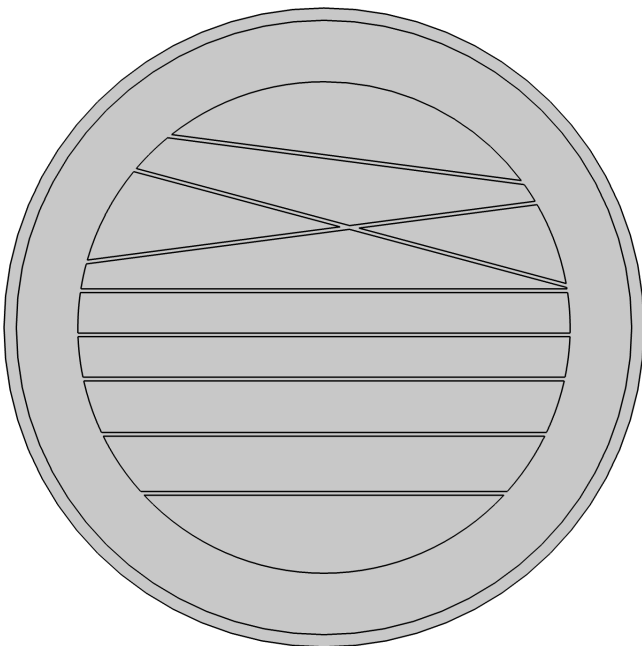


Figure 6.32. Best design pattern found by the optimisation algorithm.

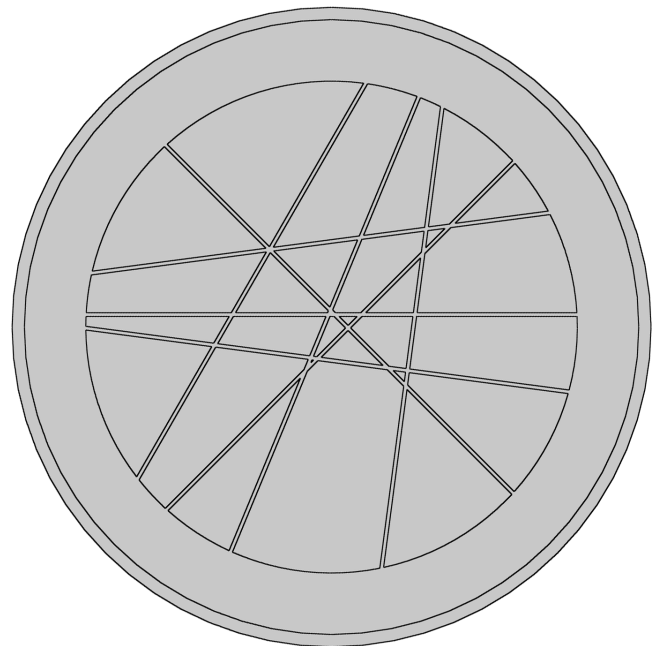


Figure 6.33. Second best design pattern found by the optimisation algorithm.

Both designs appears to resemble systematic patterns, while being slightly uneven. As a strategy to further decrease the cost function value, the two designs are used as initial guesses for non-integer gradient based optimisation. As described above, the gradient based algorithms have difficulty in changing the pattern, however they have good performance when they are to find the optimal placement of the cuts for a specified pattern. For the initial guesses the systematic patterns are extracted from the above results. It is only of interest to place the cuts at the optimal position within the given patterns rather than finding new patterns. The initial guesses for the gradient based optimisation are shown in Figure 6.34 and 6.35.

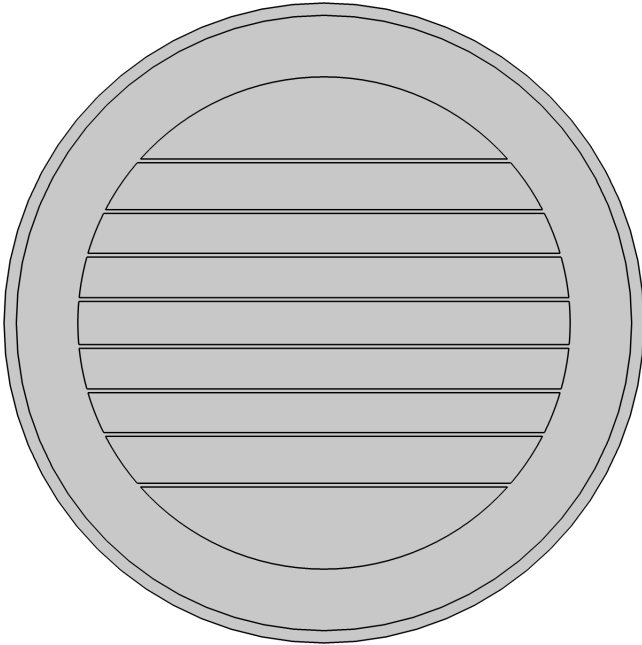


Figure 6.34. "Parallel" pattern initial guess for the gradient based optimisation.

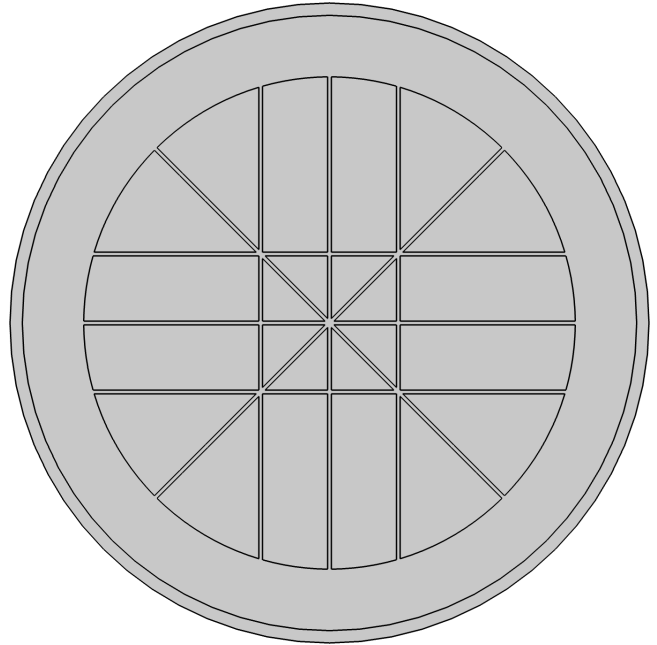


Figure 6.35. "Cross" pattern initial guess for the gradient based optimisation.

Using a gradient based algorithm, the cost function value for both designs are decreased. For the parallel design the improved cost function value is -0.51804 , and for the "cross" design it is -0.51794 . This is an improvement of respectively 17.84% and 17.81% with respect to the plunger with no cuts. The design with the parallel cuts are again the best, however the difference between the designs are even less than before.

When using a global optimisation algorithm it is not obvious if the global optimum is found. According to MATLAB, it is proven that the "surrogateopt" algorithm will converge to the global optimum (MATLAB 2022b). Despite running for a total of ~ 192 h, and not improving the design in the final 3000 iterations, it was still possible to slightly improve the best designs by using a gradient based solver. This means the "surrogateopt" did not find the global optimum, but it might have found the best pattern in terms of a parallel pattern. This cannot be proven, however this design is accepted. It is also peculiar that the second design is a completely different pattern, while still having almost the exact same cost function value. This could indicate that these designs are at the limit of how much the cost function can be decreased with eight cuts.

With an optimised design a 3D model simulation including both the improved plunger and center piece as well as the improved aluminium tubes can be done. The result of this is shown in Figure 6.36. The results for the model of the original system and the system with the improved aluminium tubes are showed for reference.

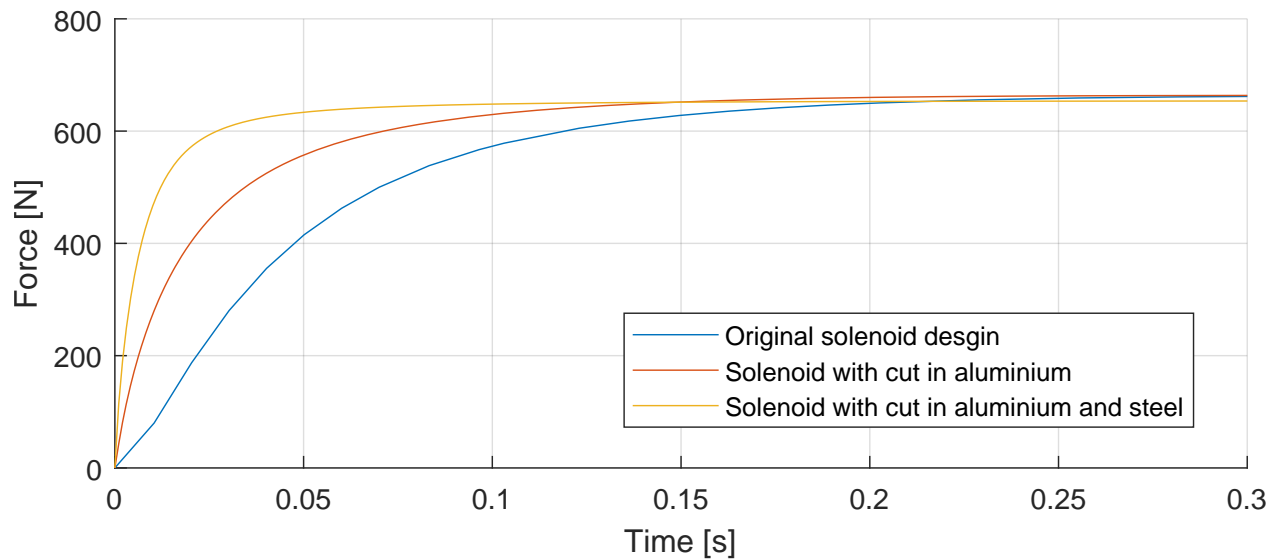


Figure 6.36. Simulated step response of proposed systems.

From the results it appears that the design with improved plunger, center piece and aluminium tubes has the fastest magnetic dynamics. For reference, the original design has a settling time of 0.155 s, while the new design have a settling time of 0.038 s, which is approximately four times faster. This is quite a significant improvement, and this design is therefore accepted. In the simulation the electrical dynamics are not accounted for, as the current rises instantaneously to 5 A. As has been argued earlier, the speed of the electrical system is expected to decrease.

6.8 Manufacturing and test of cut design

In order to test the optimised plunger and center piece, the components are manufactured. The depth of the cuts is for the center piece chosen based on keeping the structural integrity of the part. The part is to be pressed into the bottom cap, so the part of the center piece pressed into the bottom cap is kept solid. For the plunger, the cut depth is determined such that the cut ends at the top of the non-working air gap. The two manufactured components are shown in Figure 6.37 and 6.38.



Figure 6.37. Optimised plunger and center piece.

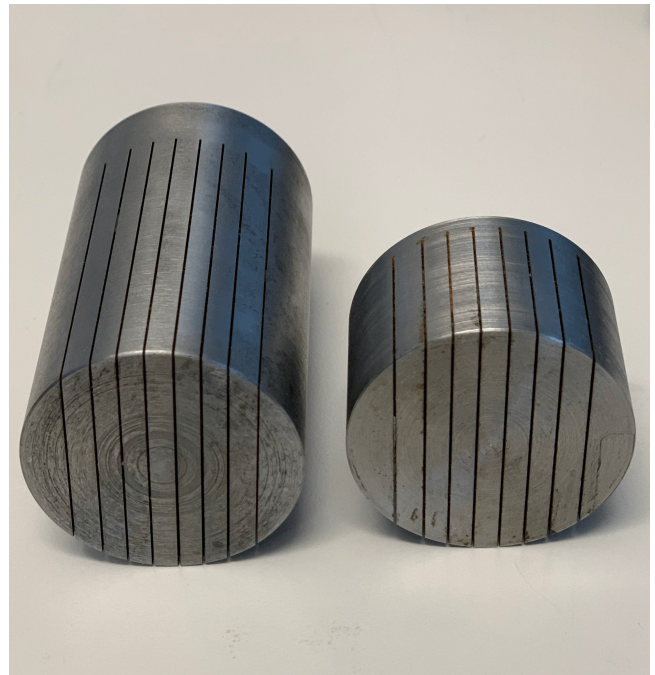


Figure 6.38. Optimised plunger and center piece.

With a prototype available, a sine sweep experiment is conducted, as described in section 3.1. The results of the force response is shown in Figure 6.39.

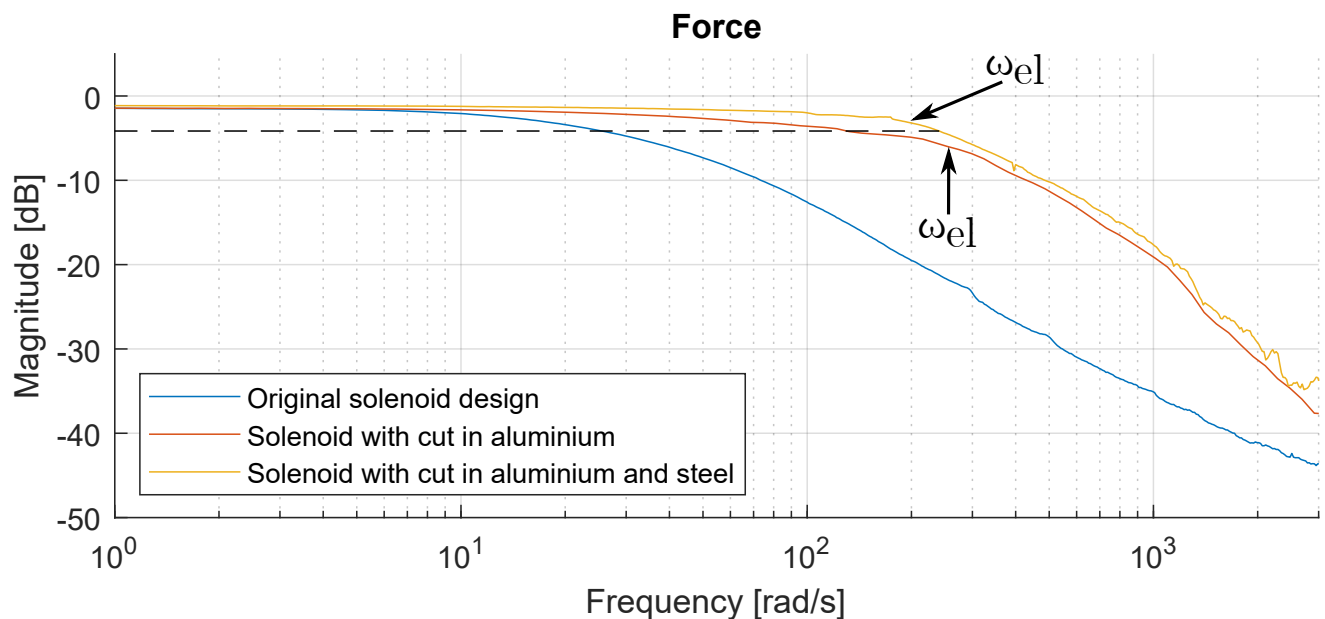


Figure 6.39. Measured force frequency response of the original system compared to the improved systems. The dashed line shows the 3 dB drop off for the best system.

The other two systems are again included for reference. For the force response of the original system and the system with the cuts in the aluminium tubes, the bandwidth is found to be 5 Hz and 24 Hz, respectively. With this improvement of making the cuts in the plunger and center piece, the bandwidth has been experimentally found to be approximately 38 Hz. Compared to the original system, the bandwidth has almost been increased with a factor of eight. In terms of the system with the improved aluminium tubes, this is an increase of around 60%. This is a slightly smaller percentage wise increase than what is seen in the step response simulations in Figure 6.36. The belonging current responses measured in the

experiments are shown in Figure 6.40.

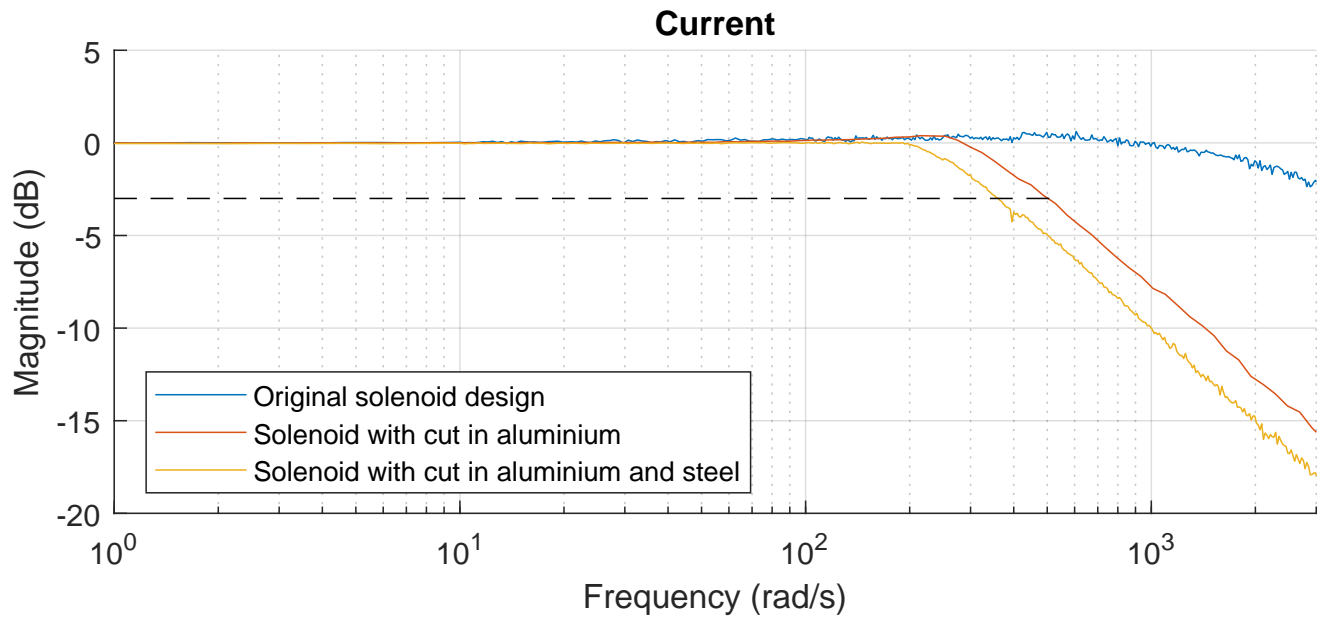


Figure 6.40. Measured current frequency response of the original system compared to the improved systems. The dashed line shows the 3 dB drop off.

Again it is seen in the current responses, that the speed of the electrical system has been decreased. The bandwidth of the electrical system for the solenoid with cuts in the aluminium and the steel is approximately 58 Hz. While the bandwidth of the electrical system response is still slightly higher than the bandwidth of the force response, it appears that the system is close to the limit at which they obtain the same bandwidth. In the electrical responses, the drop off starts more distinct. In Figure 6.39 the two frequencies at which the electrical system starts to drop off is marked. Here it is noticed that for the system with cuts in both the aluminium and steel parts starts having a drop off in the electrical system before the bandwidth frequency of the force system. This indicates that the overall system bandwidth cannot be increased much more, if any at all, and would instead require improvements of the electrical system.

6.9 Subsidiary conclusion

In this chapter an analysis and an optimisation process are conducted on the plunger and center piece of the solenoid. These two pieces are shown to include the majority of the remaining eddy currents in the system. It is shown that a 2D model can be used as an alternative to a computationally heavy 3D model. While the 2D model cannot give absolute results equivalent to those of the 3D model, it is shown that it can be used to predict the relative difference between different cut pattern designs. An optimisation is conducted based on this 2D model where a global optimisation algorithm is used to find an optimal cut pattern for the plunger and center piece. This cut pattern is used to make prototype parts which are manufactured and tested. Here it is shown that this improved design increases the bandwidth of the system with 60% compared to the previous system iteration. A bandwidth of approximately 38 Hz is reached with this improved design.

While the bandwidth is significantly improved with the cuts, it is seen in Figure 6.39 that the DC gain is below zero, meaning that the system cannot perfectly track a reference signal with the feed forward alone. Therefore work is done on implementing a feedback controller in the following chapter.

In this chapter the implementation of a controller, and its ability to increase the performance of the optimised solenoid actuator, is examined. This is mainly focused on increasing the bandwidth of the system, as well as improving the reference tracking capabilities. To achieve this, the following initiatives have been taken regarding the control of the solenoid actuator:

- The main goal of the controller is to increase the bandwidth of the system. Therefore a proportional controller is implemented.
- Requirement four in section 2.1 states that the system must be able to track a DC input with zero steady state error (within a minor tolerance range). An integral controller is therefore implemented in the system to enhance steady state performance.
- The system is highly non-linear around an input of 0 A, where the system gain changes sign. Meaning that an input current of -1 A and 1 A gives the same output force, if hysteresis is disregarded. This can also be seen in Equation 4.20 on page 18, where the flux density is squared. This is a problem in regards to the feedback control, as the sign of the system gain has to be taken into consideration. In order to detect the sign of the system gain, a Kalman filter is proposed.
- In order to aid the controller, a dynamic feed forward is implemented. This dynamic feed forward is based on the non-linear model. To implement this, the proposed Kalman filter is modified to estimate the required variables used for the dynamic feed forward.

To give an overview of the final control structure, it is presented in Figure 7.1. The details of each block are covered in the following sections.

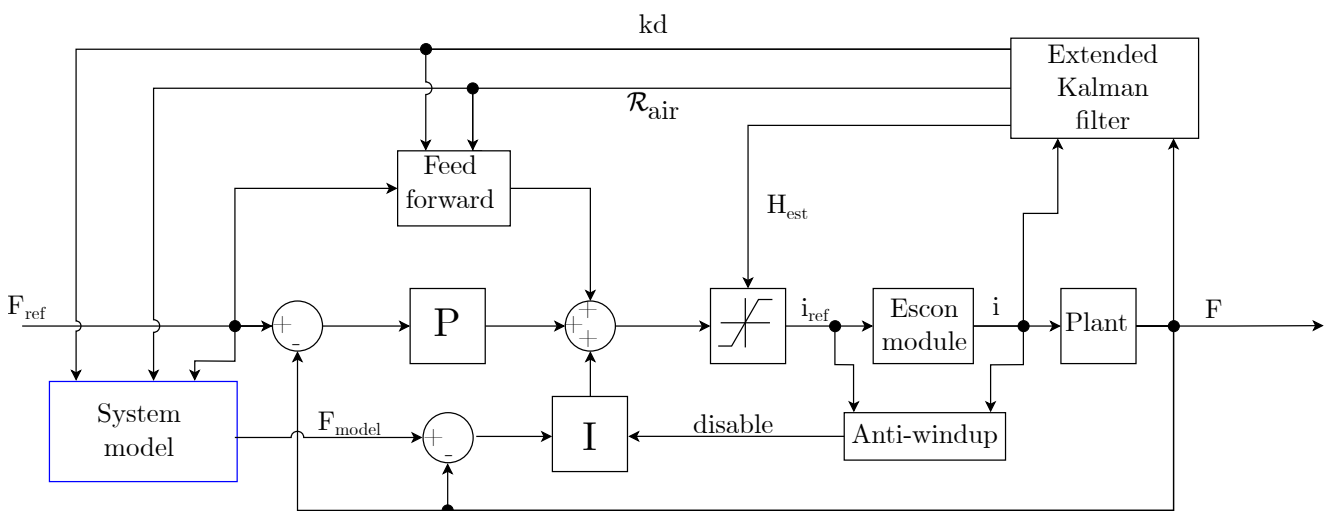


Figure 7.1. A block diagram showing the general control structure of the solenoid actuator. A block diagram of the system model can be seen in Figure 7.7 on page 63.

A Kalman filter is proposed to estimate the air gap reluctance, \mathcal{R}_{air} , the knock-down factor, kd and the magnetic field intensity, H_{est} , in the solenoid during operation. The Kalman filter is based on the non-linear model of the system presented in section 4.1. Therefore the model parameters must be updated after the geometrical changes have been made to the aluminium center tube, the plunger and the center piece. The parameters are found with the same procedure as described in Section 4.1 on page 16, and is shown in Table 7.1:

Parameter	Value
k_{ec}	6303 A V^{-1}
kd	0.70
\mathcal{R}_{air}	$979\,938 \text{ H}^{-1}$

Table 7.1. Offline estimated model parameters for optimised geometry.

The simulated and measured data is shown in Figure 7.2. The RMSE is found to be 17N, which is similar to the value found using the model without hysteresis for the original system. It is therefore assessed to be sufficiently accurate for the succeeding work.

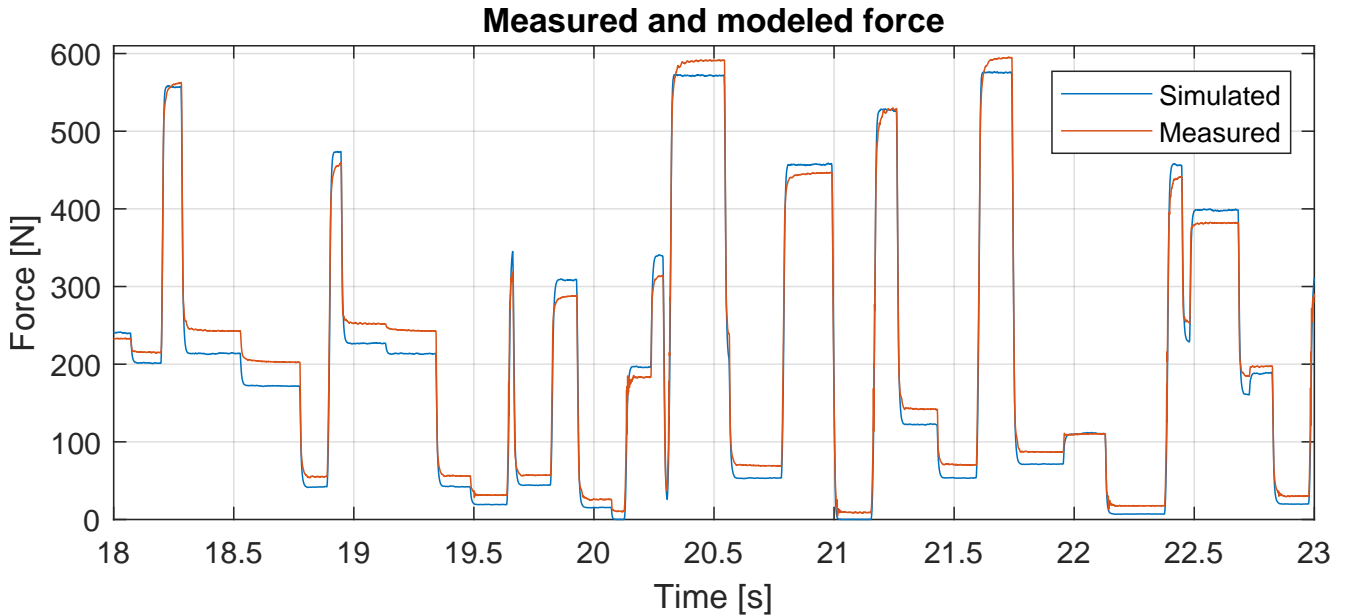


Figure 7.2. Comparison between simulated and measured data from a part of the 60s validation test.

In the following sections the individual blocks of Figure 7.1 are presented. The control system strategy is gradually implemented.

7.1 Dynamic feed forward from non-linear solenoid model

To initially improve the performance of the system, the proposed lookup table feed forward presented in section 3.2 is reconsidered. The lookup table feed forward requires experimental tests to be conducted whenever a change is made to the system, in order to ensure that the lookup table data reflects the actual system. A dynamic solenoid model, developed in section 4.1, is now available. It is therefore advantageous to use this model as feed forward, as it can be updated dynamically during operation of the actuator. By using the Kalman filter, proposed in section 7.3, the parameters used in the model based feed forward can be continuously adjusted in order to reflect the actual solenoid actuator system.

Since the feed forward is to be based on steady state, Equation 4.18 on page 18 can be modified in order to calculate the steady state input to the system required for a given reference. The following applies for steady state:

$$\frac{dH_{steel}}{dt} = \frac{N \cdot i - B_{steel}(H_{steel}) \cdot A_{steel} \cdot \mathcal{R}_{air} - H_{steel} \cdot l_{steel}}{k_{ec} \cdot \mu'(H_{steel}) \cdot A_{steel}} = 0 \quad (7.1)$$

$$i = \frac{B_{steel}(H_{steel}) \cdot A_{steel} \cdot \mathcal{R}_{air} + H_{steel} \cdot l_{steel}}{N} \quad (7.2)$$

Since A_{steel} , \mathcal{R}_{air} , l_{steel} and N are known parameters, the only unknowns are H_{steel} and B_{steel} , which are dependent on each other. In steady state, B_{steel} can be found from Equation 4.20 on page 18, which gives:

$$B_{steel} = \frac{\sqrt{\frac{2F\mu_0\mu_{air}}{A_{steel}}}}{kd} \quad (7.3)$$

The equivalent H-field for a given B-field can be found in different ways. As the hysteresis is neglected, the relationship between the H-field and the B-field is governed by the BH-curve, as explained in section 4.1. Here the BH-curve is modelled with Equation Equation 4.23, however due to the nature of the equation the H-field cannot be isolated. Therefore another approach is needed. A lookup table is generated where mean values of the measured data for the BH-curves is used. The measured data of the BH-curves is shown in Figure 4.4 on page 21. Linear interpolation is utilised in order to find values that lies in between the points of the lookup table. The axes of the BH-curve are then inverted in order to find the H-field to a given B-field. The data for the inverted BH-curve is shown in Figure 7.3.

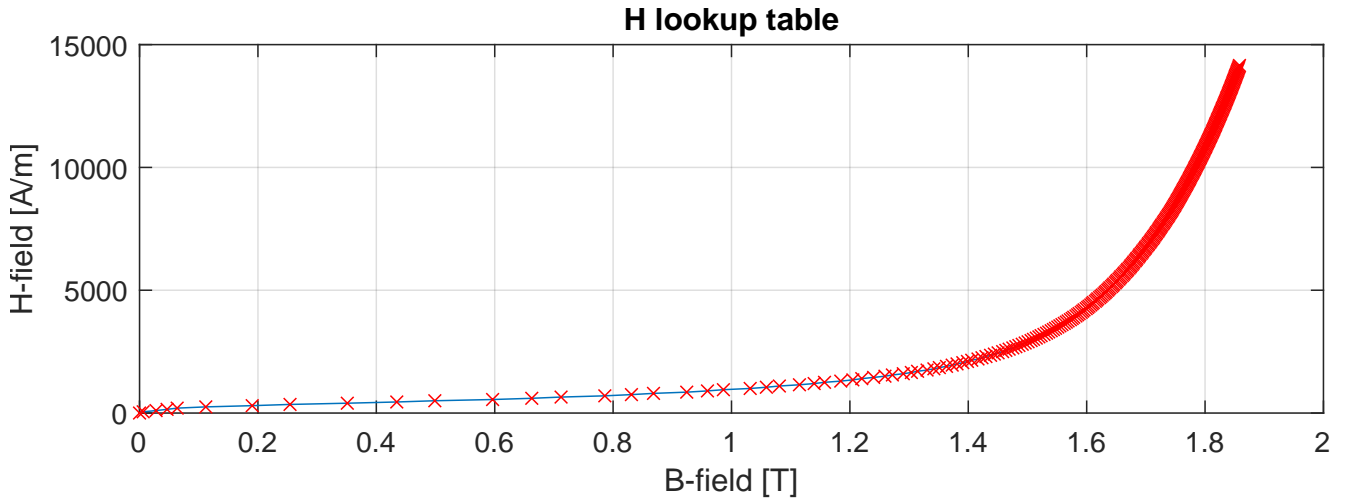


Figure 7.3. The lookup table values and linear interpolation used to find the H-field for a given B-field.

The basic structure of the model based feed forward algorithm is shown in the flowchart in Figure 7.4. It shows how the solenoid model and lookup table are used to calculate the necessary current to reach a force reference. This algorithm has the benefit compared to the original feed forward, that it is based on system parameters. If there is a known change in one or more of the parameters, it is not necessary to run a series of new tests in order to recalculate the feed forward, as it is for the feed forward proposed in section 3.2. Here the parameters in Equation 7.2 and 7.3 can be changed to adjust the feed forward.

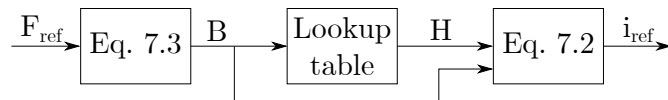


Figure 7.4. The basic structure of the model based feed forward algorithm.

As the feed forward is capable of dynamically adjusting its model based on changes in the parameters, an algorithm capable of estimating these parameters during operation would increase the feed forward performance. Therefore a Kalman filter is proposed in section 7.3, as this can be developed such that it can estimate the relevant parameters.

The performance of the feed forward can be seen in Figure 7.5. It is expected that the model based feed forward works as well as the lookup table based feed forward if the parameters are estimated correctly. The model based feed forward is not expected to perform better than the lookup table based feed forward. The possibility of taking parameter variations into account is however expected to increase the robustness of the feed forward. The model based feed forward is therefore assessed to be better. The Kalman filter, described in section 7.3, used for estimating the parameters for the model based feed forward is not implemented on the real time target. All tests incorporating the model based feed forward in this project are therefore based on offline fitted parameters based on experiments on the actuator.

7.2 Feedback controllers

With the developed feed forward a good foundation for the system is formed. The feed forward calculates the majority of the controller output. To further improve both the transient response and steady state performance feedback control is utilised. Two feedback controllers are proposed as shown in Figure 7.1.

7.2.1 Proportional controller (P)

The proportional controller for the force system is primarily implemented to improve the transient performance of the system. It is acting on the error between the force reference and the measured force from the load cell. The gain of the proportional controller is 0.02 A/N. The performance improvement from the proportional controller can be seen in Figure 7.5. The transient improvement from implementing the proportional controller is not as significant as expected. This is assumed to be due to saturation in the electrical system. Below approximately 300 N, the feed forward is fully saturating the electrical system, so the addition of the proportional controller is not increasing the initial transients. This is seen in Figure 7.6. Here the measured current for the both controllers is plotted, where it is seen that during the initial transients, the currents is rising at the same rate even though they have different references. After the 300 N mark, an improvement is however seen in both the final transients and the steady state performance.

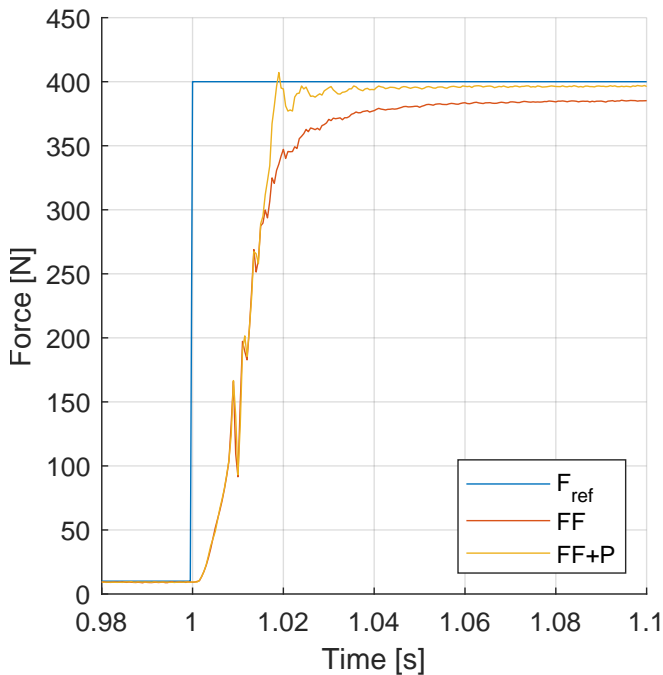


Figure 7.5. Step response of the actuator system. F_{ref} is the force reference, FF is feed forward and P is proportional controller.

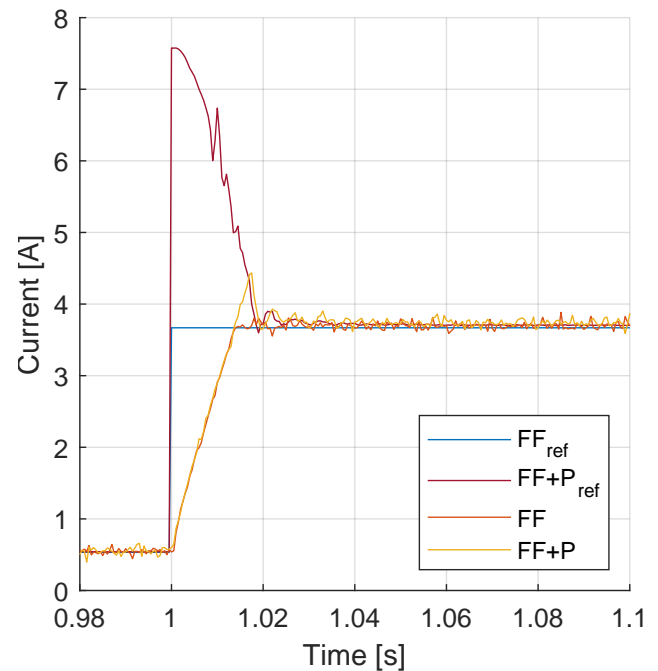


Figure 7.6. Current references and actual currents based on the force controllers shown in Figure 7.5.

7.2.2 Integral controller

Conventional Integral controller (I)

From Figure 7.5 it can be seen that while the proportional controller also improved the steady state performance of the system, an offset is still observed. To counteract this, an integral controller is implemented. Figure 7.9 shows the force response after the implementation of the integral controller, denoted "FF+P+I". A severe overshoot can be seen as a result of the integral controller trying to drive the already saturated current controller to higher currents. This results in a windup of the integrator, which is seen as the overshoot of force.

Conventional Integral controller with anti-Windup (IW)

Contrary to the proportional controller, the integral controller is not implemented to improve system transients, but instead steady state accuracy of the system. It is therefore not desired for the integral controller to react to system transients, where the current controller is in saturation, as this results in overshoots due to windup. The actual current in the actuator coil is available as an output from the ESCON module. An integrator anti-windup is therefore implemented in a way which prevents the integral controller from reacting to errors whenever the actual current deviates from the current reference by more than 0.5 A. If the currents deviates with more than 0.5 A it is assumed that the current system is in saturation. The performance of the integral controller with anti-Windup can be seen on Figure 7.9 as "FF+P+IW". In the response it appears that the majority of the overshoot is suppressed with the anti windup. There is however still an overshoot of 25 N. Therefore further initiatives are examined in order to reduce this.

Model Error Integral controller with anti-Windup (MEIW)

The conventional integral controller reacts to the error between the reference and actual force. As this will inevitably result in windup problems due to controller saturation, another idea is implemented, in which knowledge of the system is utilised. The fundamental idea is to create a model which predicts the

best possible system behaviour with the available controller effort, and then have the integral controller compensate for deviation from this model. Since the system response is well defined during controller saturation, the difference between model and reality is small during transients. When the difference between model and reality becomes small, the integrator is effectively disabled.

The model is based on the non-linear model presented in section 4.1, denoted the non linear magnetic model, with the addition of a model of the electrical system, the feed forward and the proportional feedback controller, as seen in Figure 7.7. These addition is needed to predict the behaviour of the system.

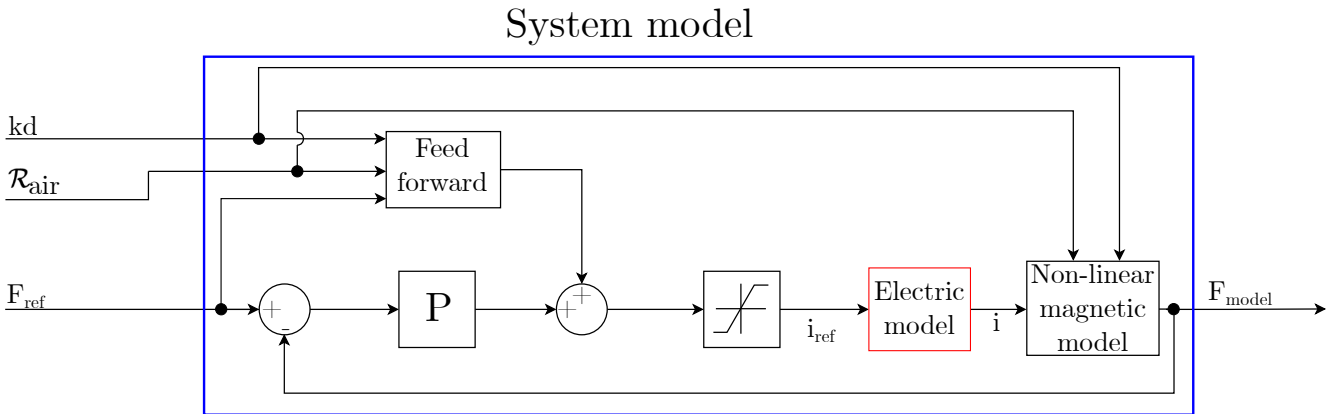


Figure 7.7. A block diagram showing the structure of the system model, that is nested in Figure 7.1.

The model of the electrical system is presented in Figure 7.8, where P_{electric} is a gain of 10000 and the coil is modelled as a first order system.

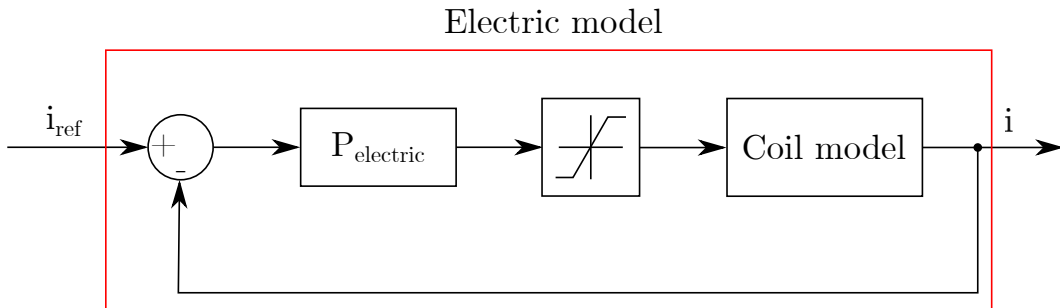


Figure 7.8. A block diagram showing the structure of the electrical model, nested in Figure 7.7.

As this system model and the feed forward is based on the same non-linear model, the system model output will always settle on the force reference, while still featuring the approximated dynamics of the system. The output from this model compared to the actual force from the system can be seen on Figure 7.10. It can be seen that the transients of the model is identical to the real system, while model settles on the force reference. The step response of the system with the model error integral controller with anti-windup can be seen on Figure 7.9 as "FF+P+MEIW". It can be seen that the implementation of the model error approach, reduces the overshoot by $\approx 50\%$ for this test, compared to the conventional integral controller with anti-windup.

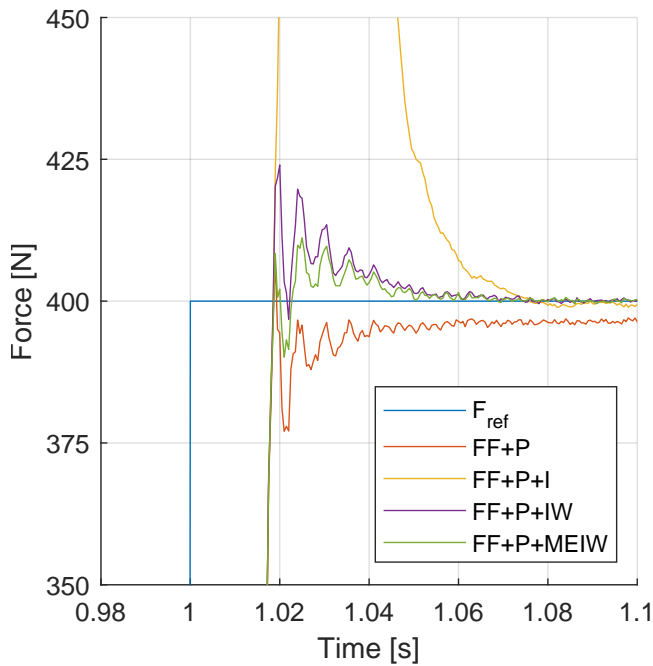


Figure 7.9. Step response of system with different controllers.

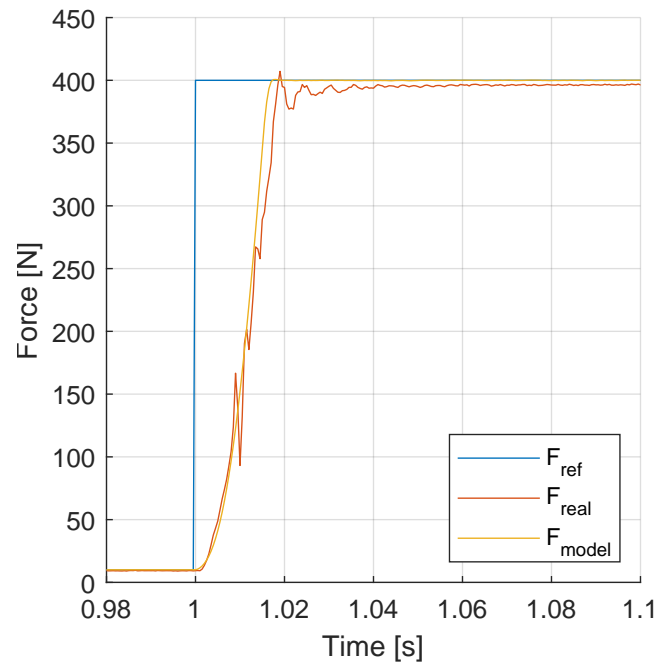


Figure 7.10. Step response of real and modelled system.

The above results are only valid when the model is sufficiently accurate. In order to correct the model parameters, to account for process variations, a Kalman filter capable of estimating model parameters is proposed.

As described in the beginning of this chapter, the system is highly non-linear around 0 N and changes the sign of the system gain. Figure 7.11 shows that this non-linearity can cause problems, which has to be addressed. It is seen that when the reference force is close to zero and the system gain changes sign, the controller mistakenly tries to correct the output in the wrong direction. However, it appears that the current controller, seen in Figure 7.12, correctly tracks the current reference.

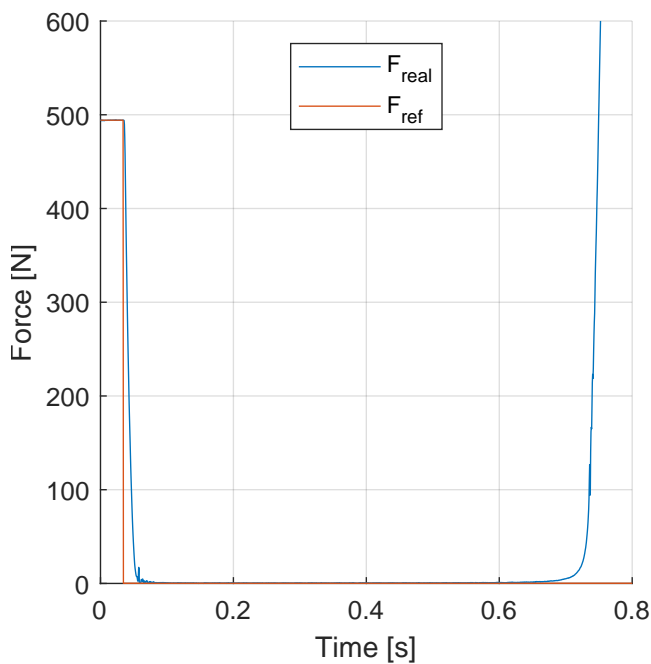


Figure 7.11. Force step from 500 N to 0 N, showing the system gain sign change problem.

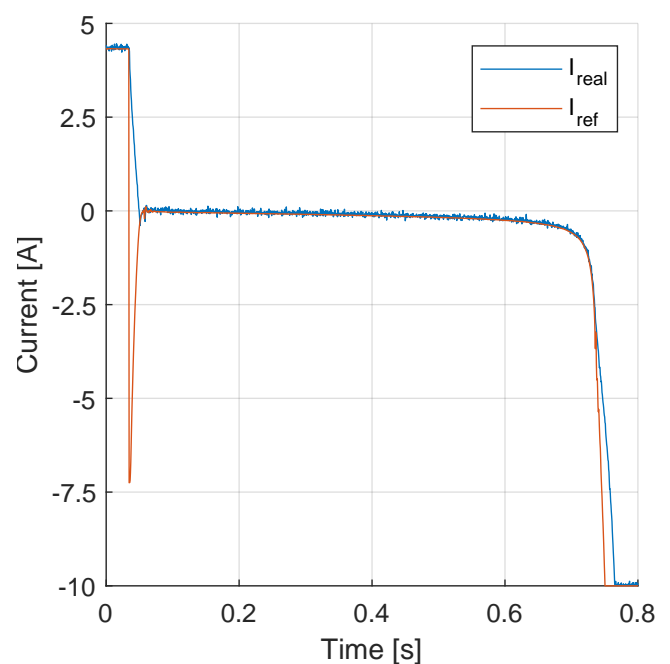


Figure 7.12. Current reference and actual current during the force step shown in Figure 7.11.

7.3 Kalman filter

In order to address the challenge, with the system gain changing sign when the magnetic field changes direction, a Kalman filter is proposed. A Kalman filter is capable of estimating states that are not directly measured. In this case the Kalman filter is to be designed such that it is capable of estimating the magnetic flux in the actuator and thereby finding zero crossings of the flux. By detecting the magnetic flux zero crossings, suitable measures can be taken in order to stabilise the control algorithm.

As described in section 7.1 and subsection 7.2.2, it is beneficial to estimate changes in the model parameters due to installation inaccuracies. This is in principle not necessary to do in real time, as these should not change, after the solenoid actuator is installed. However, the parameters might change due to unforeseen disturbances during operation. As the Kalman filter has to operate in real time to estimate the magnetic flux zero crossings, the augmented version is implemented such that any estimated changes in parameters during operation can be used to dynamically adjust the feed forward. The relevant parameters, which needs to be estimated, is kd and \mathcal{R}_{air} as these can change due to installation inaccuracies. Therefore the Kalman filter is augmented in order to estimate these parameters. The following derivation of the Kalman filter is based on Isermann (2006).

7.3.1 Linearisation

In order to design the Kalman filter it is necessary to put the governing equations on a state space form. This is done by identifying the states and then determining a linear expression for the governing equations with respect to these states. The Kalman filter is to be augmented, so it can estimate both the H-field, air gap reluctance and the knock-down factor. Therefore the air gap reluctance and knock-down factor has to be states as well.

$$\dot{x} = Ax + Bu + Vv \quad (7.4)$$

$$y = Cx + n \quad (7.5)$$

Where x is a vector containing the states, A is the system matrix, B is an input vector, u is input to the system, v is a vector of stochastic variables containing information about the process noise. This could be input noise or disturbances in the system. V is a matrix that contains information about how the process noise translates into the state derivatives. y is the output, C is the output vector and n describes sensor noise in the output.

$$x = \begin{bmatrix} H \\ \mathcal{R}_{air} \\ kd \end{bmatrix} \quad (7.6)$$

$$u = i \quad (7.7)$$

Hereafter the following notation is used: $x_1 = H$, $x_2 = \mathcal{R}_{air}$ and $x_3 = kd$. The first governing equation is the solenoid model found in chapter 4. Since the air gap reluctance and the knock-down factor are assumed slowly varying, the three governing equations become:

$$\frac{dH_{steel}}{dt} = \frac{N \cdot i - B_{steel}(H_{steel}) \cdot A_{steel} \cdot \mathcal{R}_{air} - H_{steel} \cdot l_{steel}}{k_{ec} \cdot \mu'(H_{steel}) \cdot A_{steel}} \quad (4.18)$$

$$\frac{d\mathcal{R}_{air}}{dt} = 0 \quad (7.8)$$

$$\frac{dkd}{dt} = 0 \quad (7.9)$$

In order to put these equations on a state space form, the three equations are partially differentiated with respect to all three states:

$$A = \begin{bmatrix} \frac{d\dot{H}}{dH} & \frac{d\dot{H}}{d\mathcal{R}_{air}} & \frac{d\dot{H}}{dkd} \\ \frac{d\dot{\mathcal{R}}_{air}}{dH} & \frac{d\dot{\mathcal{R}}_{air}}{d\mathcal{R}_{air}} & \frac{d\dot{\mathcal{R}}_{air}}{dkd} \\ \frac{dkd}{dH} & \frac{dkd}{d\mathcal{R}_{air}} & \frac{dkd}{dkd} \end{bmatrix} = \begin{bmatrix} \frac{d\dot{H}}{dH} & \frac{d\dot{H}}{d\mathcal{R}_{air}} & 0 \\ 0 & 0 & 0 \\ 0 & 0 & 0 \end{bmatrix} \quad (7.10)$$

$$B = \begin{bmatrix} \frac{d\dot{H}}{di} \\ \frac{d\dot{\mathcal{R}}_{air}}{di} \\ \frac{dkd}{di} \end{bmatrix} = \begin{bmatrix} \frac{d\dot{H}}{di} \\ 0 \\ 0 \end{bmatrix} \quad (7.11)$$

The C matrix is found based on Equation 4.20 on page 18, where $B_{steel}(H_{steel})$ is calculated based on the material model found in Equation 4.23. Thereby the output vector, C , becomes:

$$C = \begin{bmatrix} \frac{dF}{dH} \\ \frac{dF}{d\mathcal{R}_{air}} \\ \frac{dF}{dkd} \end{bmatrix} = \begin{bmatrix} \frac{dF}{dH} \\ 0 \\ \frac{dF}{dkd} \end{bmatrix} \quad (7.12)$$

7.3.2 Prediction

A Kalman filter consists of two primary steps, a prediction step and a correction step. The prediction step uses the incorporated model to predict the states for the coming time step. The correction step compares a measurement and the predicted state value and weights them based on covariance of the sensor noise and process disturbance. The prediction step is examined in the following.

k indicates a discrete time step and a notation like eg. $x(k+1|k)$ is used in the following. The first part, $k+1$, means it is the predicted state estimate for the next time step, while the second part, k means that it has not yet been corrected. Then $x(k+1|k+1)$ is the predicted state estimate that has also been corrected. During the prediction state, two quantities are predicted, a state estimate and a state error covariance.

Predicted state estimate

The predicted state estimate, \hat{x} , is based on the model:

$$\hat{x}_1(k+1|k) = f(x(k|k), u(k)) \quad (7.13)$$

Here either the linear model or the non-linear model can be used. The nonlinear model is chosen as this is assumed to deliver the best results. The model is to be discretised, which is shown below:

$$f(x(k|k), u(k)) = \left(\frac{N \cdot u - B_{steel}(\hat{x}_1(k|k)) \cdot A_{steel} \cdot \hat{x}_2(k|k) - \hat{x}_1(k|k) \cdot l_{steel}}{k_{ec} \cdot \mu'(\hat{x}_1(k|k)) \cdot A_{steel}} \right) T_s + \hat{x}_1(k|k) \quad (7.14)$$

where T_s is the sample time, on the real time target.

Predicted state error covariance

The predicted state error covariance, P^- , is a measure for the magnitude of the disturbance. The predicted state error covariance is calculated based on the prior state error covariance, P , and a covariance matrix,

M , describing the covariance of disturbances and process noise. The covariance matrix, M , is based on the process disturbance, v .

$$P^-(k+1) = A_d P(k) A_d^T + V M V^T \quad (7.15)$$

Where A_d is the discretised A -matrix. When the calculations for the state estimate and the predicted state error covariance in the prediction step are made, they are transferred to the correction step.

7.3.3 Correction

The correction step consists of the following three parts: Calculating the Kalman gain, correcting the state estimate and calculating a new state error covariance. This is elaborated below.

Kalman gain

The Kalman gain, K , is calculated as follows:

$$K(k+1) = P^-(k+1) C^T [C P^-(k+1) C^T + N]^{-1} \quad (7.16)$$

where N is a covariance matrix containing information about the measurement noise. The values in N is based on the sensor noise n . An intuitive understanding of the Kalman gain can be obtained by assuming that $P^-(k+1)$, C , M and N are scalars. If $P^-(k+1) \gg N$, it is seen that the Kalman gain approaches $K = 1$, while $P^-(k+1) \ll N$ makes the Kalman gain approach $K = 0$. Meaning that if the covariance of the disturbance, M , is high compared to the sensor noise covariance, N , the Kalman gain is close to 1, while a large amount of sensor noise compared to disturbance makes the Kalman gain very small. This influences the correction of the state estimate, which is explained below.

Corrected state estimate

With knowledge of the system disturbance and the measurement noise used to calculate the Kalman gain, the predicted states can be corrected. The corrected state estimate is calculated as:

$$\hat{x}(k+1|k+1) = \hat{x}(k+1|k) + K(k+1)[y(k+1) - C\hat{x}(k+1|k)] \quad (7.17)$$

where $y(k+1)$ is the measured outputs. Again an intuitive understanding can be obtained if C is assumed be 1. If the Kalman gain is close to 0 (low disturbance compared to sensor noise), there is no correction made to the predicted state estimate. If the Kalman gain on the other hand approaches 1, the two terms of predicted states cancels out and the corrected state estimate relies heavily on the measurement.

State estimate error covariance

The state estimate error covariance is calculated:

$$P(k+1) = [I - K(k+1)C]P^-(k+1) \quad (7.18)$$

where I is an identity matrix. The intuitive understanding of this is, that if the Kalman gain is close to 1, then the state estimate error covariance in the next step becomes small, while the opposite is valid for a Kalman gain close to 0. However according to Grewal and Andrews (2001) the "Joseph form" of the state estimate error covariance is numerically more stable and it is therefore implemented in MATLAB:

$$P(k+1) = [I - K(k+1)C]P^-(k+1)[I - K(k+1)C]^T + K(k+1) N K(k+1)^T \quad (7.19)$$

7.3.4 Implementation

The basic structure of the Kalman filter is laid out above, however some parameters still needs to be identified. It is the values of the matrices M and N , and the initial values of the state estimate error covariance matrix, $P(0)$.

Determination of sensor noise covariance matrix, N

N is the measurement noise covariance matrix. Since the system only measures a single quantity, the output force, N becomes a scalar. That scalar value is the variance of the force signal. Optimally the load cell is subjected to a sequence of precisely known loads or loaded in series with a calibrating load cell. The measurement noise covariance is then determined based on the difference between the load cell under test and the calibrating value. In this project the load cell is assumed to have a zero mean Gaussian distributed noise overlay. The variance is found at different load levels whereafter the average variance, used for the Kalman filter, is calculated as:

$$N = 0.047 \text{ N}^2 \quad (7.20)$$

Determination of process noise covariance matrix, M

M contains information about the uncertainty in the model and since the state space model has three states, the M -matrix is a 3x3-matrix. It is normally defined as:

$$E\{v \cdot v^T\} = M \quad (7.21)$$

Where E is the long time mean. Since the covariance information can be difficult to obtain, M is often designed as a diagonal matrix with the estimated variances on the diagonal, where the different entries defines how well the model predicts a given state. Depending on the system it might be possible to obtain information about the variance in the disturbances. However for the actuator system it is disproportionately difficult to obtain this information compared to tuning the parameters until the Kalman filter performs as intended.

The air gap reluctance and knock-down factor, \mathcal{R}_{air} and kd , are to be determined dynamically in order to update the feed forward. As it is not desired for the feed forward to react to parameter variations, due to other system dynamics, relatively small values for the variance is chosen. The changes in the parameters that the Kalman filter is to estimate are related to installation inaccuracies as well as other permanent changes to the air gap length. The estimation of the change in the parameters due to these are not needed to be done quickly. After a new installation, the Kalman filter can simply over time settle on the new values for \mathcal{R}_{air} and kd . The variance must be relatively small, however \mathcal{R}_{air} has a significantly higher numerical value than kd . Satisfactory results are therefore obtained when $\sigma_{kd}^2 = 10^{-15}$ and $\sigma_{\mathcal{R}_{air}}^2 = 10^{-8}$.

From a comparison of modelled and measured data in Figure 4.11 on page 26, it is seen that there are some disturbances, that the model does not account for. Therefore the variance ascribed to the state, H_{steel} , must be significantly larger than the variance ascribed to the two other states. An initial guess is $\sigma_{H_{steel}}^2 = 10^{-1}$. The process covariance matrix is therefore given by:

$$M = \begin{bmatrix} \sigma_{H_{steel}}^2 & 0 & 0 \\ 0 & \sigma_{\mathcal{R}_{air}}^2 & 0 \\ 0 & 0 & \sigma_{kd}^2 \end{bmatrix} \quad (7.22)$$

Determination of initial state error covariance, $P(0)$

As described in subsection 7.3.3, the state error covariance matrix, M , in relation to the sensor noise covariance matrix, N , describes whether to trust the model or measurements the most. So the initial state error covariance, $P(0)$, describes how much the model is trusted initially. This initial matrix is designed as a diagonal matrix as well. Since all three states are relatively well known in the beginning of a test, the values of $P(0)$ can be set relatively low.

$$P(0) = M \quad (7.23)$$

Testing

The Kalman filter is implemented in MATLAB and used on experimental data, where random current set points between -5 A and 5 A are applied to the actuator. After further tuning of the parameters, it is found that $\sigma_{H_{steel}}^2 = 10^{-6}$, $\sigma_{\mathcal{R}_{air}}^2 = 10^{-3}$ and $\sigma_{kd}^2 = 10^{-15}$ are the parameters that works best for the Kalman filter. For both \mathcal{R}_{air} and kd three different tests are made. Only one of the two variable is changed during each test, and the other variables are then set to the value of the offline estimation as shown in Table 7.1. From Figure 7.13 and 7.14 it is seen that the Kalman filter is slowly converging towards the same parameter value estimated by the offline optimisation.

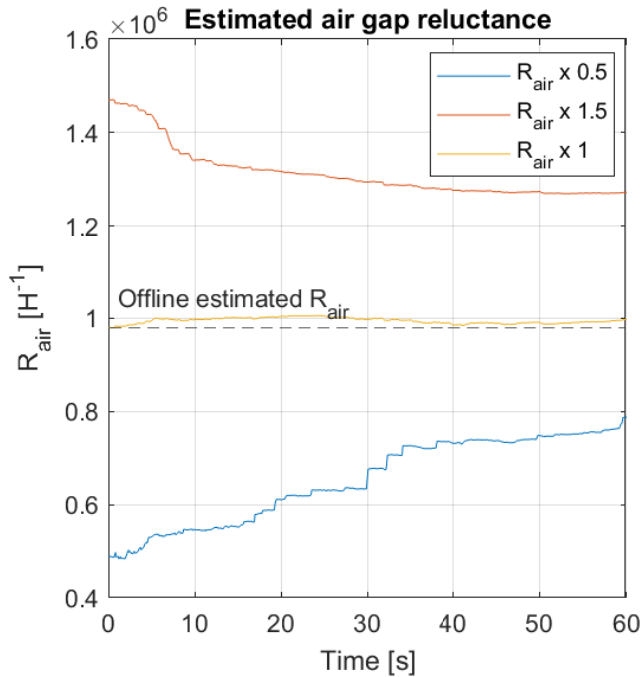


Figure 7.13. The Kalman filter estimate of the air gap reluctance during a test.

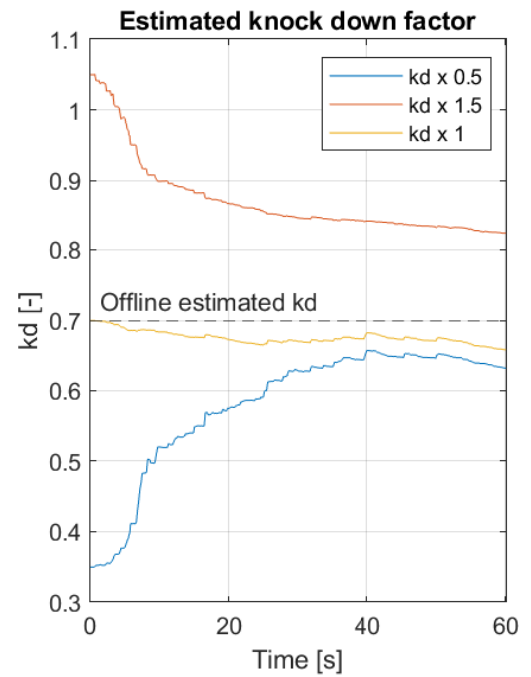


Figure 7.14. The Kalman filter estimate of the knock-down factor during a test.

Regarding the ability of the Kalman filter to detect zero crossings of the magnetic field, the estimated H-field and the measured force are plotted together in Figure 7.15 as well as the current. It is seen that, the sign of the H-field changes whenever the force has a local minimum. It is further worth noticing that the sign of the H-field and the current is consistent which means that direction of the H-field is correctly estimated.

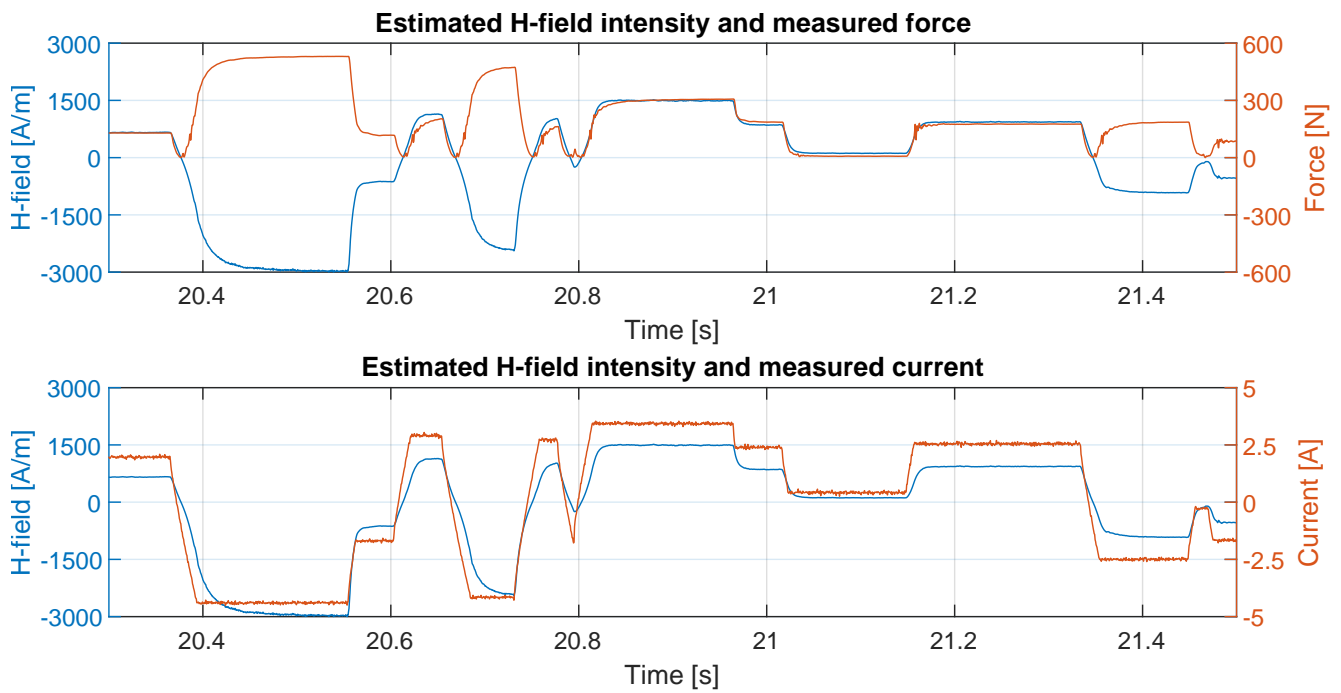


Figure 7.15. The Kalman filter estimate of the H-field intensity, measured force and measured current during a test.

By zooming into the zero crossings of the estimated H-field, it is seen that the magnetic field has a zero crossing when the force is on its lowest point, see Figure 7.16. This means that there is not any phase between the estimated H-field and the measured current. It is further seen that the estimated H-field is lagging a little behind the measured current, which indicates that the Kalman filter is capable of estimating the dynamics between the current and H-field in the solenoid actuator.

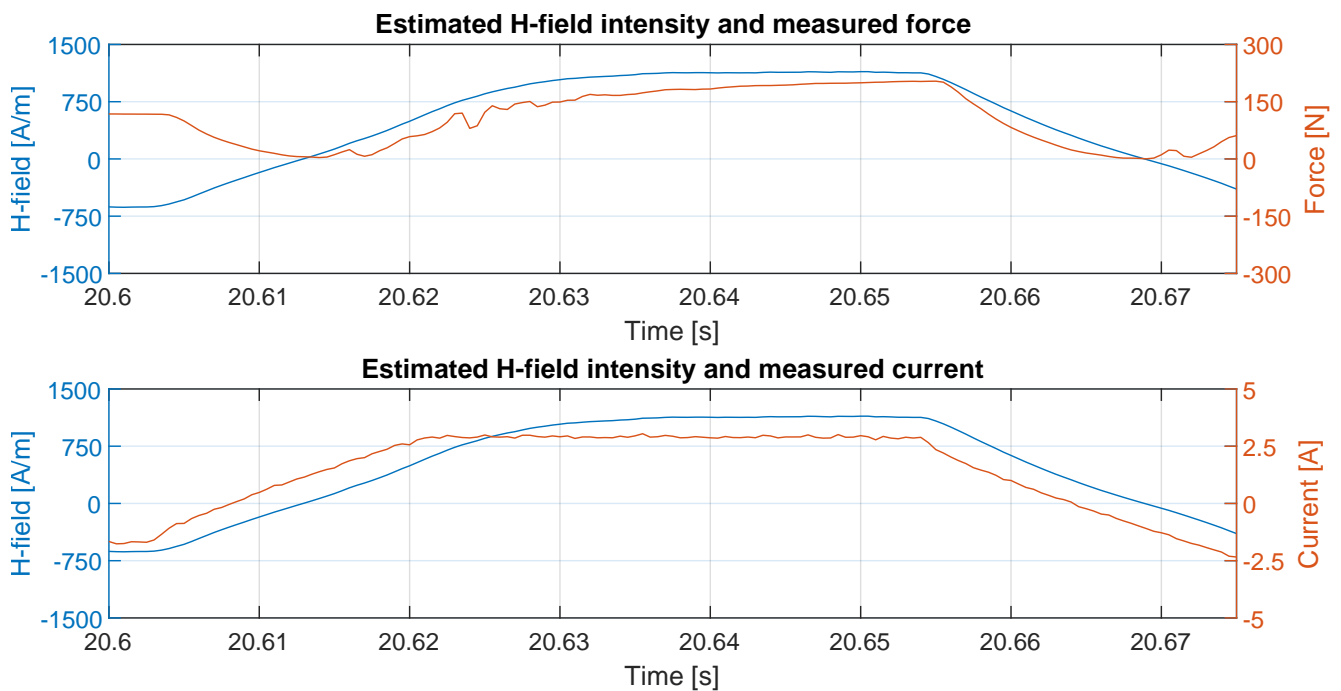


Figure 7.16. The Kalman filter estimate of the H-field intensity and the measured force during a test.

With the possibility to detect the zero crossings, the information can be used to limit the controller current reference to only the positive range whenever a negative H-field is detected. This is used to avoid

the problem seen in Figure 7.11. In this way, the controller will be kept in the operating range with positive system gain.

The Kalman filter is not implemented on the real time target, but only in MATLAB. Therefore further work is needed in order to implement it as a part of the actual control algorithm controlling the actuator, but the results above are promising and indicates that it is a feasible solution. The tuning process of the parameters in the covariance matrix M should be evaluated when the Kalman filter is to be implemented on a real time target. During the tuning of the parameters it is found that if the Kalman filter relies too much on the measured data (high $\sigma_{H_{steel}}^2$). It is not capable of detecting all zero crossings of the magnetic field, as the force measurements does not contain information about the direction of the magnetic field. The Kalman filter is especially sensitive to an offset on the load cell output, so a larger offset on the load cell require a decrease in $\sigma_{H_{steel}}^2$, which means that the model is trusted more.

7.4 Control results

With the control algorithm in place, a test to estimate the bandwidth of the system with controller is performed as described in section 3.1. The frequency response found in this bandwidth test is seen in Figure 7.17, where the frequency response of the system without controller is also shown for reference.

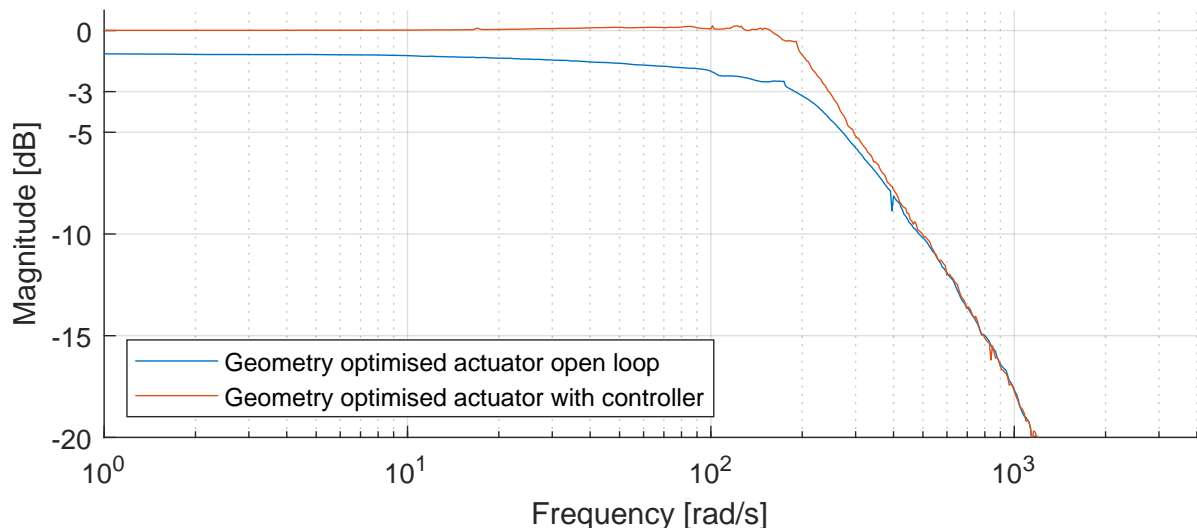


Figure 7.17. Frequency response of solenoid actuator with and without controller. Tested according to section 3.1

The geometry optimised actuator in open loop reaches a bandwidth of 240 rad/s (38.2 Hz), while the geometry optimised actuator with controller reaches a bandwidth of 245 rad/s (39 Hz). This means that bandwidth increase from implementing the controller is limited. It is however seen that the controller is capable of delivering accurate steady state tracking, with 0.01 dB at 1 rad/s. This makes the system comply with the steady state restriction requiring less than ± 0.1 dB steady state error, described in section 2.1. From Figure 7.17, it is also seen that the system with and without controller tends towards the same response at high frequencies. This is due to the dynamics of the electrical system dominating at high frequencies, as described in section 6.8.

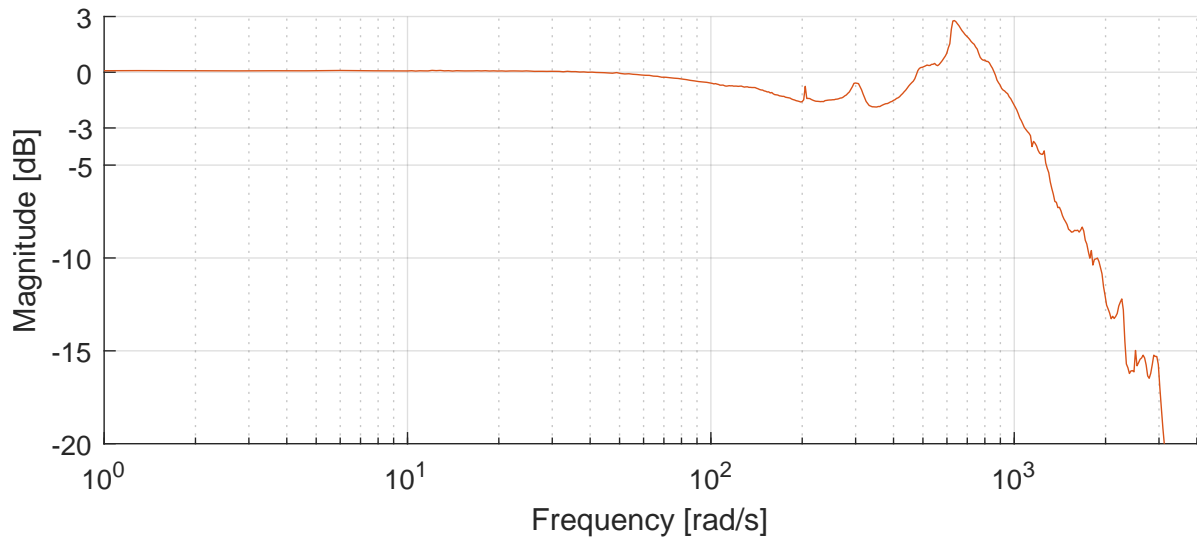


Figure 7.18. Frequency response of solenoid actuator with controller, at reduced input amplitude (100 N peak to peak)

The reason for the insignificant increase in bandwidth when implementing the controller on the solenoid actuator, is due to the slow dynamics of the electrical system at frequencies at and above the bandwidth. By reducing the amplitude of the input in the frequency response test, the electrical system gains additional voltage headroom to control the current. This is assumed equivalent to increasing the system input voltage in the frequency tests with full amplitude. Figure 7.18 shows the frequency response of the system with controller at reduced input amplitude. It can be seen that at reduced amplitudes the bandwidth of the system increases. It is therefore also assumed that by increasing the input voltage to the system, higher bandwidths are obtainable.

7.5 Subsidiary conclusion

A control algorithm consisting of four different parts is developed and partially implemented on the real time target. The fundamental structure can be seen in Figure 7.1 on page 58. The four parts of the control algorithm is a feed forward, a proportional controller, an integral controller and a Kalman filter. As described in section 7.1 a feed forward based on the non-linear model has been created. This model is suited to dynamically updating based on model parameters estimated by the Kalman filter. It is shown that the feed forward is capable of predicting the majority of the required system input. The proportional controller is based on the measured error while the integral controller reacts on the difference between the modelled and measured force, as described in section 7.2. This reduces overshoot caused by saturation in the current controller dramatically, and yields good results as shown in Figure 7.19. The controller is capable of obtaining good steady state performance, but does not increase the bandwidth of the system substantially.

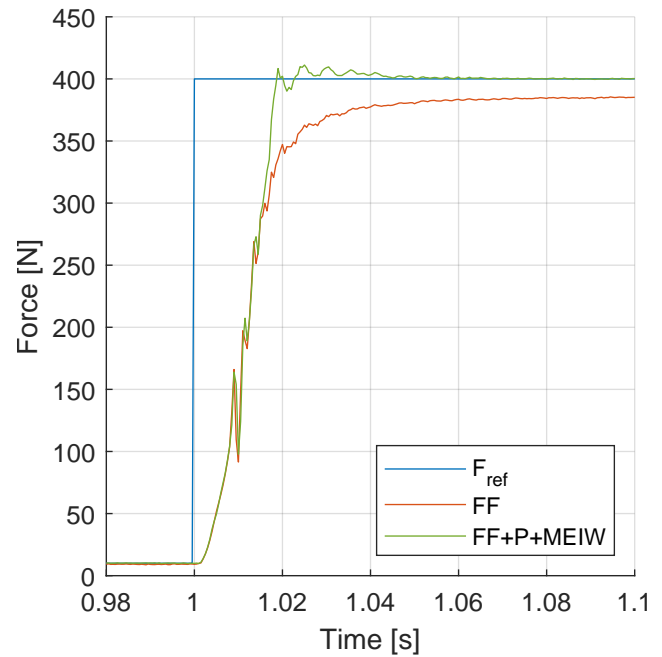


Figure 7.19. Step response of actuator system with and without controller.

A Kalman filter is proposed, designed and tested in MATLAB in order to detect zero crossings of the magnetic field within the solenoid. The Kalman filter is augmented in order to estimate changes in the air gap reluctance and the knock-down factor allowing for a dynamic update of the feed forward algorithm, and thereby reducing the impact of imperfections in the mounting of the actuator. The Kalman filter has been shown to work on actual data retrieved from tests of the actuator but for the time being it is solely implemented in MATLAB and not on the real time target. Though the results obtained from the MATLAB implementation is promising.

Conclusion 8

In this project the bandwidth of the solenoid actuator is improved from approximately 5 Hz, in the original system, to 39 Hz in the optimised design, by geometric modifications and the implementation of a closed loop control algorithm.

It is shown, through thorough magnetic FE analysis, that eddy currents are the primary contributor to the dynamics between the electrical system and the magnetic force exerted from the actuator. Based on these analyses, a slit is cut in the aluminium tubes inside the actuator, in order to limit the eddy currents, and the bandwidth is thereby increased to 24 Hz. Further refinement of the FEA model enabled the use of optimisation algorithms in order to optimise the geometry of the plunger and center piece. This optimisation algorithm finds that a series of parallel cuts in the plunger and center piece is the optimal pattern in order to minimise eddy currents. The bandwidth of the actuator is thereby increased to 38 Hz.

A non-linear solenoid actuator model is developed in order to support the developed control algorithm. The model is validated against measured data from the solenoid actuator with an average error of 3 % of the full scale force, when subjected to a random input. The model forms the basis for the control algorithm where an unconventional PI-controller is implemented together with a feed forward. The proportional controller is based on the error between reference and measured output while the integral controller is based on the error between the non-linear model and measured output, which effectively serves as anti windup. A Kalman filter, capable of estimating the present H-field in the solenoid actuator is also developed in order counteract the non-linearity around zero magnetic field. The Kalman filter is also capable of estimating some of the model parameters during operation and thereby updating the model and feed forward dynamically if the parameters changes. The Kalman filter is only designed and not implemented on the real time target, but as the primary purpose of this is to make the control algorithm robust it is not expected to improve the performance of the actuator. The implementation of the control algorithm increases the bandwidth of the optimised solenoid actuator to 39 Hz while also ensuring a steady state error below $\pm 0.1\%$. This bandwidth makes the solenoid actuator capable of exciting more than 95 % of the journal bearing designs showed in Figure 1.9 on page 6 compared to the 17 % of the original solenoid actuator.

It is found that the majority of the eddy current dynamics are suppressed by the optimised plunger design. The limiting factor for further increase of the actuator bandwidth is found to be the available controller effort in terms of supply voltage to the electrical system.

Discussion & further Work

9

The project has been limited in terms of time, therefore the project effort has been prioritised. This chapter addresses some of the possible things which should be addressed if further work is to be conducted. Here some of the assumptions, procedures and potential sources of error are discussed and evaluated.

Cuts in other parts of the actuator

In chapter 5 and chapter 6 the effects of using cuts in parts of the solenoid actuator, in order to reduce eddy currents, are investigated. In this project cuts are introduced in the plunger, center piece and aluminium tubes. It is however shown that some eddy currents are still present in the system. Figure 6.1 on page 39 shows that substantial eddy currents are present in the top and bottom caps of the solenoid actuator. It would therefore be of interest to further look into these eddy currents.

As the cross sectional area of the top and bottom cap is more than enough for the amount of flux passing through them, it is assumed that introducing cuts in these parts will not noticeably reduce the force capabilities of the actuator. Introducing cuts into these parts therefore comes without immediate disadvantages.

Voltage as input to COMSOL model

The 3D model presented in chapter 5 is capable of modelling the electrical system as well. In this project a constant current is applied to the coil. It could however be beneficial to have applied a voltage to the coil instead. By applying a voltage to the coil and inspecting the resultant force response, the slowing of the electrical system, that the cuts introduce, can be included in the assessment of the cut designs. This is however only possible in the 3D model, which is too computationally heavy to be used for optimisation. At the same time, it is assumed that the fastest overall system is the one with the fastest magnetic dynamics and thereby slowest electrical system.

Mounting the actuators at an angle

The test stand described in section 3.3 is capable of tilting the entire test stand to simulate various actuator mounting scenarios. This feature is not used in this project. Further work might therefore investigate the impact of actuator mounting angle. By angling the actuator, issues might occur due to excessive friction in the POM bushings or uneven non-working air gap length, which leads to sideways forces on the plunger.

Movement of plunger

Throughout this project the movement of the plunger is neglected. The movement of the plunger when installed in the test bench, presented in the former project (Steffensen, Sanderhoff, and Mejdahl 2021), is small, but might not be neglectable. The steady state impact of a change in the air gap length can be calculated based on Figure 1.8. The dynamic effects of plunger movement is however not investigated, and might therefore be of interest in further work.

Kalman filter implementation

In section 7.3 a Kalman filter is proposed and implemented in MATLAB. Further work on this project might therefore implement this Kalman filter on the real time target, in order to detect flux zero crossings and estimate model parameters for the feed forward live.

The system has severe problems with stability around zero force, due to the system gain changing sign. The flux zero cross detection should be able to suppress this problem. One way this zero cross detection could be used to prevent the controller from becoming unstable at negative flux, is to limit the output range of the controller whenever the flux is estimated to be negative. In this case, the controller output range should be limited to only the positive range. The flux should thereby also be kept in to the positive range, as the controller would be prohibited from driving the flux any lower when it is negative.

Improving the feed forward

Both feed forwards used in this project are based on steady state behaviour of the solenoid actuator. It would be possible to use the information contained in the model about the dynamics of the system to predict the required input to get a desired transient response. This is however not expected to increase the bandwidth of the present system as the electrical system is fully saturated during most transients.

The model based feed forward described in section 7.1, could be improved if the model, which it is based upon, featured hysteresis as well. As described in section 4.3, the model featuring the hysteresis is too computationally heavy to run in real time on the real time target. In further work it could therefore be of interest to look into this challenge. It might not be necessary to recalculate the entire hysteresis model at every time step. From Equation C.8 and C.9 on page 89 it can be seen that the calculation of the hysteresis model includes adding multiple hysteresis contributions together. It is these hysteresis contributions that takes the majority of the time to calculate. These contributions does however not change at every time step. It might therefore be possible to calculate the contributions when they first appear, and then store their values in memory. In this way, the real time target would, for every time step, only have to add the contributions stored in memory together, and occasionally calculate the new hysteresis contribution when the H-field changes in a way which creates new α or β points.

Another way to reduce the computational load on the real time target could be by pre-calculating the feed forward. Instead of only giving the real time target a reference to follow, the feed forward could also be provided. In this way, the model for the feed forward does not have to be able to execute real time. It can be calculated in advance of the experiment. The downside to pre-calculating a hysteresis based feed forward, is that the if any disturbance causes deviations from the reference, the history of the flux in the solenoid is no longer as calculated.

Non cascade control structure

The use of a Maxon ESCON module to control the current entails that the control algorithm is having a cascade control structure, where a force controller dictates the input to a current controller. Normally an assumption when designing a cascade controller is that the inner loop is significantly faster than the outer loop, but as shown in Figure 5.14 and 5.15 on page 37, this is not the case after the optimisation of the solenoid geometry. The system might therefore no longer benefit from having this cascade control structure. If a higher input voltage is desired and the ESCON module has to be replaced. The ESCON module can possibly be replaced with a simple variable voltage source, without having a significant impact on the performance of the system.

Bibliography

- COMSOL (Mar. 22, 2016). *How to Choose Between Boundary Conditions for Coil Modeling*. URL: <https://www.comsol.com/blogs/how-to-choose-between-boundary-conditions-for-coil-modeling/>.
- (2018). *AC/DC Module User’s Guide. COMSOL version 5.4*. URL: <https://doc.comsol.com/5.4/doc/com.comsol.help.acdc/ACDCModuleUsersGuide.pdf>.
- (2019). *User’s Guide. COMSOL version 5.5*. URL: https://doc.comsol.com/5.5/doc/com.comsol.help.comsol/comsol_api_mesh.40.19.html.
- DS/EN60404-4 (n.d.). “Magnetiske materialer Del 4: Metoder til måling af jævnstrømsegenskaber for jern og stål”. In: *Dansk Standard* ().
- Grewal, Mohinder S. and Angus P. Andrews (2001). *Kalman Filtering: Theory and Practice Using MATLAB*. Wiley-Interscience. ISBN: 0-471-26638-8.
- Isermann, Rolf (2006). *Fault-Diagnosis Systems. An Introduction from Fault Detection to Fault Tolerance*.
- MATLAB (2022a). *Surrogate Optimization Algorithm*. URL: <https://www.mathworks.com/help/gads/surrogate-optimization-algorithm.html>.
- (2022b). *What Is Surrogate Optimization?* URL: <https://www.mathworks.com/help/gads/what-is-surrogate-optimization.html>.
- NDT Supply.com (2002). *Conductivity and Resistivity Values for Aluminum Alloys*. URL: https://content.ndtsupply.com/media/Conductivity_Al%5C%20Reference%5C%20Chart.pdf.
- Per Johansen (Sept. 1, 2020). *Adaptive Ultrasound Reflectometry Techniques for Smart Tribology Systems*. URL: <https://vbn.aau.dk/en/projects/adaptive-ultrasound-reflectometry-techniques-for-smart-tribology--2> (visited on 11/05/2022).
- Pruksanubal, P, A Binner, and K. H Gonschorek (Feb. 2006). “Determination of Distribution Functions and Parameters for the Preisach Hysteresis Model”. In: *17th International Zurich Symposium on Electromagnetic Compatibility*.
- Ramirez-Laboreo, Edgar, Maurice Roes, and Carlos Sagues (2019). “Hybrid Dynamical Model for Reluctance Actuators Including Saturation, Hysteresis and Eddy Currents”. In: *IEEE/ASME Transactions on Mechatronics*.
- Steffensen, Daniel Woldbye, Frederik Sanderhoff, and Jens Erik Damgaard Mejdahl (2021). *Test Setup with Radial Load Control for Journal Bearings*. Aalborg Universitet.

Part I
Appendix

Structural analysis of test stand



A.1 Aim

The rigidity of an actuator test stand is of high importance if the steady state and dynamic results of the actuator behavior are to be reliable. Especially the distance between each mounting point during load is of interest, since the length of the air gap within the actuator has influence on both steady state and dynamic results.

A.2 Simulation

The simulation used to evaluate the base plate is a static linear analysis assuming small deformations and linear material behavior. The software used for the simulation is SOLIDWORKS 2021.

A.2.1 Geometry

The test stand is made of two triangular end plates with a thickness of 15 mm and three pillars with a length of 315 mm and a diameter of 20 mm. The pillars are used to keep a fixed distance between the end plates. The top end plate has a threaded M12 hole in the center in order to mount a threaded rod with a mounting bracket and allow for vertical adjustment of the actuator. The bottom end plate has two threaded M8 holes that allow for bolting a mounting bracket on this part, as shown in Figure A.1.

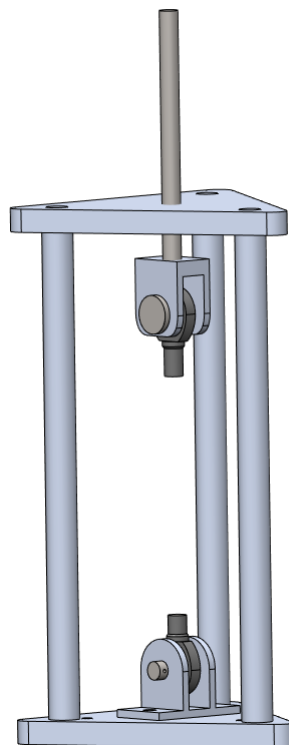


Figure A.1. The test stand with end plates, pillars and the actuator mounts.

A.2.2 Material

The majority of the test stand is made from aluminium, where the threaded rod and pins are made from steel. The material properties used for the simulation are stated in Table A.1

Material	Poisson's ratio	Elastic modulus [GPa]	Yield strength [MPa]
Aluminium	0.33	69.0	27.6
Steel	0.28	210	235

Table A.1. Material properties used in analysis.

A.2.3 Boundary conditions

During tests the test stand is going to be placed on a table and thereby friction is the only force holding it in place. In order to simplify the model a small circle in the middle of the bottom end plate is fixed instead of modelling the friction between table and test stand as shown in Figure A.2. The fixed boundary condition implies that the nodes on the chosen surface cannot translate in any direction, meaning the chosen surface is infinitely stiff. By only applying this boundary condition to a small area the added stiffness is small compared to the stiffness of the end plate.

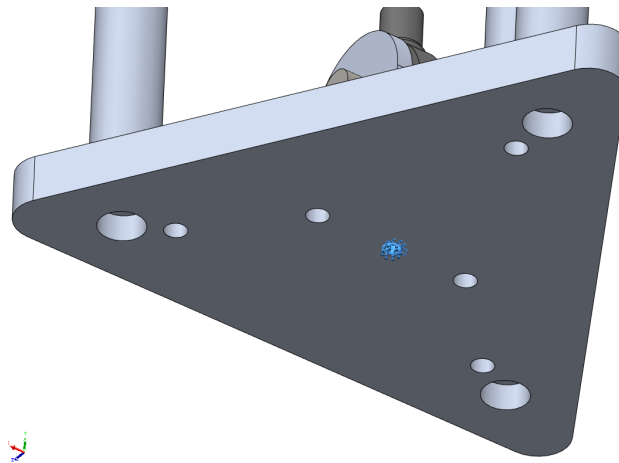


Figure A.2. The fixture is applied to the area marked in blue.

The interaction between the different components are defined as "bonded", meaning that the nodes are merged as if it was the same part.

The forces applied to the test stand from the actuator is applied to the rod ends as shown in Figure A.3. A force of 650 N is applied to both rod ends in a direction such that they pull towards each other.

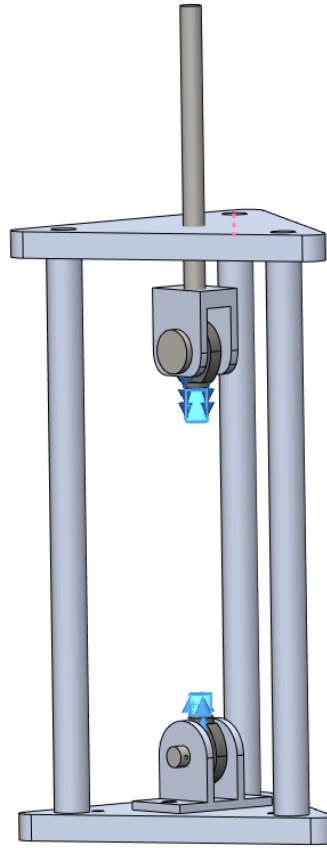


Figure A.3. The forces are applied to the rod ends.

A.2.4 Mesh

The test stand is meshed with parabolic tetrahedral solid elements with a global size of 2.5 mm after a mesh convergence analysis is performed as described in section A.3.

A.3 Results

The vertical displacement of the two horizontal rod end faces are measured as shown in Figure A.4. The result of the mesh convergence can be seen in Table A.2

Mesh size [mm]	Displacement [mm]	Deviation	# nodes	Solution time [mm:ss]
10	-0.0292	-	27171	00:05
5	-0.0295	1.0%	96643	00:15
2.5	-0.0297	0,7%	557766	01:09

Table A.2. Results from analysis.

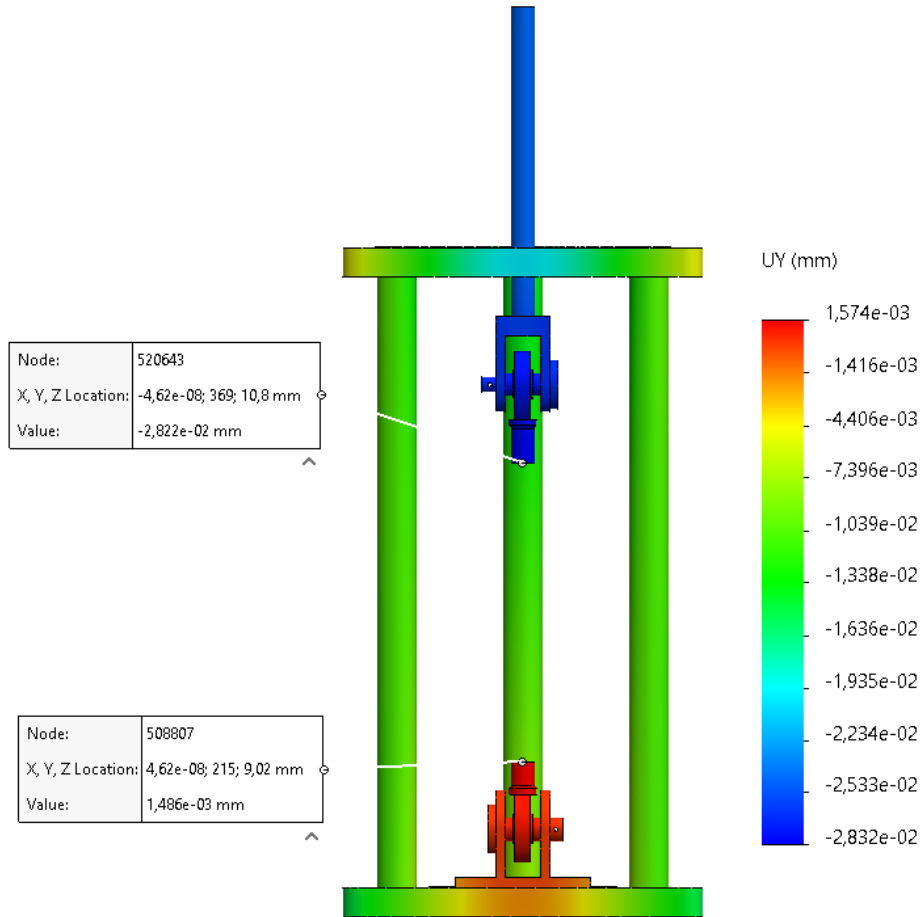


Figure A.4. The displacements of the two horizontal rod end faces.

Table A.2 shows that, the displacement on the test stand reaches approximately 0.03 mm when subjected to a force of 650 N. Compared to the air gap within the actuator this is:

$$change = \frac{0.0297 \text{ mm}}{2 \text{ mm}} \approx 1.5 \% \quad (\text{A.1})$$

According to Figure 1.8, there is a force sensitivity of 370 N mm^{-1} , when the air gap length is 2 mm and the current is 5 A. Thereby the change in force due to the displacement of the actuator test stand becomes:

$$\Delta F = 370 \text{ N mm}^{-1} \cdot 0.0297 \text{ mm} \approx 11 \text{ N} \quad (\text{A.2})$$

A.4 Discussion

The boundary condition, where all nodes within the small circle are fixed, adds an artificial stiffness to the bottom end plate. However as mentioned subsection A.2.3, the area is assessed to be sufficiently small such that the added stiffness is insignificant compared to the inherent stiffness of the end plate itself.

A.5 Subsidiary conclusion

Based on the FEM analysis, it is found that the actuator test stand has a displacement of 0.0297 mm when exposed to an actuator force of 650 N. This displacement will result in a 1.5 % change in the actuator air gap, and thereby result in an 11 N increase which is deemed to be sufficiently small.

Magnetic material properties of S235 B

B.1 Aim

The following experiment is made to identify the magnetic material properties of the structural steel, S235, used to manufacture the solenoid actuators. The majority of the experiment is based on DS/EN60404-4 (n.d.).

B.2 Theory

DS/EN60404-4 (ibid.) method "a" uses a closed steel ring where an excitation coil and a sense coil is wound around the ring. The flux linkage between the two coils is defined by the material parameters, and can be determined if the current input of the excitation coil and voltage output of the sense coil is known. According to DS/EN60404-4 (ibid.) the relationship between inner and outer diameter must be $D \leq 1.1d$, where D is the outer diameter and d is the inner diameter. In that case the magnetic path length, l , can be calculated as:

$$l = \pi \frac{D + d}{2} \quad (\text{B.1})$$

Thereby the magnetic field strength, H-field, can be calculated as:

$$H = \frac{N_1 i}{l} \quad (\text{B.2})$$

Where H is the magnetic field strength, N_1 is the number of turns of the excitation coil and i is the current in the excitation coil.

The voltage signal in the sense coil is defined by Faraday's law of induction:

$$v_2 = N_2 \frac{d\Phi}{dt} \quad (\text{B.3})$$

Where v_2 is the voltage over the sense coil, N_2 is the number of turns of the sense coil and Φ is the total flux in the ring specimen. The flux can also be expressed as:

$$\Phi = \int B \, dA \quad (\text{B.4})$$

Where A is the cross-sectional area of the specimen, and B is the magnetic flux density in the specimen. For a uniform distributed B-field it can be approximated as:

$$\Phi = BA \quad (\text{B.5})$$

Thereby the flux density, B-field, can be expressed as:

$$v_2 = N_2 A \frac{dB}{dt} \quad (\text{B.6})$$

$$\int v_2 dt = N_2 A \int \frac{dB}{dt} dt \quad (\text{B.7})$$

$$\int v_2 dt = N_2 AB \quad (\text{B.8})$$

$$B = \frac{\int v_2 dt}{N_2 A} \quad (\text{B.9})$$

The H-field and B-field can thereby be determined based on Equation B.2 and B.9, respectively.

B.3 Experimental setup

The test specimen is manufactured in accordance with DS/EN60404-4 (n.d.) with an inner diameter of 100 mm, an outer diameter of 110 mm and a height of 20 mm. All corners are rounded with a fillet of radius 2 mm, whereafter the specimen is covered in a layer of electrically isolating tape as shown in Figure B.1. A sense coil with a wire diameter of 0.5 mm is wound with 534 turns as shown in Figure B.2. Hereafter the excitation coil with a wire diameter of 0.9 mm is wound over it with 613 windings as shown in Figure B.3.



Figure B.1. The test specimen **Figure B.2.** The test specimen with **Figure B.3.** The complete test specimen covered in a layer of electrically isolating tape.

In order to deliver a specific current of up to 8 A in the excitation coil and measure the resulting voltage over the sense coil, the following equipment is used:

- c-Rio with NI-9263 module - supplying an analog output used to control the amplifier
- Amcron DC300A series II - amplifies the signal from the c-Rio and works as current source
- 4.7 Ω load resistor - increases overall system resistance in order to better control the current
- Tektronix DPO 2014B - oscilloscope used to record voltage and current data
- Fluke multimeter and thermocouple - measuring the temperature of the test specimen

The test setup and wiring diagram can be seen in Figure B.4 and B.5.

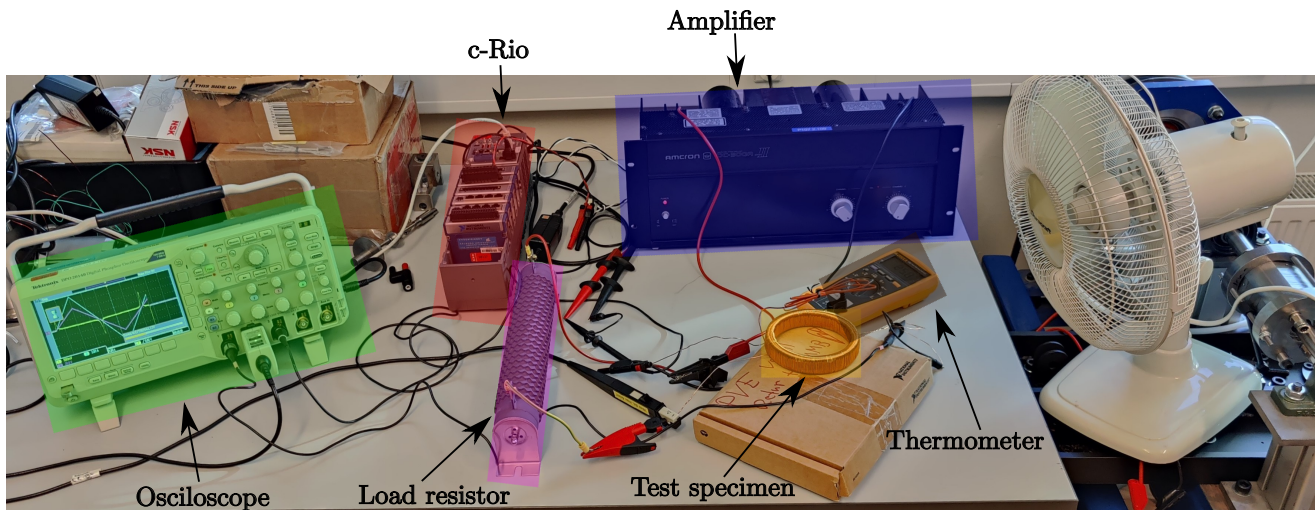


Figure B.4. The test setup during a test.

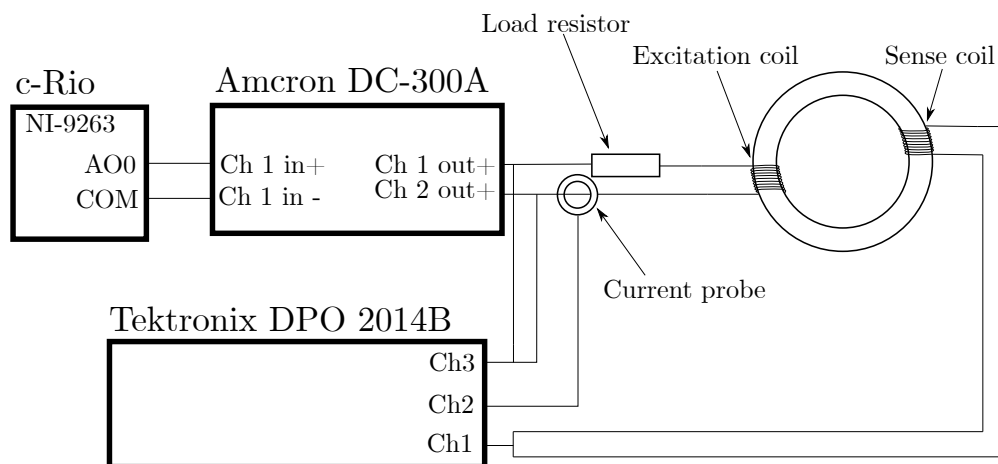


Figure B.5. Wiring diagram of the test setup.

B.4 Procedure

Before all tests a demagnetization current is applied to the test specimen. The demagnetization current consists of a sinusoidal current starting with a peak-peak amplitude of 16 A whereafter the amplitude is linearly reduced to 0 A over the course of 30 s. The temperature of the test specimen is measured during all tests and measures are taken in order to ensure that the test specimen does not reach a temperature higher than 35 °C. Both the normal magnetization curve and the complete hysteresis loop is of interest and therefore different tests are conducted in order to find these.

B.4.1 Normal magnetization curve

The equations shown above does not take eddy currents into account, and it is therefore desirable to minimise these during the test. The eddy currents are best minimised by reducing the rate of change of current and thereby the rate of change in the magnetic field. The test specimen is subject to steady current ramps from 0 A to 8 A with a test duration varying from 0.5 s to 10 s. It is subsequently estimated which tests are influenced by eddy currents.

B.4.2 Hysteresis loop

In order to determine the complete hysteresis loop, a series of low frequency saw tooth current signals are applied with peak-peak amplitudes ranging between 16 A and 0.25 A. The applied frequency is 0.25 Hz and ensures that the hysteresis is minimally affected by eddy currents.

B.5 Results

B.5.1 Normal magnetization curve

The test specimen is subjected to the current reference shown in Figure B.6 and the resulting voltage is measured over the sense coil. The resulting sense coil voltage can be seen in Figure B.7 for all the tests, where any bias is removed. The ramp duration for each test shown in Figure B.7 is shown in Table B.1.

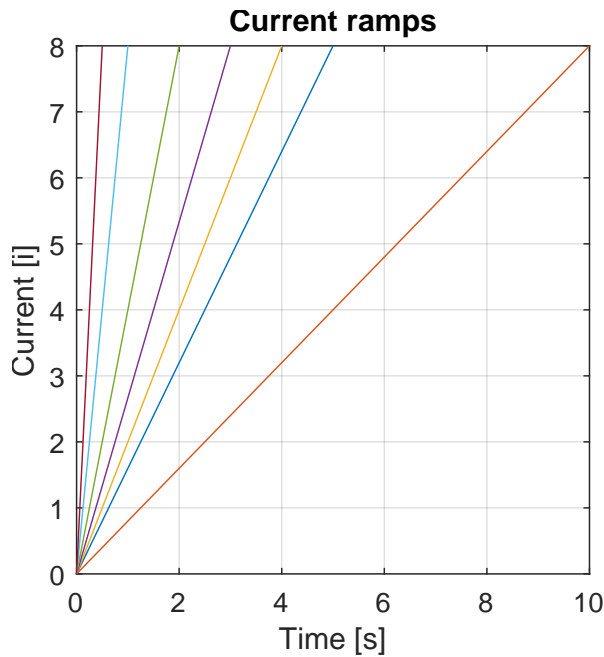


Figure B.6. The applied current on the excitation coil.

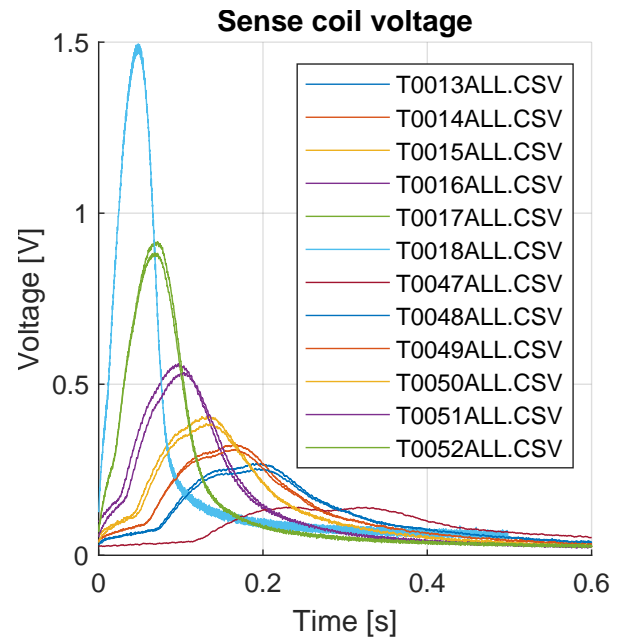


Figure B.7. The measured voltage on the sense coil during tests with ramp current.

Test name	Duration
T0013ALL	5 s
T0014ALL	4 s
T0015ALL	3 s
T0016ALL	2 s
T0017ALL	1 s
T0018ALL	0.5 s
T0047ALL	10 s
T0048ALL	5 s
T0049ALL	4 s
T0050ALL	3 s
T0051ALL	2 s
T0052ALL	1 s

Table B.1. Tests and the input current ramp duration.

The H-field at a given time is calculated with Equation B.2 and the resulting B-field is calculated with Equation B.9. Using these equations the resulting BH-curve for each test can be found.

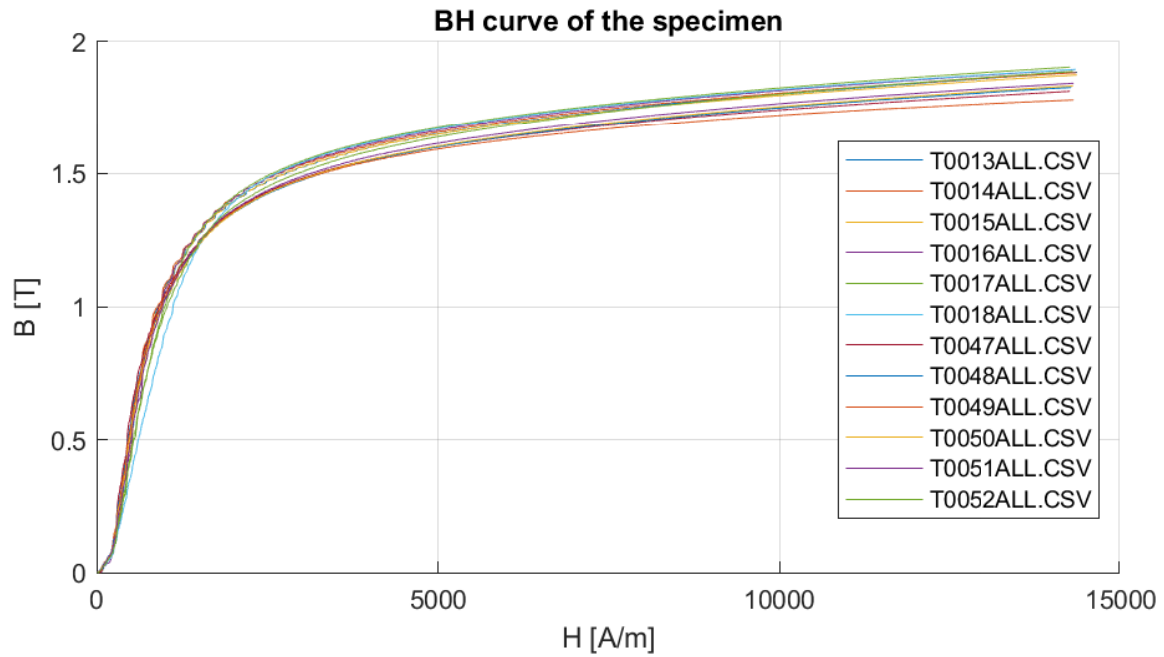


Figure B.8. The measured BH-curve.

Figure B.8 shows that for ramps with a duration of 0.5 s or more the eddy currents do not have a significant influence on the normal magnetization curve

B.5.2 Hysteresis loop

In order to find the hysteresis loop, a saw tooth shaped input current is supplied to the excitation coil on the test specimen. Based on the findings in subsection B.5.1 it is assessed that a signal frequency of 0.25 Hz is sufficiently low to avoid a significant effect from eddy currents. Several tests are conducted with peak-peak amplitudes ranging between 0.5 A and 16 A as shown in Figure B.9.

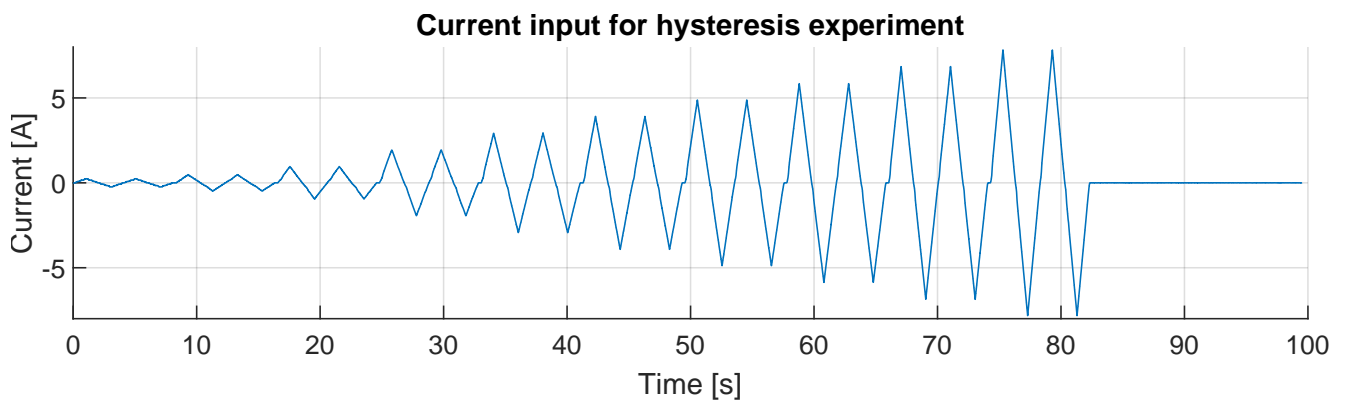


Figure B.9. The applied current on the excitation coil.

The sense coil voltage corresponding to the applied current is shown in Figure B.10 after any bias is been removed.

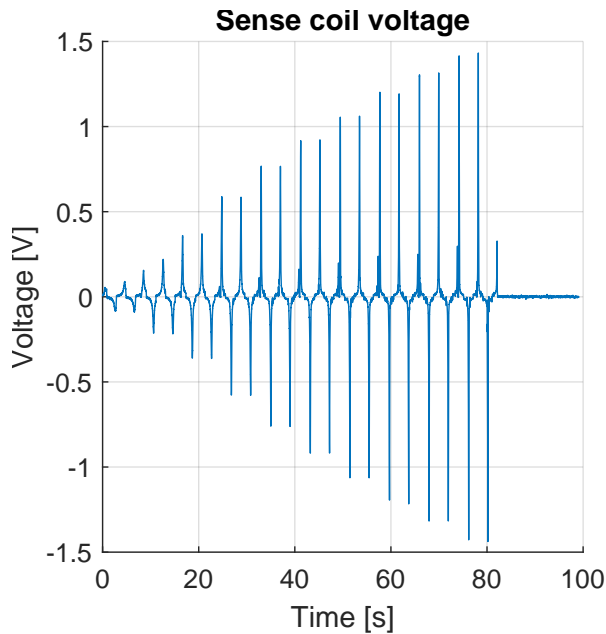


Figure B.10. The measured voltage on the sense coil during tests with saw tooth current.

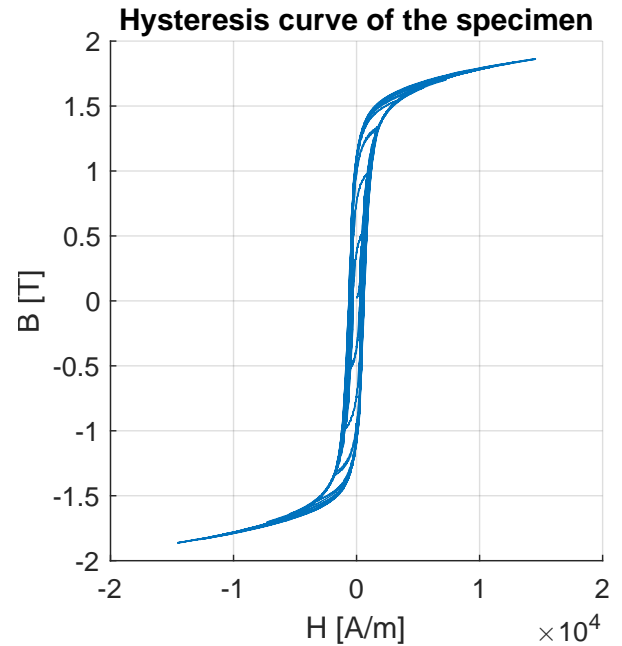


Figure B.11. The calculated hysteresis loop based on measured voltage and applied current.

The H-field can be calculated by Equation B.2 and the data shown in Figure B.9, while numerical integration of the voltage shown in Figure B.10, as described in Equation B.9, yields the corresponding B-field. When the calculated B-field is plotted as a function of the calculated H-field, the hysteresis loop is found as shown in Figure B.11.

B.6 Discussion

Some deviations have been made from the standard, (DS/EN60404-4 n.d.), for practical reasons.

The cross sectional area of the test specimen might have an uncertainty of more than the specified 0.5% since all sharp edges is rounded. The rounding radius is approximately 2 mm. Due to manufacturing time and thereby also price considerations it is assessed that a potential deviation of the area is so small that the accuracy of the results are still within the useful limits of this project.

The standard also dictates that an analog integrator is used to integrate the voltage signal from the sense coil. It is decided to utilise a numerical integrator, since it reduces the number of instruments that is needed for the tests.

B.7 Conclusion

The magnetic material properties found in the tests described above are consistent with the expected findings. Both the normal magnetisation curve, Figure B.8, and the hysteresis curve, Figure B.11, are consistent with the general shape expected from ferromagnetic materials. The results are therefore considered acceptable.

Mathematical basis of Preisach model



Using the distribution functions, two new variables are to be defined as $h_c = \frac{\alpha - \beta}{2}$ and $h_m = \frac{\alpha + \beta}{2}$, due to a transformation of coordinates, (Ramirez-Laboreo, Roes, and Sagues 2019). With the transformation of coordinates and the distribution functions, the Preisach function is transformed to:

$$P(\alpha, \beta) = f_1(h_c)f_2(h_m) \quad (C.1)$$

Where f_1 and f_2 are the distribution functions.

$$f_{Cauchy}(x|m_x, s_x) = \frac{1}{\pi s_x \left(1 + \left(\frac{x - m_x}{s_x}\right)^2\right)} \quad (C.2)$$

$$F_{Cauchy}(x|m_x, s_x) = \frac{1}{2} + \frac{1}{\pi} \arctan\left(\frac{x - m_x}{s_x}\right) \quad (C.3)$$

Here f denotes the distribution function and the belonging cumulative distribution function will be denoted by capital F . Thereby:

$$f_1(h_c) = f_{Cauchy}(h_c|m_{h_c}, s_{h_c}) \quad (C.4)$$

$$f_2(h_m) = f_{Cauchy}(h_m|m_{h_m}, s_{h_m}) \quad (C.5)$$

As described in Ramirez-Laboreo, Roes, and Sagues (ibid.), the CPM output can be calculated by integrating the areas in Figure 4.8 and the calculating the sum of these areas. For the given Preisach function, $P(\alpha, \beta)$, the integral over a triangle, T , in the Preisach plane can be defined as:

$$T(\alpha_i, \beta_j) = \int_{\beta_j}^{\alpha_i} \int_{\beta}^{\alpha_i} P(\alpha, \beta) d\alpha d\beta \quad (C.6)$$

$$T(\alpha_i, \beta_j) = 2 \int_0^{h_c} f_1(h_c) \left[F_2(h_m) \right]_{\beta_j + h_c}^{\alpha_i - h_c} dh_c \quad (C.7)$$

By adding and subtracting the weighted area of different triangles, defined by Equation C.6, the CPM output (B-field) can be obtained. It is necessary to calculate the CPM output in two different ways depending on whether the input is increasing or decreasing:

$$f_{CPM, increasing} = -T(\alpha_0, \beta_0) + 2 \sum_{k=1}^n T(\alpha_k, \beta_{k-1}) - 2 \sum_{k=1}^n T(\alpha_k, \beta_k) + 2T(H, \beta_n) \quad (C.8)$$

$$f_{CPM, decreasing} = -T(\alpha_0, \beta_0) + 2 \sum_{k=1}^n T(\alpha_k, \beta_{k-1}) - 2 \sum_{k=1}^{n-1} T(\alpha_k, \beta_k) - 2T(\alpha_n, H) \quad (C.9)$$

Here n denotes the total number of α levels (local maximums in the past) in Figure 4.8 and H denotes the present input. From Equation C.8 and C.9 it is seen, that an increasing number of α levels, n , increases the number of calculations necessary to compute the CPM output.

The CPM has a drawback, which is, that the magnetic incremental permeability, μ' , is zero in the reversal points, which is when \dot{H} changes sign. This means that whenever the H-field changes direction, the model presented in Equation 4.18 is undefined, as $\mu'(H_{steel})$ will be zero. Therefore the GPM is presented, since this has a non-zero magnetic permeability in the reversal point (Ramirez-Laboreo, Roes, and Sagues 2019).

The output of the GPM, f_{GPM} , consists of two parts, a reversible and an irreversible part:

$$f_{GPM} = B_{rev} + B_{irr} \quad (C.10)$$

Here B_{rev} is already defined as the BH-curve in Equation 4.23, and according to Ramirez-Laboreo, Roes, and Sagues (ibid.), the irreversible part can be defined as:

$$B_{irr} = \hat{B}_{irr} \frac{f_{CPM}}{T(\alpha_0, \beta_0)} \quad (C.11)$$

Where \hat{B}_{irr} is the saturation level of the irreversible part and $T(\alpha_0, \beta_0)$ is a normalisation term.

The magnetic incremental permeability is calculated as:

$$\mu'_{GPM} = \frac{\delta f_{GPM}}{\delta H} = \frac{\delta B_{rev}}{\delta H} + \frac{\delta B_{irr}}{\delta H} \quad (C.12)$$

Since $\frac{dB_{rev}}{dH}$ is defined in Equation 4.24, only the irreversible permeability, $\frac{dB_{irr}}{dH}$, needs to be derived. According to Ramirez-Laboreo, Roes, and Sagues (ibid.), the irreversible permeability can be found as follows:

$$\mu_{irr,increasing} = \frac{\delta B_{irr}}{\delta H} = \frac{\hat{B}_{irr}}{T(\alpha_0, \beta_0)} \frac{\delta f_{CPM,increasing}}{\delta H} = \frac{\hat{B}_{irr}}{T(\alpha_0, \beta_0)} 2 \int_{\beta_n}^H P(H, \beta) d\beta \quad (C.13)$$

$$\mu_{irr,decreasing} = \frac{\delta B_{irr}}{\delta H} = \frac{\hat{B}_{irr}}{T(\alpha_0, \beta_0)} \frac{\delta f_{CPM,decreasing}}{\delta H} = \frac{\hat{B}_{irr}}{T(\alpha_0, \beta_0)} 2 \int_H^{\alpha_n} P(\alpha, H) d\alpha \quad (C.14)$$

Electrical conductivity of S235

D

D.1 Aim

The following experiment is made to identify the electrical conductivity of the structural steel, S235, used to manufacture the solenoid actuators.

D.2 Theory

The electrical conductivity is the reciprocal of the electrical resistivity.

The resistivity of a given material in a test specimen can be calculated by:

$$\rho = R \frac{A}{l} \quad (\text{D.1})$$

Where ρ is the electrical resistivity, R is the resistance, A is the cross sectional area and l is the length of the test specimen.

The resistance of the test specimen can be calculated from Ohm's law:

$$R = \frac{V}{I} \quad (\text{D.2})$$

Where V is the voltage and I is the current.

The electrical conductivity can then be calculated by:

$$\sigma = \frac{1}{\rho} \quad (\text{D.3})$$

Where σ is the electrical conductivity.

D.3 Experimental setup & procedure

A sketch of the experimental setup can be seen on Figure D.1. The test specimen is placed on isolating rubber supports, to prevent alternative current paths. The resistivity tests are conducted using a four wire method to increase accuracy. A pair of current delivering alligator clips, connected to the current source, are clipped on both ends of the test specimen. Before mounting, all contact points on the test specimens are brushed with a wire brush to ensure good contact between the specimen and the alligator clips.

Approximately 10 cm from the current carrying alligator clips towards the center of the test specimen, another pair of alligator clips are placed. These are connected to a volt meter which measures the voltage drop across the test specimen. All test are conducted at 6 A current, as this is the max current for the power supply.

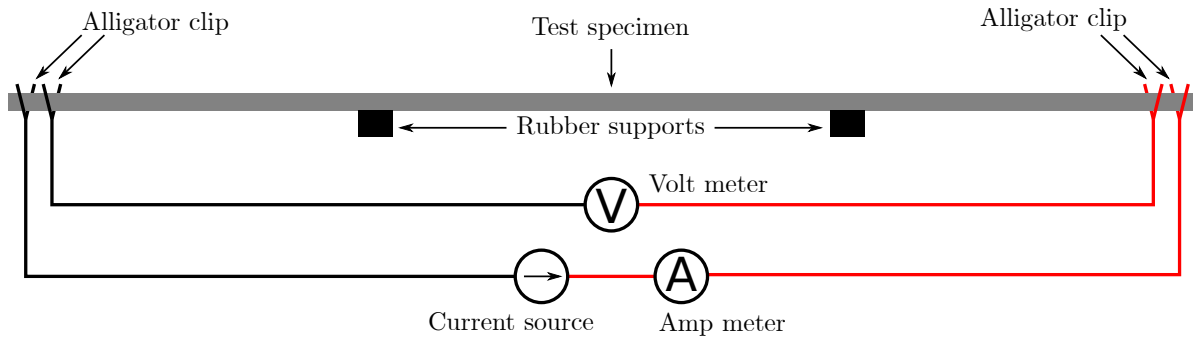


Figure D.1. Experimental setup for electrical conductivity test.

the following equipment is used:

- GW instek GPD-3303S - DC power supply. 6 A max current.
- Fluke 45 - Multimeter used for voltage measurements.
- Fluke 8845A - Multimeter used for current measurements.

The test specimens are selected stock from the steel depot at AAU.

The following specimens have been tested:

Specimen number	Cross sectional area [mm ²]	Length [mm]	Profile
1	64	2831	Square
2	36	2672	Square
3	25	2815	Square
4	80	2674	Square
5	126	2682	Square
6	60	2811	Strip
7	201	2043	Round
8	201	1853	Round
9	283	2827	Round

Table D.1. Specimens for electrical conductivity test.

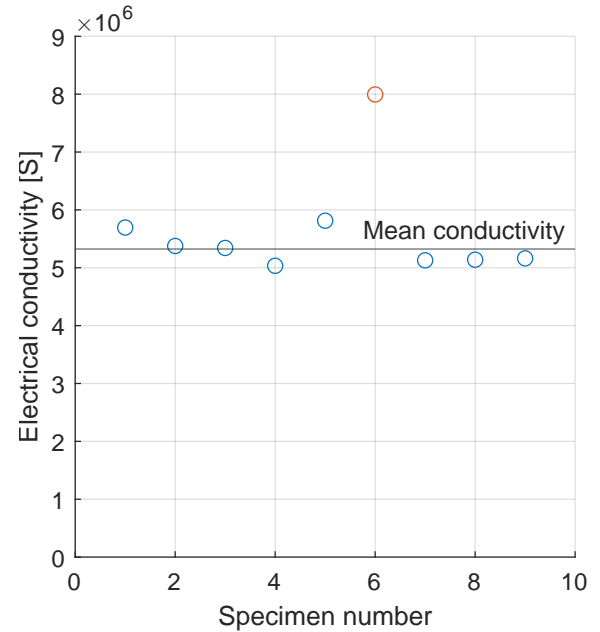


Figure D.2. Results of the conductivity test.

The specimen length is determined as the distance between the two voltage probing alligator clips.

D.4 Results

Figure D.2 shows the results of the test. Test six is excluded as it is deemed an outlier. It is the only specimen which is a piece of strip steel, which means that the resistance is highly dependent on the thickness. The test result is based on an average of the remaining specimens. The electrical conductivity is therefore determined to be 5.32 MS.

D.5 Discussion

The tests are conducted on stock from the steel depot at AAU. There is therefore no guarantee that the steel tested in these tests are the same or equivalent to the S235 used for the actuators. It is however assumed that the stock from the steel depot is representable for the steel used in the actuators.

D.6 Conclusion

The electrical conductivity of 5.32 MS, found in the tests described above lies within the expected range. The results are therefore considered acceptable.

Previous report by the same authors



The project is a continuation of the work done in a previous project by the same authors (Steffensen, Sanderhoff, and Mejdahl 2021). As the report might not be easily accessible to persons outside of Aalborg University, it is included as external appendix.

The report can be found at the following path in the external appendix:

External appendix\Appendix E\Previous report

Technical drawings of test stand



The technical drawings created for the actuator test stand can be found at the following path in the external appendix:

External appendix\Appendix F\Technical drawings